INL/EXT-12-26425

Zone Freezing Study for Pyrochemical Process Waste Minimization

Ammon Ned Williams

May 2012

The INL is a U.S. Department of Energy National Laboratory
operated by Battelle Energy Alliance

INL/EXT-12-26425

Zone Freezing Study for Pyrochemical Process Waste Minimization

Ammon Ned Williams

May 2012

Idaho National Laboratory
Idaho Falls, Idaho 83415

http://www.inl.gov

Prepared for the
U.S. Department of Energy
Through the INL LDRD Program
Under DOE Idaho Operations Office
Contract DE-AC07-05ID14517

ZONE FREEZING STUDY FOR PYROCHEMICAL PROCESS WASTE MINIMIZATION

A Thesis

Presented in Partial Fulfillment of the Requirements for the

Degree of Master of Science

with a

Major in Chemical Engineering

in the

College of Graduate Studies

University of Idaho

by

Ammon Ned Williams

May 2012

Major Professor: Supathorn Phongikaroon, Ph.D.

Authorization to Submit Thesis

This thesis of Ammon N. Williams, submitted for the degree of Master of Science with a major in Chemical Engineering and titled "Zone Freezing Study for Pyrochemical Process Waste Minimization," has been reviewed in final form. Permission, as indicated by the signatures and dates given below, is now granted to submit final copies to the College of Graduate Studies for approval.

Major Professor _____Date_____
Supathorn Phongikaroon

Committee Members _____Date_____
Vivek Utgikar

_____Date_____
Akira Tokuhiro

Department Administrator _____Date_____
Wudneh Admassu

Discipline's College Dean _____Date_____
Larry Stauffer

Final Approval and Acceptance by the College of Graduate Studies

_____Date_____
Jie Chen

Abstract

Pyroprocessing technology is a non-aqueous separation process for treatment of used nuclear fuel. At the heart of pyroprocessing lies the electrorefiner, which electrochemically dissolves uranium from the used fuel at the anode and deposits it onto a cathode. During this operation, sodium, transuranics, and fission product chlorides accumulate in the electrolyte salt (LiCl-KCl). These contaminates change the characteristics of the salt overtime and as a result, large volumes of contaminated salt are being removed, reprocessed and stored as radioactive waste. To reduce the storage volumes and improve recycling process for cost minimization, a salt purification method called zone freezing has been proposed at Korea Atomic Energy Research Institute (KAERI).

Zone freezing is melt crystallization process similar to the vertical Bridgeman method. In this process, the eutectic salt is slowly cooled axially from top to bottom. As solidification occurs, the fission products are rejected from the solid interface and forced into the liquid phase. The resulting product is a grown crystal with the bulk of the fission products near the bottom of the salt ingot, where they can be easily be sectioned and removed. Despite successful feasibility report from KAERI on this process, there were many unexplored parameters to help understanding and improving its operational routines. Thus, this becomes the main motivation of this proposed study. The majority of this work has been focused on the CsCl-LiCl-KCl ternary salt. $CeCl_3$-LiCl-KCl was also investigated to check whether or not this process is feasible for the trivalent species—surrogate for rare-earths and transuranics. For the main part of the work, several parameters were varied, they are: (1) the retort advancement rate—1.8, 3.2, and 5.0 mm/hr, (2) the crucible lid configurations—lid versus no-lid, (3) the amount or size of mixture—50 and 400 g, (4) the composition of CsCl in the salt—1, 3, and 5 wt%, and (5) the temperature differences between the high and low furnace zones—200 and 300 °C. During each experiment, the temperatures at selected locations around the crucible were measured and recorded to provide temperature profiles. Following each experiment, samples were collected and elemental analysis was done to determine the composition of

the salt. Several models—non-mixed, well-mixed, Favier, and hybrid—were explored to describe the zone freezing process.

For CsCl-LiCl-KCl system, experimental results indicate that through this process up to 90% of the used salt can be recycled, effectively reducing waste volume by a factor of ten. The optimal configuration was found to be a 5.0 mm/hr rate with a lid configuration and a ΔT of 200°C. The larger 400 g mixtures had recycle percentages similar to the 50 g mixtures; however, the throughput per time was greater for the 400 g case. As a result, the 400 g case is recommended. For the $CeCl_3$-LiCl-KCl system, the result implies that it is possible to use this process to separate the rare-earth and transuranics chlorides. Different models were applied to only CsCl ternary system. The best fit model was the hybrid model as a result of a solute transport transition from non-mixed to well-mixed throughout the growing process.

Acknowledgment

I am sincerely grateful to my advisor and friend, Dr. Supathorn Phongikaroon, for his endless time and effort mentoring and guiding me to become a great engineer. He provided many opportunities for me to make the research my own and to present it in various conferences and forums, and I really appreciated that. I would like to thank Dr. Michael Simpson for his technical expertise. Thank you, Joanna Taylor and Michael Shaltry, for all of your help in navigating the laboratory side of research. They helped the work move forward. Thank you to the other members of my research group: Rob Hoover, Ryan Bezzant, Josh Versey, Elizabeth Sooby, and Michael Pack for informative conversations and fun times. I owe a gigantic thanks to my committee members, Drs. Akira Tokuhiro and Vivek Utgikar, for their invaluable input. I am so glad that I have had the opportunity to rub shoulders with such great people. Thank you to everyone that has helped me along the way.

This work was supported by the Laboratory Directed Research and Development (LDRD) Program of Idaho National Laboratory, administered by the Center for Advanced Energy Studies, under the Department of Energy Idaho Operations Office Contract DE-AC07-05ID14517.

Table of Contents

List of Figures

List of Tables

List of Symbols

Symbol	Description	Unit
C	Concentration	
C_a	C_L-C_0	
C_B	Bulk Fluid Concentration	
C_L	Liquid Concentration	
C_S	Solid Concentration	
C_0	Initial Concentration	
D	Diffusion Coefficient	m^2/s
f_S or h/h_0	Fraction Solidified	
g	Gravitational Constant	m/s^2
Gr	Grashof Number	
h	Distance Solidified from the Top Surface	m
h_0	Overall Crystal Height	m
i, j	Indexing Variables	
k	Segregation Coefficient (C_S/C_L)	
k_0	Equilibrium Segregation Coefficient (C_S/C_B @ equilibrium)	
k_{eff}	Effective Segregation Coefficient (C_S/C_B)	
L	Characteristic Length (height of liquid)	m
L_{Liq}	Height of the Bulk Liquid Phase	m
m	Mass	g
P	Numerical Time Iteration	
Pe	Peclet Number	
Pr	Prandtl Number	
R	Growth Rate	m/s
r	Characteristic Length (radius of crucible)	m
R^2	Coefficient of Determination	
R_g	Universal Gas Constant	J/mol K
RMSD	Root Mean Squared Deviation	%
Sc	Schmidt Number	

t	Time	s
T1, T2, T3, T4	Temperatures around the Crucible	°C
T_{melt}	Melting Temperature of the Mixture	°C
wt%	Weight Percent	%
x	Position from the Solid-Liquid Interface	m
ΔH_{fusion}	Heat of Fusion	J/kg
Δt	Numerical Time Step	s
Δx	Numerical Mesh Size	m

Chemical Symbols

Ag+	Silver Ion
Au+	Gold Ion
CCS1	Mixture of Rare Earth Elements
CCS4	Mixture of Major-Earth Elements
Ce	Cerium
$CeCl_3$	Cerium Chloride
Cs	Cesium
CsCl	Cesium Chloride
Cu+	Copper Ion
K	Potassium
KCl	Potassium Chloride
Li	Lithium
LiCl	Lithium Chloride
Na	Sodium
NaCl	Sodium Chloride
Rb+	Rubidium Ion
Sr	Strontium
$SrCl_2$	Strontium Chloride
Tl+	Thallium Ion

Greek Symbols

α	Proportionality Constant	
α_i and β_i	Roots of Eqn. 2.23	
β	Expansion Coefficient	
δ	Diffusion Boundary Layer Thickness	m
Δ	Transport Parameter ($R\delta/D$)	
μ	Dynamic Viscosity	$N{\cdot}s/m^2$
ν	Kinematic Viscosity	m^2/s
ξ	Dimensionless Position	
ρ	Density	kg/m^3
τ	Dimensionless Time	
τ^*	Dimensionless Time at Steady State	
χ	Mole Fraction	
ω	Mass Fraction	

Chapter 1 Introduction

1.1 Purpose

The purpose of this thesis is to conduct a parametric study on the effect of key zone freezing parameters on the separation of cesium chloride (CsCl) from a lithium chloride-potassium chloride (LiCl-KCl) salt mixture. In the first phase of this work, experiments were conducted while varying the advancement rate, salt amount, composition, temperature, and crucible lid configurations. From each experiment, the axial concentration of CsCl was measured via Inductively Coupled Plasma-Mass Spectrometry (ICP-MS). The second phase of this thesis was data analysis and modeling. Concentration profiles of each experiment were analyzed to observe trends in the data that provided useful information on the effect of each experimental parameter. Several models were explored which yielded insights on the nature of zone freezing as well as providing researchers with values for the segregation coefficient and boundary layer thicknesses under varying conditions. The overall goal of this thesis is to gain greater insights of zone freezing and to develop a modeling tool that can be used in process optimization.

1.2 Motivation

One of the major challenges faced by the nuclear industry is used nuclear fuel disposal and management. The United States utilizes a once through fuel cycle because of the announcement made by President Carter in 1977 that all reprocessing be discontinued due to non-proliferation issues [**1**]. The once through fuel cycle is wasteful, with less than five percent of the uranium being used for power production [**2**]. In addition, storage of used nuclear fuel poses safety and engineering challenges. In 2001, President Bush recommended that the United States consider reprocessing technologies that are cleaner and more proliferation-resistant [**1**]. The U. S. Department of Energy established the Fuel Cycle and Research Development Program with the mission of developing technologies to safely close the fuel cycle [**3**].

One of the reprocessing technologies explored by the U. S. Department of Energy is pyroprocessing. Pyroprocessing is a process in which the uranium is electrochemically

dissolved in a molten salt and deposited on a cathode. One major advantage to this electrochemical process is that it is impossible to separate out pure plutonium metal, making this technology very proliferation resistant. One of the current challenges with the electrochemical treatment process is the accumulation of fission products and transuranics, and sodium in the molten salt electrolyte. Over time these contaminants increase the melting point of the salt, which affects the performance of the electrorefiner. Currently, the contaminated salt is removed and mixed with zeolite and glass and formed into a ceramic waste. As a result, 2 kg of ceramic waste will be generated for every kilogram of used fuel processed [**4**].

Researchers at the Korea Atomic Energy Research Institute (KAERI) have proposed a zone freezing method for the separation of fission products from the molten salt that may reduce the amount of ceramic waste generated **[5-6]**. Work conducted at KAERI focused primarily on feasibility, and several parameters were left unexplored. The main motivation of this thesis work is to parametrically explore zone freezing parameters and develop a modeling tool that can be used for process optimization. Understanding and optimizing the zone freezing process would make pyroprocessing technology more attractive from a waste management perspective.

1.3 Approach

Zone freezing experiments were conducted using a LiCl-KCl base salt with added impurities of CsCl and cerium chloride ($CeCl_3$). In the actual pyroprocessing of used fuel, the primary heat producing fission products found in the salt are Cs-137 and Sr-90. To simplify the experiments, a Cs-133 surrogate chloride salt was used. Cerium chloride was used as a surrogate to represent the trivalent actinide and rare earth chlorides. Experiments were conducted at varying concentrations of CsCl and $CeCl_3$. Combinations of CsCl and $CeCl_3$ salts were never tested in this work. The chloride salts of interest are hygroscopic; therefore, sample preparation was conducted in an inert atmosphere glove box. The crystal growing furnace also provided an inert gas atmosphere for the duration of the experiment. Concentration profiles were obtained by taking samples axially from all experimental runs, dissolving them in nitric acid, and measuring the concentration of all samples via ICP-MS.

1.4 Background

1.4.1 EBR-II

The Experimental Breeder Reactor-II (EBR-II) was a sodium cooled fast reactor developed by the Argonne National Laboratory as a successor to the Experimental Breeder Reactor-I. EBR-II was operated from 1963 to 1994 at Argonne National Laboratory-West [**7**]. The basic objective of EBR-II was to operate a metal cooled fast reactor to produce power while operating on recycled fuel. EBR-II was built with the intention that used fuel be reprocessed onsite into new fuel assemblies. Onsite reprocessing of fuel occurred from 1965 to 1969 using a melt refining process [**8**].

The core configuration of EBR-II consisted of driver fuel assemblies surrounded by a blanket fuel assembly. The driver fuel was composed of an enriched uranium metal alloy that was sodium bonded to stainless steel cladding. Blanket fuel consisting of depleted uranium was placed around the core with the purpose of breeding additional fuel. Traditionally, aqueous reprocessing technology has not been effective for treating EBR-II fuel because of the violent reaction between water and sodium metal. In addition, aqueous processes are large and not feasible for onsite reprocessing.

1.4.2 Pyroprocessing

To treat used fuel from the EBR-II reactor, a compact and "dry" process was developed by Argonne National Laboratory called pyroprocessing (see Figure 1.1). At the heart of the process is the Mk-IV electrorefiner—consisting of a stainless steel basket anode, a molten salt electrolyte, and a stainless steel cathode. Chopped used driver fuel is loaded into the anode basket. Current is then applied to electrochemically dissolve uranium into the electrolyte, transport and deposit onto the cathode. The cathode is removed from the electrorefiner and further processed resulting in a pure uranium product. The used fuel cladding is also removed and mixed with zirconium metal to form a metal waste. Over time, the electrolyte in the electrorefiner becomes contaminated with fission products and other rare earth and transuranic chloride salts. Currently, the used salt is removed, mixed with zeolite and made into a ceramic waste form **[9-12].**

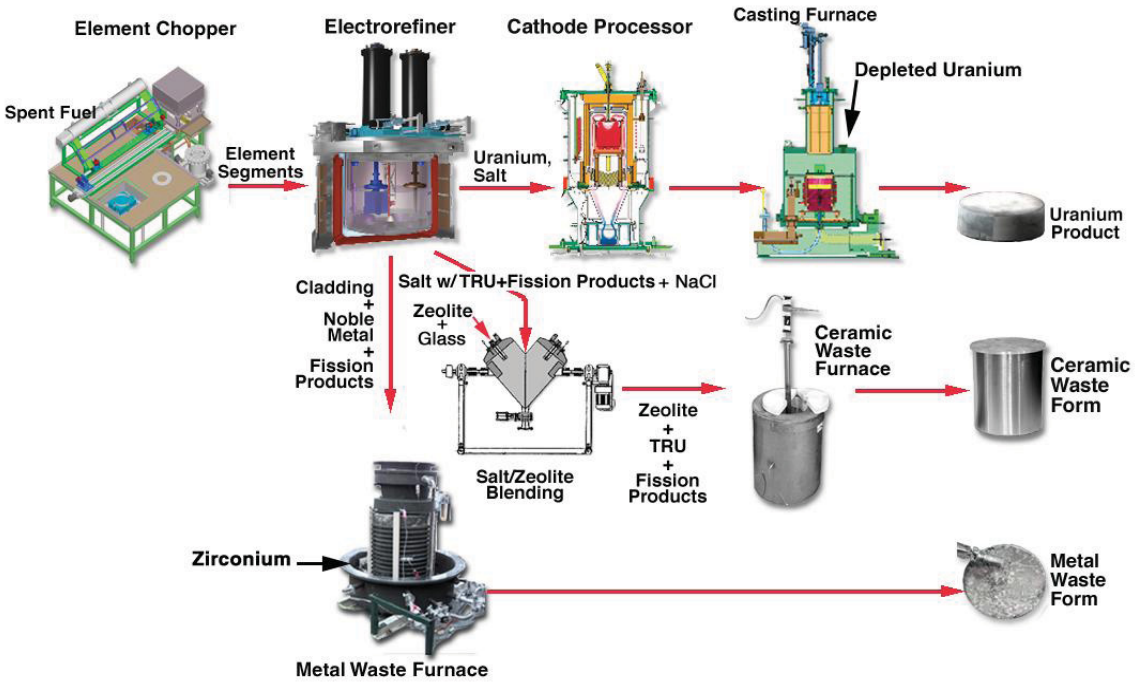

Figure 1.1: Conceptual schematic of current pyroprocessing technology.

1.4.3 Proposed Molten Salt Purification Techniques

Various treatment processes for the molten salt electrolyte have been proposed and explored—one of these is the ion exchange. Ideally, the contaminated molten salt is transferred from the electrorefiner and through a series of columns filled with zeolite-4A. Cesium and strontium ions would then be removed from the salt by the zeolite material in the columns and the exit salt would be returned to the electrorefiner. Fundamental studies on this process have been conducted at equilibrium **[13-17]**, and transient conditions [**18**]. Results from these studies indicate that the ion exchange process could effectively reduce waste volume by a factor of two [**19**].

Recently, KAERI proposed a salt purification method called zone freezing [**5**]. Zone freezing is a melt crystallization process where the contaminated electrorefiner salt is melted and then slowly cooled from the top downwards (see Figure 1.2) as in the reverse vertical Bridgman method [**20**]. Impurities in the salt solidify at a lower temperature than the LiCl-KCl salt and thus tend to concentrate in the melt phase. Once all the salt has been solidified, the bottom portion of the salt containing the bulk of the impurities can be sectioned and mixed with zeolite to form a ceramic waste. The upper

portion of the grown crystal is relatively pure LiCl-KCl and can be returned to the electrorefiner for further use. KAERI has shown that up to 90% of the electrorefiner salt can be recycled via this method, thus reducing the waste by a factor of ten [**5**].

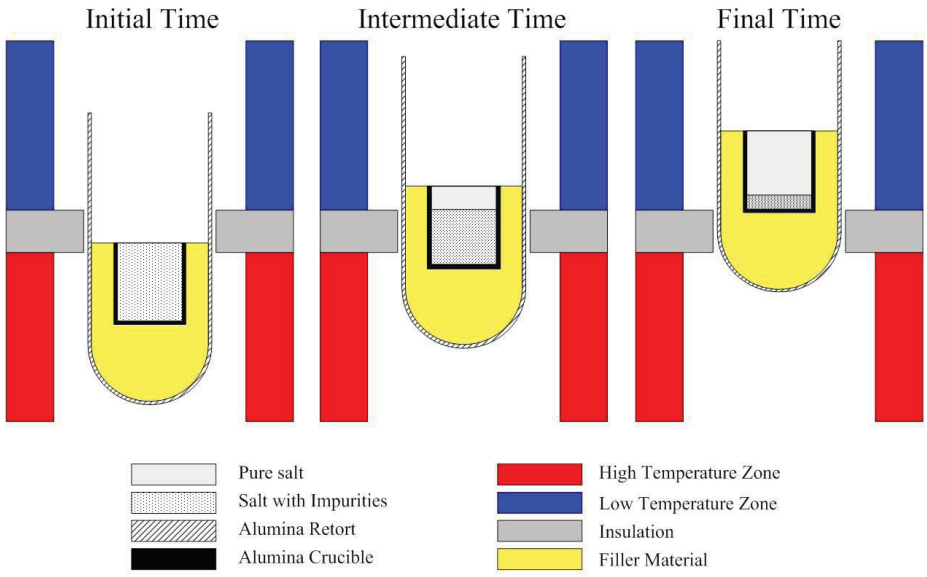

Figure 1.2: Schematic of zone freezing process.

1.5 Organization of Thesis

Chapter 1 of this thesis provides the purpose, motivation, and background information of this work. In Chapter 2, several melt crystallization models and their applicability to zone freezing are discussed. Chapter 3 describes the experimental setup, conditions, equipment, and procedures. In Chapter 4, the experimental results are presented, analyzed, and discussed. In Chapter 5, the modeling results are presented and comparisons between the models and experimental data are discussed. Chapter 6 contains a summary and recommendations of this thesis work.

Chapter 2 Crystallization Theory and Modeling

2.1 Crystallization Processes and Theory

2.1.1 Melt Crystallization Processes

Crystallization is used extensively in industry as a separation method for various materials such as semiconductors, metals, organics, and water. Two main categories of crystallization are solution and melt crystallization processes. In general, solution processes involve chemical reactions, or simply changing solvent compositions to induce crystal growth of the desired products. In melt crystallization processes, the driving force for crystallization is typically thermally induced by cooling of the liquid phase **[21-22]**.

Melt crystallization can be further divided into two separation methods: suspension and solid layer crystallization. Suspension type crystallization is designed as a continuous process where the feed material is fed through a crystallizer (similar to a heat exchanger) and then through wash columns to separate the solid material from the liquid phase. In solid layer crystallization, the product is grown on a surface layer by layer (for examples, the falling film crystallizer or the wall crystallizer **[22-23]**). However, most solid layer growth methods are batch processes like the zone melting [**24**], Czochralski [**25**], and Bridgman [**20**] crystallization techniques.

In zone melting, the material is initially solid and a heater is slowly advanced down the axis of the crucible melting the material in its path [**24**]. As the heated zone advances, the melted material refreezes leaving a small molten region, as shown in Figure 2.1. As the melted zone advances, impurities are pulled along in the melt phase, and ultimately solidify at one end of the crucible. Because of the thin melt zone, this process is generally diffusion dominated; that is, the effect of convection is limited. One advantage of zone melting is the ability to make multiple passes on the same material **[26-27]**. With each pass, the impurities in the material will continue to concentrate at one end. After processing the material via zone melting, the end with the bulk of the impurities can be removed leaving a high purity product material.

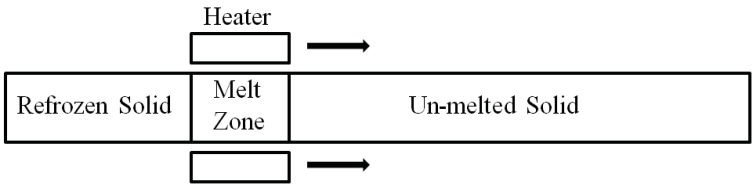

Figure 2.1: Schematic of zone melting process.

The Czochralski growth technique is widely used in the semiconductor and optics industries to create high purity, single crystal products for electronic devices [**28**]. In Czochralski growth, a seed is introduced into a melt and slowly pulled as the crystal grows. The growing crystal is usually rotated to provide mixing of the liquid phase [**29**]. The Czochralski method has been used by Lee et al. [**30**] to separate CsCl from a LiCl salt mixture. Results showed that high purity LiCl salt could be recovered via this method.

The Bridgman crystal growing technique is also an effective method for growing crystals from a melt. The driving force for crystallization via Bridgman growth is an imposed temperature gradient. Typically, the temperature gradient is made using a low temperature zone and a high temperature zone separated by an adiabatic zone. By controlling the zone temperatures, the temperature gradient in the crystallizer can be adjusted. Crystallization of the melt is initiated by slowly advancing the material through the temperature gradient. Several different Bridgman configurations have been used in the past; they are horizontal [**31**], vertical [**32**], and reverse vertical [**6**]. The difference between the vertical and reverse vertical configurations is the direction of the temperature gradient with respect to gravity. In the vertical method, the low and high temperature zones are on the bottom and top, respectively. The reverse vertical method is simply a reversal of the high and low temperature zones. A crystal seed can be used to initiate crystal growth using the Bridgman technique, but it is not necessary [**20**].

2.1.2 Phase Diagrams and Maximum Yields

A key step in determining the feasibility and maximum yields of a crystallization process is a careful analysis of a phase diagram. The phase diagram maps out the temperatures, compositions, and pressures in which different phases or mixtures of phases exist at equilibrium conditions.

Most crystallization processes do not occur at equilibrium; however, an equilibrium phase diagram is useful in providing researchers with an idea of appropriate operating conditions and maximum product yields [**33**]. A phase diagram of hypothetical compounds A and B, as shown in Figure 2.2, can be used as a demonstrative example of the basic concept. Here, it is desired to separate A from B in a mixture at composition C_I. The liquid of A and B is cooled from point T_0 to T_1 without any change in composition. With further cooling, the liquidus line is intercepted and crystals of A with a small amount of B begin to form. At temperature T_2, the composition of the liquid is shown by point C_L and the composition of the crystals is shown by point C_S. Here, the fraction of the solution crystallized can be determined using the inverse lever rule [**34**]. The inverse lever rule in this case gives: (kg of crystals A)/(kg of original solution) = $(C_I-C_L)/(C_S-C_L)$. With further cooling below T_3, crystals of A and B will form at composition C_E. Point C_E is known as the binary eutectic point. At the eutectic point the compositions of the species at the eutectic temperature will solidify simultaneously. In a separations process for this system, the maximum product yield can be found using the inverse lever rule at T_3. Also, it is important to operate the crystallizer between T_1 and T_3 if mostly crystals of A are desired.

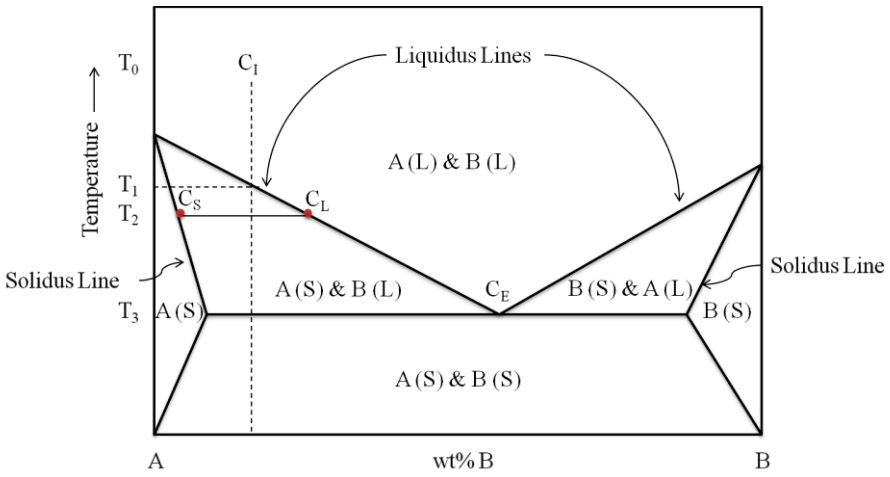

Figure 2.2: Binary phase diagram for a hypothetical system of components A and B.

A common parameter used in melt crystallization is the equilibrium segregation coefficient k_0. k_0 is defined as the ratio of the solute concentration in the solid to that of the liquid ($k_0 = C_S/C_L$) when the two phases are in equilibrium. Figure 2.2 shows that the

value of k_0 depends on the slopes of the liquidus and solidus lines. In this example, k_0 is constant throughout the crystal growing process because the slopes of the lines do not change. In real systems where the slopes are not constant, k_0 will change as a function of the melt temperature.

The phase diagram for the ternary salt CsCl-LiCl-KCl system is shown in Figure 2.3. The temperature at the ternary eutectic point E is 260°C with compositions of (57, 25, and 18) wt% or (29, 51, and 20) mol% for CsCl, LiCl, and KCl, respectively. The initial composition of the salt used in zone freezing is shown at point I on the diagram. In a crystallization process, the temperature of the melt is dropped to approximately 350°C where the binary eutectic line (line IE) is reached and components LiCl and KCl start to solidify. With further cooling, the liquid composition is enriched with component CsCl until the ternary eutectic point E is reached, and at which point no further separation can occur. Using the inverse lever rule, the maximum yield of a salt sample of 100 g with an initial composition of 3 wt% CsCl is shown below,

$$\frac{\text{kg (LiCl - KCl)}}{100\ \text{kg}} = \frac{0.03 - 0.57}{0 - 0.57} = 94.7\,. \qquad \text{Eqn. 2.1}$$

This shows that approximately 95% of the salt can be recycled. Thus, the separation via a crystallization method is feasible.

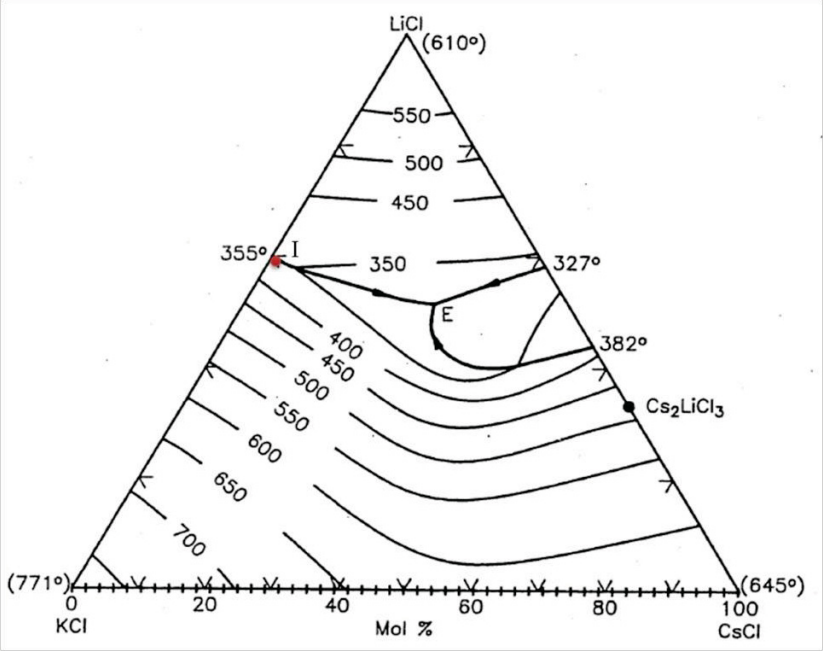

Figure 2.3: Phase diagram of the ternary CsCl-LiCl-KCl salt system [**35**].

Since the LiCl and KCl salts are at the eutectic composition, a pseudo binary phase diagram can be approximated for the ternary CsCl-LiCl-KCl salt. Along the LiCl-KCl eutectic line, three temperatures are specified; they are, 355°C at zero mol% CsCl, 350°C at approximately 4 mol% CsCl, and 260°C at 29 mol% CsCl. These three points were converted to mass fractions and plotted as shown in Figure 2.4. The resulting line is an approximation to the liquidus line of the pseudo binary phase diagram for CsCl. Sangster and Pelton [**36**] suggested a method (see Eqn. 2.2) for estimating the slope of the solidus line,

$$\frac{d\chi^{l}_{A}}{dT} - \frac{d\chi^{s}_{A}}{dT} = \frac{\Delta H_{fusion,A}}{R_g \left(T_{melt,A}\right)^2} \qquad \text{Eqn. 2.2}$$

where χ is the mol fraction of pure A, superscript l is for liquidus, superscript s is for solidus, $\Delta H_{fusion,A}$ is the heat of fusion of pure A, R_g is the univesal gas constant, and $T_{melt,A}$ is the melting temperature of pure A. Using Eqn. 2.1, the slope ($d\chi^{s}_{A}/dT$) of the solidus line was calculated to be zero. In other words, all solid formed prior to the ternary eutectic at equilibrium conditions contains no CsCl ($C_S = 0$); therefore, k_0 is zero for this system.

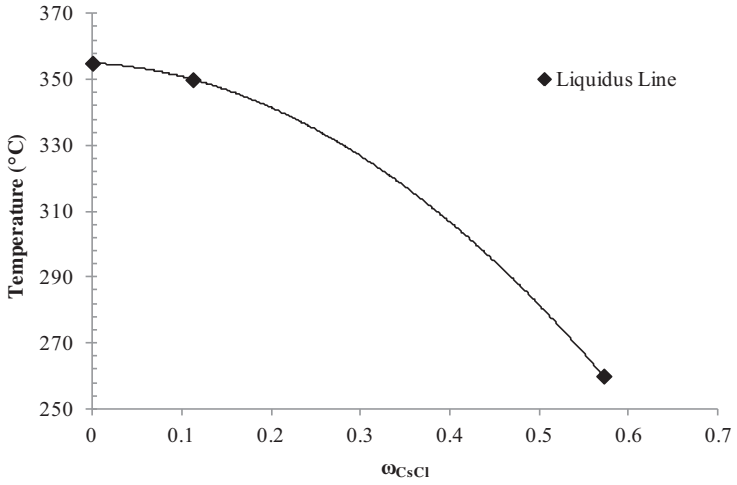

Figure 2.4: Pseudo Binary phase diagram for the CsCl-LiCl-KCl system. The LiCl and KCl are at the eutectic composition throughout.

A ternary phase diagram for $CeCl_3$-LiCl-KCl salt is shown in Figure 2.5 [**37**]. For this system, two ternary eutectic points exist and are indicated on the diagram at E1 and E2. In the crystallization of used electrorefiner salts, E2 is the eutectic point of interest at 340°C. The composition of salt at E2 is 13.6 wt% $CeCl_3$, 35.6 wt% LiCl, and 50.8 wt% KCl. Typical salt composition of used salt from the electrorefiner are shown as point I on the diagram. A pseudo binary phase diagram was computed for this system and the solubility of the solid is limited with k_0 being approximately zero. Again, assuming a 100 g sample with an initial composition of 3 wt% $CeCl_3$ and applying a similar approach, the maximum yield can be calculated to be approximately 78 g of pure eutectic salt recovered with 22 g of waste salt.

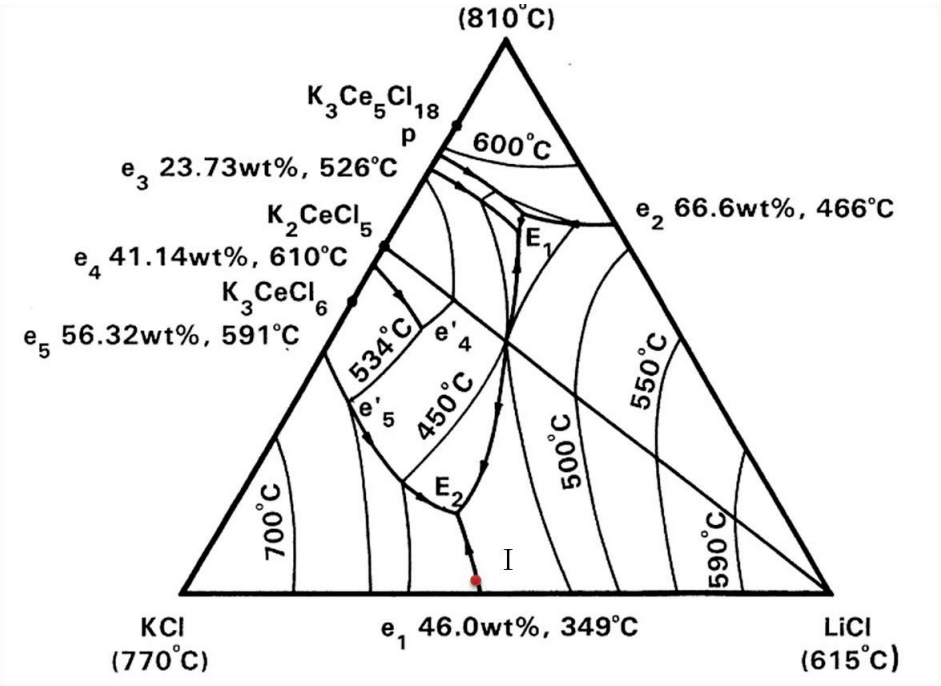

Figure 2.5: Ternary phase diagram of the $CeCl_3$-LiCl-KCL salt system [**37**].

2.1.3 Fundamentals of Phase Separation

Phase equilibria thermodynamics provides valuable insights on non-equilibrium crystallization. Equilibrium between two phases exists when the chemical potential (or Gibbs free energy) of each component in a single phase is equal to the chemical potential of the components in the adjacent phase [**38**]. In non-equilibrium crystallization, the Gibbs free energy of the solute in the solid phase is greater than its Gibbs free energy in the liquid phase as shown in Figure 2.6 **[39-40]**. As solidification occurs, the difference between the solid and liquid Gibbs free energies drives the solute into the liquid phase [**41**]. If the crystal growth rate is slow, and solute atoms have time to diffuse from the solid crystal lattice, then a relatively pure crystal can be grown. Cases where the crystal growth rate is faster than the movement of impurity atoms from the crystal result in solute trapping [**42**]. The kinetics of solute rejection is not well understood and models typically rely on empirical data.

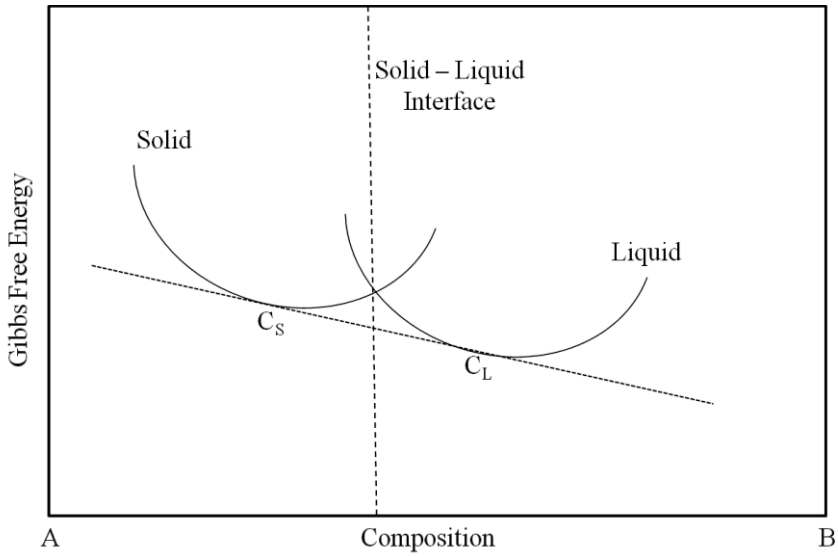

Figure 2.6: Gibbs free energy plot for a hypothetical material A-B

2.2 Melt Crystallization Modeling

2.2.1 The Scheil Equation or Well-Mixed Model

A model developed by Scheil [**43**], and later Pfann [**27**], has been used widely to describe solute concentration in the solid phase. In the system modeled by Scheil, the assumption was made that the liquid phase was well-mixed and that no concentration gradients existed in the liquid. A segregation coefficient (k), which is the ratio of the concentrations in the solid to the liquid at the interface, was used to describe the solute distribution. If equilibrium conditions prevail at the interface (solute rejection kinetics are fast), then k_0 may be used. If solute rejection kinetics are slow, then k is an empirically determined parameter that accounts for kinetics. Figure 2.7 shows a representation of a well-mixed system. Region 1 represents the amount of solute rejected with a small change in the fraction solidified (f_S). Region 2 represents the change in the bulk composition. A mass balance on the system yields:

$$(C_L - C_S)df_S = (1 - f_S)dC_L \qquad \text{Eqn. 2.3}$$

where C_L, C_S, df_S and dC_L are the liquid concentrations, solid concentrations, differential fraction solidified, and the differential change in concentration in the liquid, respectively. Since $k = C_S/C_L$, Eqn. 2.3 can be expressed as:

$$C_L(1-k)df_S = (1-f_S)dC_L \qquad \text{Eqn. 2.4}$$

Using the initial condition of $C_L = C_0$ at $f_s = 0$ and rearranging Eqn. 2.4, the following integration can be done:

$$\int_0^{f_S} \frac{1}{1-f_S} df_S = \frac{1}{1-k} \int_{C_0}^{C_L} \frac{1}{C_L} dC_L \qquad \text{Eqn. 2.5}$$

to yield,

$$C_L = C_0(1-f_S)^{k-1} \qquad \text{Eqn. 2.6}$$

The solid concentration is then obtained by substituting C_S/k for C_L. The resulting equation shown below is the Scheil Equation [**43**].

$$C_S = kC_0(1-f_S)^{k-1} \qquad \text{Eqn. 2.7}$$

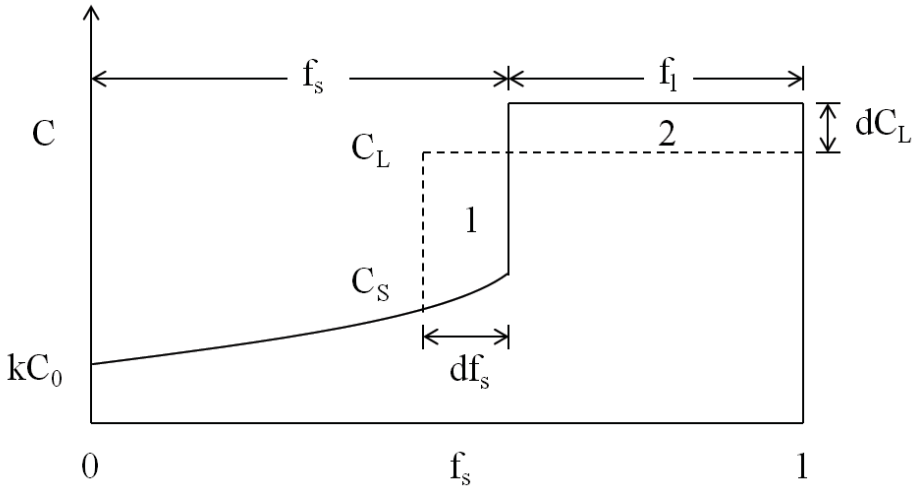

Figure 2.7: Drawing representing the solute concentration in a well mixed case.

2.2.2 The Non-Mixed Model

The idea behind the non-mixed model began with the constitutional supercooling theory proposed by Rutter and Chalmers in 1953 [**44**]. According to Rutter and Chalmers, in non-equilibrium crystal growth, the rejected solute atoms create a concentration gradient in the liquid as shown in Figure 2.8. Because of the concentration gradient, the liquidus temperature of the melt is greater than the actual temperature of the

specimen. As a result, spontaneous solidification of the solute into the solid may occur. Tiller et al. [**45**] used the concentration gradient or buildup of the solute in the liquid phase as the basis for their model. Yet, in this model, the segregation coefficient used is k and once again if equilibrium conditions prevail at the interface, then $k = k_0$.

The model developed by Tiller et al. had several key assumptions, which are: (1) solute diffusion in the solid is negligible, (2) k is constant, and (3) convection in the liquid is negligible. The first assumption is reasonable because in real systems the diffusion in a solid is typically significantly smaller than in the liquid. The second assumption is valid when the kinetics is fast such that an average k value can be used. With the third assumption, this model is only valid for convection-free systems.

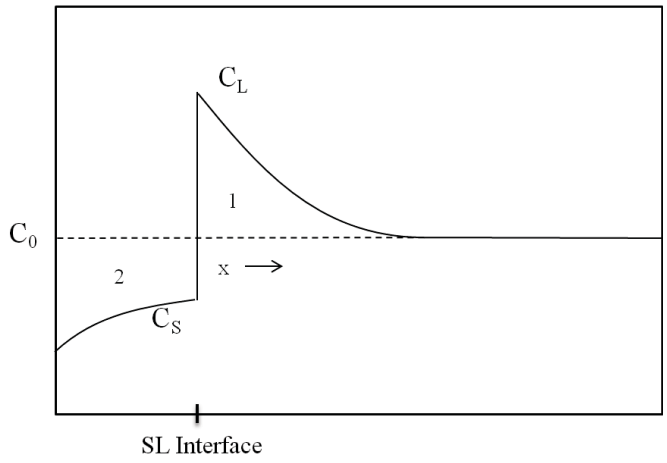

Figure 2.8: Schematic of the solute concentration profile with respect to the solid and liquid phases.

Thus, Tiller et al. performed a shell balance to derive the governing differential equation for the concentration profile in the liquid phase. In the differential volume, the amount of solute transport by diffusion into the area at face x can be expressed by using Fick's first law; that is, $J_x = -D(dC/dx)_x$, where D is the diffusion coefficient, C is the concentration, and x is the position. Due to solute rejection at the solid-liquid interface, a bulk movement of solute from the wall at the rate of growth (R) will occur. Therefore, the total flow of solute due to diffusion and advection at face x is $J_x = -[D(dC/dx) + RC]_x$ and the amount leaving at $x+\Delta x$ is $J_{x+\Delta x} = -[D(dC/dx)+RC]_{x+\Delta x}$. The net concentration of solute in the differential volume is described by:

$$D\frac{d^2C}{dx^2}+R\frac{dC}{dx}=0 \qquad \text{Eqn. 2.8}$$

The origin is defined as the solid-liquid interface. Boundary conditions are as follows: $C_L = C_a+C_0$, at $x = 0$ and $C_L \rightarrow C_0$, as $x \rightarrow \infty$ where C_0 is the initial concentration and C_a is the liquid concentration at the interface less the initial concentration. Solving Eqn. 2.8 with the above boundary conditions yields:

$$C_L = C_a \exp\left(-\frac{R}{D}x\right)+C_0 \qquad \text{Eqn. 2.9}$$

The value of C_a can be determined by using the steady state assumption. In this system, it is expected that the solid concentration, C_S, rises from the initial value of kC_0 to some steady state value. Here, the amount of solute entering the interface is the same as that of leaving; therefore, $C_S = C_0$. Using the segregation coefficient, C_a is equal to $C_0/k\text{-}C_0$. Substitution into Eqn. 2.9 yields:

$$C_L = C_0\left(1+\frac{1-k}{k}\exp\left(-\frac{R}{D}x\right)\right) \qquad \text{Eqn. 2.10}$$

Next, Tiller et al. assumed that the rate of approach of C_S to C_0 with x is proportional to $(C_0 - C_S)$. Therefore,

$$\frac{d}{dx}(C_0-C_S)=-\alpha(C_0-C_S) \qquad \text{Eqn. 2.11}$$

where α is the proportionality constant. Eqn. 2.11 can be solved with the following boundary condition: at $x = 0$, $C_S = kC_0$ and the solution is

$$C_S = C_0 - C_0(1-k)e^{-\alpha x} = C_0\left((1-k)\left(1-e^{-\alpha x}\right)+k\right). \qquad \text{Eqn. 2.12}$$

The latter form has been presented by Tiller et al. [**45**]. Here, as $x \rightarrow \infty$, $(C_0\text{-}C_S)$ becomes zero. The value of α can be determined by equating the areas 1 (A_1) and 2 (A_2) shown in Figure 2.8. A_1 is found by integrating Eqn. 2.10 from zero to infinity and subtracting the result from $C_0(\infty)$. A_2 is found by subtracting the integral of Eqn. 2.12

(evaluated from zero to infinity) from $C_0(\infty)$. Areas 1 and 2 are shown below, respectively

$$A_1 = C_0 \frac{1-k}{k}\frac{D}{R} \quad \text{and} \quad A_2 = \frac{1}{\alpha} C_0 (1-k) \ . \qquad \text{Eqn. 2.13}$$

Equating A_1 and A_2 and solving for α yields, $\alpha = kR/D$. Substituting the value of α into Eqn. 2.12 yields the non-mixed model as shown below:

$$C_S = C_0 \left((1-k) \left[1 - \exp\left(-k \frac{R}{D} x \right) \right] + k \right) \qquad \text{Eqn. 2.14}$$

It should be mentioned that one drawback of Eqn. 2.14 is that it cannot account for end effects in the material. Qualitatively, the amount of solute in the diffusion boundary layer will deposit at the end of the growing specimen, but no effort was made by Tiller et al. to calculate the ending profile.

2.2.3 Convection-Diffusion Models

In most practical applications, the mixing of the solute is neither complete nor diffusion dominated. Burton and co-workers **[46-47]** studied the effects of forced convection in Czochralski type crystal growth. According to Burton et al., convection and diffusion play important roles in crystallization. For example, in a well-mixed system, the convection dominates the solute distribution far from the growing interface. However, at and near the solid-liquid interface, the fluid velocity is zero due to the no-slip boundary condition and diffusion dominates. As a result, diffusion through this boundary layer is the limiting factor of solute distribution (solute rejection kinetics aside). Burton et al. described the concentration in the boundary layer using Eqn. 2.8, following the same approach as Tiller et al. did **[45]**, with the new proposed boundary conditions,

$$D\frac{dC}{dx} = -R(C_L - C_S), \text{ at } x = 0 \quad \text{and} \quad C = C_B, \text{ at } x = \delta \qquad \text{Eqn. 2.15}$$

where C_B is the bulk concentration and δ is the boundary layer thickness. Therefore, the solution to Eqn. 2.8 becomes

$$\frac{(C_L - C_S)}{(C_B - C_S)} = e^{\Delta} \qquad \text{Eqn. 2.16}$$

where Δ represents $R\delta/D$. They defined an effective segregation coefficient (k_{eff}) as the ratio of the concentration of the solute in the solid to the bulk liquid (C_S/C_B). Using k_{eff} and k, Eqn. 2.16 can be manipulated to get:

$$k_{eff} = \frac{k}{k + (1-k)e^{-\Delta}} \qquad \text{Eqn. 2.17}$$

When the equilibrium condition at the interface prevails, k can be replaced with k_0.

One key advantage of k_{eff} is that it links the effects of equilibrium and kinetics for solute separation with the diffusion/convection effects. For example, if Δ is known, k can be determined empirically by using a linear regression method. Conversely, if k is known, then Δ can be determined empirically. If neither k or Δ is known, then k_{eff} can be found empirically and represents the net contributions of the kinetic and transport effects. As a result, k_{eff} can be a useful parameter in melt crystallization modeling.

Favier **[48-49]** continued the work conducted by Burton et al. by developing an expression using k_{eff} to describe the solid concentration for non-steady state conditions that would work regardless of any dominant transport regimes (diffusion, convection, or a mixture of the regimes). One major assumption made by Favier is that equilibrium prevails at the interface. The governing equation (see Eqn. 2.18) used by Favier to describe the concentration in the liquid phase is Fick's second law with the coordinate system applied at the solid-liquid boundary.

$$\frac{\partial C}{\partial t} = D\frac{\partial^2 C}{\partial x^2} + R\frac{\partial C}{\partial x} \qquad \text{Eqn. 2.18}$$

where t is time and x is the distance in front of the solid-liquid interface. It is possible to transform Eqn. 2.18 into the dimensionless form by defining $\xi = 1\text{-}x/\delta$, $\tau = t/(\delta/R)$, and $C = C_L/C_0$ and substituting them into the equation. Here, the origin is transformed from the solid-liquid interface to the point $x = \delta$ with positive ξ towards the interface. With this substitution, Eqn. 2.18 becomes

$$\frac{\partial C}{\partial \tau} = \frac{D}{\delta R}\frac{\partial^2 C}{\partial \xi^2} - \frac{\partial C}{\partial \xi} \qquad \text{Eqn. 2.19}$$

subject to following initial and boundary conditions:

$$C(\xi,0) = 1, \text{ for } \tau = 0 \qquad \text{Eqn. 2.20}$$

$$C(0,\tau) = \frac{C_B}{C_0}, \text{ for } \xi = 0 \qquad \text{Eqn. 2.21}$$

$$\frac{\partial C}{\partial \xi} = \Delta(1-k)C, \text{ for } \xi = 1 \qquad \text{Eqn. 2.22}$$

Favier solved Eqns. 2.19 using Eqns. 2.20 – 2.22 analytically to get:

$$C_S(\tau) = k_{eff}\left(1 - \frac{8(1-k)\left[k+(1-k)e^{-\Delta}\right]}{\Delta} \times \sum_{i=1}^{\infty} \frac{\sin^2\alpha_i \exp\left(-\frac{\beta_i \Delta\tau}{4}\right)}{\beta_i\left(1 - \frac{2\cos^2\alpha_i}{(1-k)\Delta}\right)}\right), \text{ for } \tau < \tau^* \qquad \text{Eqn. 2.23}$$

and

$$C_S(\tau) = C_S(\tau^*) + \frac{k_{eff}}{1-k_{eff}}\left[1 - C_S(\tau^*)\right] \times \left[\left(\frac{h_0 - \delta\tau}{h_0 - \delta\tau^*}\right)^{k_{eff}-1} - 1\right], \text{ for } \tau \geq \tau^* \qquad \text{Eqn. 2.24}$$

where α_i and β_i are roots, h_0 is the specimen length, and τ^* is the time at which a steady state is reached. The derivations of Eqns. 2.23 and 2.24 are not shown here. The roots α_i and β_i are defined as follows, if

$$\frac{(2k-1)\Delta}{2} < -1, \qquad \text{Eqn. 2.25}$$

then,

$$\alpha_i \coth\alpha_i - \frac{(1-2k)\Delta}{2} = 0 \text{ and} \qquad \text{Eqn. 2.26}$$

$$\beta_i = 1-(1-2k)^2 \tanh^2 \alpha_i . \qquad \text{Eqn. 2.27}$$

If the condition shown in Eqn. 2.25 is true, then only one root is needed. However, if Eqn. 2.25 is greater than or equal to -1, then,

$$2\alpha_i \cos\alpha_i - (1-2k)\Delta \sin\alpha_i = 0 \text{ and} \qquad \text{Eqn. 2.28}$$

$$\beta_i = 1+(1-2k)^2 \tanh^2 \alpha_i . \qquad \text{Eqn. 2.29}$$

Under these conditions, multiple roots are need.

Since $\tau = (R \cdot t)/\delta$, and R is constant, then the $R \cdot t$ term represents the distance (h) solidified. As a result, τ in Eqns. 2.23 - 2.24 can be replaced by h/δ. Now the equations are in terms of the fraction solidified like the non-mixed and well-mixed models. Similarly, τ^* can be replaced by h^*/δ. The location h* occurs when the flux leaving the solid is equal to the flux arriving at the bulk liquid phase as shown below,

$$\frac{\Delta C_S(h^*)}{\Delta\tau} = \frac{k_{eff}(1-C_S(h^*))}{h_0 - h^*} . \qquad \text{Eqn. 2.30}$$

Using Eqns. 2.23 - 2.30, the solid concentration can be obtained. However, since the roots are a function of both Δ and k, curve fitting is challenging. In addition, finding h* is difficult. To ease these challenges, a program using the commercial software MATLAB was created to solve for the roots and h*. The roots are found using the built in function fzero (root finder). The location h* was found iteratively using Eqn. 2.30. This program allows for the easy computation of the analytical solution. The full program and subroutines are shown in Appendix A.

2.2.4 Determining the Boundary Layer Thickness

The usefulness of boundary layer models as proposed by Burton et al. [**46**] and Favier [**48**] has been limited due to challenges in determining the boundary layer thickness. Camel and Favier **[50-51]** used an order of magnitude analysis technique to identify several transport regimes (as a function of Δ) qualitatively and to obtain concentration profiles for each regime. The key dimensionless parameters identified in their work were the Grashof number (Gr), the Peclet number (Pr), and the Schmidt

number (Sc). The Gr number is the ratio of the buoyancy forces to the viscous forces in the liquid. Gr is defined as

$$Gr = \frac{g\beta(T_h - T_c)L^3}{\nu^2} \qquad \text{Eqn. 2.31}$$

where g, β, T_h, T_c, L, and ν are the gravitational constant, the expansion coefficient, the hot temperature, the cold temperature, the characteristic length, and the kinematic viscosity of the fluid, respectively. Pe is the ratio of the advection to the diffusion and is defined as

$$Pe = \frac{rR}{D} \qquad \text{Eqn. 2.32}$$

where r is the characteristic length, R is the rate, and D is the diffusion coefficient. Sc is the ratio between the viscous diffusion rate and the molecular diffusion rate, which is

$$Sc = \frac{\nu}{D} \quad . \qquad \text{Eqn. 2.33}$$

Camel and Favier indentified the governing parameters, but their choice of the characteristic lengths was complex and the application of their findings is challenging. Garandet et al. [**52**] further addressed the parameter Δ using scaling analysis for an ideal horizontal Bridgman growth configuration. Here, the velocity profile within the liquid cavity was approximated using the Batchelor solutions [**53**] which are functions of the Gr. It is important to point out that the characteristic lengths proposed by these literature studies for Gr and Pr were the height of liquid and the crucible radius, respectively. With these approximations and lengths, Garandet et al. estimated the parameter Δ to be proportional to Pe $(GrSc)^{-1/3}$. Kaddeche et al. [**54**], using a numerical scheme, showed that Δ can be approximated by 3.6 Pe $(GrSc)^{-1/3}$.

Of more interest to this work is the later research conducted by Kaddeche et al [**55**]. on the scaling analysis of vertical Bridgman configurations. Here, the parameters were investigated numerically over a wide range of values. The approximation of Δ =

Pe $(GrSc)^{-1/3}$ was confirmed for $Gr < 5 \times 10^3$. For larger values of the Gr number, Kaddeche et al. determined that the best fit was:

$$\Delta = 33.7 Pe(GrSc)^{-1/3} \qquad \text{Eqn. 2.34}$$

Eqn. 2.33 will be used in this work to determine the parameter Δ, which can be led to the thickness of the diffusion boundary layer δ.

2.3 Numerical Models

The majority of melt crystallization models found in the literature have been numerical due to complexities of crystal growth. In this section, a brief summary of some of the numerical models will be presented. Verhoeven et al. **[56-57]** solved numerically the diffusion equation for convection-free systems in rectangular, cylindrical, and spherical coordinates. In their models, solute distribution was determined using the equilibrium segregation coefficient. Results were in good agreement with Tiller et al. [**45**] and Smith et al. [**58**], who developed analytical solutions for the rectangular coordinate system. A large number of numerical crystallization models solve all the transport equations simultaneously to get the velocity, temperature, and concentration profiles in the melt. Bennon and Incropera [**59**], for example, developed a continuum model for solid-liquid phase change to solve the transport equations. Here, solute distribution was modeled using the equilibrium segregation coefficient. Other authors that solve the transport equations simultaneously using the equilibrium segregation coefficient are Chang and Brown [**60**], Voller et al. [**61**], and Kim and Brown [**62**]. Prescott et al. [**63**] and Krane and Incropera [**64**] performed experimental validations of the continuum model developed by Bennon and Incropera.

Of particular interest is a numerical model developed by Fukui and Maeda [**65**] that is completely predictive if knowledge of the equilibrium phase diagram is available. Here, the transport equations of mass, energy, and momentum are solved simultaneously. However, rather than using the segregation coefficient as many other authors, Fukui and Maeda use the theory of constitutional supercooling and an equilibrium phase diagram to predict solute segregation. Fukui and Maeda have confirmed experimentally their model

with several different geometries **[23, 66]**. They also developed a simplified numerical model where the momentum equations were approximated using scaling laws [**67**].

Whereas the above list of numerical crystallization models is in no way comprehensive, it provides a basic view of numerical models in general. The implementation of these models are challenging due the complexities of solving the momentum equations for buoyancy driven flow. For this case, the velocity field is linked to a pressure distribution within the liquid. This pressure distribution must be solved for iteratively and which adds computational complexities. As a result, none of the numerical models were considered in this. The analytical modeling approaches are simpler and can be applied without the use of a large CPU times.

Chapter 3 Experimental Methods

3.1 Parameters and Conditions

To gain a better understanding of zone freezing and to provide information that can be used to optimize the process, several parameters and conditions were selected and explored. They are: (1) amounts and compositions of salt, (2) retort advancement rates, (3) crucible lid configurations, and (4) induced temperature gradients.

Experiments were conducted using a eutectic LiCl-KCl (44 wt% LiCl and 56 wt% KCl) salt mixed with $CeCl_3$ or CsCl salts. It is important to point out that typical weight percents of $CeCl_3$ and CsCl coming out of the electrorefiner are 3.0 wt% and 3.2 wt%, respectively [**16**]. Therefore, most of the experiments in this work were conducted at 3 wt%. However, several experiments were conducted at 1 wt% and 5 wt% CsCl to explore the composition effect. The majority of the experiments were conducted using 50 g salt samples. Several runs were also conducted using 400 g samples to explore the scale up effect.

Three retort advancement rates were selected in this study: 1.8, 3.2, and 5.0 mm/hr. These rates were selected to be similar to rates used by KAERI (1.7, 2.5, and 5.7 mm/hr) [**5**]. For each of these rates, the effect of covering the salt with a magnesium oxide crucible lid was also explored (this will be referred to as the "lid configuration"). Identical experiments were conducted without using the lid and referred to as the "no-lid configuration". Finally, the induced temperature gradient was varied by adjusting the temperatures of the upper and lower furnace zones. Temperature differences of $\Delta T = 200°C$ and $\Delta T = 300°C$ were selected. In the first case, the upper and lower furnace zones were set to 250°C and 450°C, respectively. For the latter case, the upper and lower zones were set at 200°C and 500°C, respectively. Temperatures were selected so that the melting temperature of LiCl-KCl (352°C) was an average of the temperature zones.

3.2 Equipment

The apparatus used in the zone freezing experiments was purchased by the Idaho National Laboratory from OXY-GON Industries, Inc. and is shown in Figure 3.1. The apparatus has two fully programmable furnace zones that are divided by an adiabatic

zone. Each furnace zone has an effective heating height of 30.0 cm and can operate up to 1000°C. The adiabatic zone thickness can be adjusted from 2.5 cm to 10.0 cm thick. The apparatus is equipped with an alumina retort tube (90.0 cm height × 7.0 cm diameter) that passes through the furnace zones and can be sealed to maintain a vacuum or inert gas atmosphere. By the manufacturer's recommendations, a temperature gradient no more than 80°C per centimeter should be applied to the retort across the adiabatic zone. As a result, the insulation thickness in the adiabatic zone was set at 2.5 cm and 5.0 cm for of the ΔT of 200°C and the ΔT of 300°C, respectively. During operation, the retort is initially at its lowest setting (in the high temperature zone) and then slowly drawn upwards through the furnace zones via a translation mechanism that is fully programmable to operate at advancement rates as low as 0.5 mm/hr.

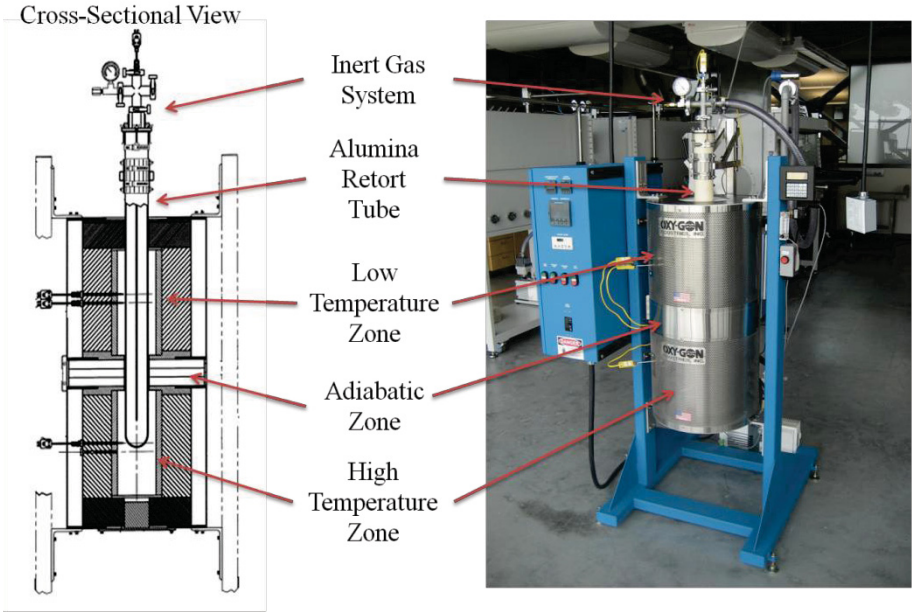

Figure 3.1: Zone freezing apparatus cross-sectional view and photo showing the various apparatus components.

Salt preparation was conducted in a sealed atmosphere glove box manufactured by MBraun. The glove box was equipped with continuous atmosphere circulators that maintain the oxygen and water content in the box less than 0.1 parts per million (ppm). The inert atmosphere gas was industrial grade argon. Salts were weighed using a Mettler Toledo NewClassic mass balance located inside the glove box.

Samples collected following each experiment were analyzed via Inductively Coupled Plasma-Mass Spectrometry (ICP-MS). The ICP-MS used was an Agilent 7500c and autosampler. Calibration of the instrument was done using an internal standard (rhodium and scandium) and external standards at varying concentrations of the element of interest. In this work, the external standards used were CCS1 (mixture containing rare earth elements) to measure Ce, and CCS4 (mixture of major-earth elements) to measure Li, K, and Cs. CCS1 and CCS4 were purchased from Inorganic Ventures in 100 µg/L concentrations. Standards were prepared at the following concentrations: (10, 30, 50, 70, 100, 200, 500, 1000, 2000, and 5000) µg/L in a 5% by volume nitric acid.

3.3 Materials and Configurations

The salts used in the experiments were LiCl, KCl, CsCl, and $CeCl_3$. These salts were surrogate (non-radioactive) and were purchased from Alfa Aesar and Rare Earth Products Inc. and had a 99.99% purity or greater. Salt materials were anhydrous beads or granules. The salts were placed in high density alumina crucibles purchased from Ozark Technical Ceramics. Two crucible sizes were used. The first measured 7.6 cm height and 3.0 cm in diameter and the second measured 20.0 cm in height and 6.0 cm in diameter. For both crucible sizes, the amount of salt was selected such that the height to diameter ratio of the salt inside the crucible was approximately 1.5. The smaller crucible size was used to hold 50 g salt mixtures. The larger size crucible contained the 400 g salt mixture. The majority of experiments were done using the small crucible size to conserve salt materials.

To accommodate the smaller crucible diameter and to assist in lowering and removing the crucible from the retort, a basket was fabricated as shown in Figure 3.2. The basket was made of an alumina-silicate material and was 10.0 cm tall and 6.8 cm in diameter allowing for an easy fit into the retort tube. The inside cavity of the basket was 7.6 cm in depth and 3.5 cm in diameter, allowing for the insertion of the smaller crucible size. The basket with crucible was lowered and removed from the retort via thermocouples inserted into the basket.

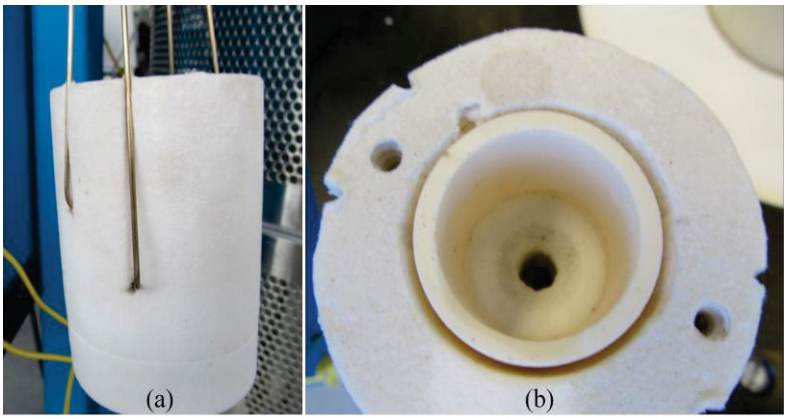

Figure 3.2: (a) Side view of alumina-silicate basket with inserted thermocouples. (b) Top view of basket with inserted alumina crucible and salt.

Four thermocouples were positioned around the crucible during experiments to provide temperature readings and profiles of the system throughout zone freezing. Thermocouples were type K, inconel sheathed, 1.5 m long and 1.5 mm in diameter, and purchased from Idaho Laboratories Inc. Thermocouples were inserted through an airtight gland at the top of the retort, and bent into the alumina-silicate basket with the probe tips just touching the outside wall of the crucible. Thermocouple one (T1) was placed at the bottom of the crucible with T2, T3, and T4 positioned at 2 cm, 4 cm, and 6 cm from the bottom, respectively (see Figure 3.3).

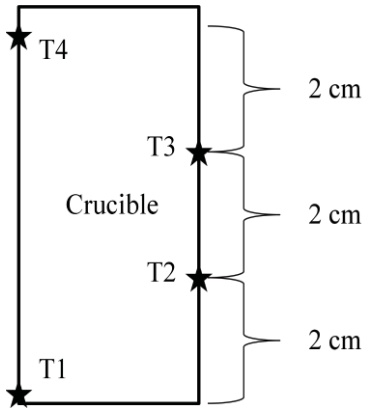

Figure 3.3: Schematic showing the positioning of the four thermocouples around the alumina crucible. Stars represent the thermocouple probe tips.

For the larger crucible size, the alumina-silcate basket was not used; however, the small gap (5 mm on each side) between the crucible and retort was filled using an alumina-silicate fiber wrapped with stainless steel wire and aluminum foil (see Figure

3.4). In this case, thermocouples were placed along the crucible wall using wire. T1 was placed at the bottom of the crucible and a 3 cm spacing was used to separate T2, T3, and T4. Thermocouples were connected to a data logger (USB-TEMP) made by Measurement Computing. The USB-TEMP was connected directly to a laptop and temperature measurements were recorded every two minutes throughout the experiment.

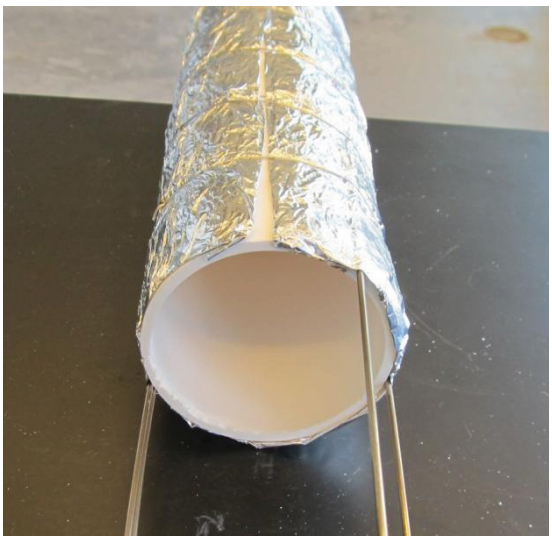

Figure 3.4: Large crucible (20 cm x 6 cm) and thermocouples wrapped in alumina-silicate fiber, aluminum foil, and stainless steel wire.

3.4 Procedure and Sample Analysis

In preparation for an experiment, the alumina crucibles were dried by slowly heating them to 150°C and leaving them at that temperature for two hours. The hot crucibles were then placed in the ante-chamber of the glove box under vacuum for two hours to remove any water and oxygen in the material. The dried crucibles were then transferred into the glove box and stored in the inert atmosphere until use.

Salts were mixed to varying compositions by mass in the glove box. The mixed salts were then placed into the crucible, covered with parafilm, and transferred out of the glove box. The crucible and salt were quickly placed inside the alumina-silicate basket, with the parafilm removed, and lowered into the retort tube. Once the crucible was positioned and the retort sealed, the retort was evacuated to less than 300 milliTorr and left for two hours. During this time, the furnace zones were ramped up to 150°C. The purpose of this step was to remove any water and oxygen that may have been absorbed

into the retort and basket materials between experiments. Following this procedure, the retort was backfilled with argon gas. The furnace zones were set at the desired temperatures and then left for 6 to 8 hours, allowing for the salt to melt and to reach equilibrium. The retort was then moved to a reference position (top of salt at the bottom of adiabatic zone) within the furnace and the translation mechanism was set at the desired rate. In a typical experiment the retort was advanced a distance of 10 cm. This corresponded to run times between 20 hours and 60 hours.

Once the salt temperatures had dropped well below the melting temperature, the retort advancement and furnace zones were powered down. The furnace required up to 18 hours to cool to ambient conditions following an experiment. The cooled crucible and salt was removed from the retort and quickly placed in a plastic bag that had been filled previously with argon gas. The salt was removed from the crucibles by solidly striking the top edge of the crucible with a wedge and hammer. In all cases, with one exception, the crucible could be removed without fracturing the salt ingot. The grown crystal ingot was then transferred into the inert atmosphere glove box and samples were acquired by drilling holes into the salt at select locations down the axis of the salt. Shavings from each hole were collected and stored in glass vials. The sampling method is shown in Figure 3.5.

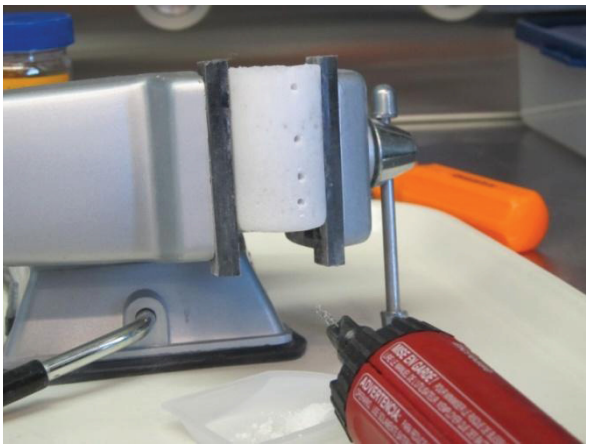

Figure 3.5: Salt sampling technique in the glove box.

The stored samples were removed from the glove box and prepared for elemental analysis via ICP-MS. Samples were weighed using a mass balance and placed into 15

mL plastic test tubes. Ten mL of 5% nitric acid was added to each sample to dissolve the salt. Dissolution of the salt occurred rapidly. Following dissolution, the samples were diluted 100× and analyzed on the ICP-MS instrument for concentrations of Li, K, Cs, and Ce. Samples were measured on the instrument at random from each experiment.

Chapter 4 Experimental Results and Discussions

4.1 Grown Crystal Characteristics

There are several common characteristics of the grown crystals resulting from the zone freezing experiments (see Figure 4.1). The most apparent characteristic is the hole through the center of the salt sample and the downward sloped top surface; which occurs as a result of volume change during solidification. The average ratio between the diameter of the hole to the outside diameter of the salt is 0.24. The average depth of the sloped portion on the top surface is 5 mm. Another interesting characteristic of the crystals is the dendritic appearance of the growth on surfaces of the salt not in contact with the crucible. Additional photos of grown crystals are shown in Appendix B.

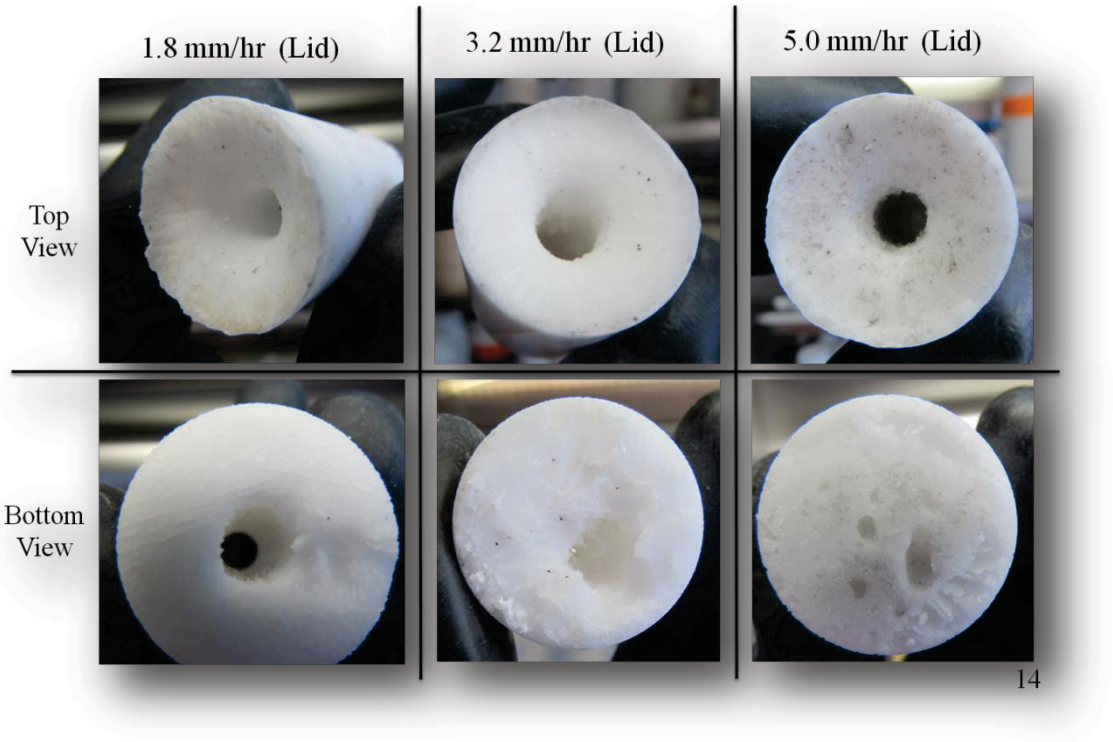

Figure 4.1: Top and bottom view of grown crystal ingots for 50 g, 3 wt% CsCl salt with a lid configuration.

4.2 Physical Properties of the Salt

In the analysis of the experimental results several physical properties of the salt are needed, which are: density (ρ), viscosity (μ), the expansion coefficient (β), and the diffusion coefficient (D). The density [**68**] of eutectic LiCl-KCl can be approximated by:

$$\rho(g/cm^3) = 2.03 - 5.27\times10^{-4}T \qquad \text{Eqn. 4.1}$$

where T stands for the temperature. The measured temperature range of Eqn. 4.1 is 680 K to 860 K. The viscosity [**68**] of the eutectic LiCl-KCl is:

$$\mu\left(\frac{mN\cdot s}{m^2}\right) = 0.08703\exp\left(\frac{2.08\times10^4}{R_g T}\right) \qquad \text{Eqn. 4.2}$$

where R_g is the universal gas constant (8.314 J/mol K). This equation is valid for the temperature ranging from 890 K to 1070 K. The expansion coefficient [**69**] is shown below:

$$\beta = -\left(\frac{1}{\rho}\right)\left(\frac{\partial\rho}{\partial T}\right) \qquad \text{Eqn. 4.3}$$

where ρ and $\partial\rho/\partial T$ can be calculated using Eqn. 4.1 at the specified temperature.

The diffusion coefficient for Cs^+ in a eutectic LiCl-KCl could not be found in the literature. However, available in the literature are several (Na^+, Cu^+, Ag^+, Au^+, and Tl^+) diffusion coefficients that can be used as an approximation. The above elements have a plus one charge as well as Cs^+ so the effect of anion diffusion should be the same. Another important factor is the atomic radius of the elements in comparison to Cs^+. The atomic radii of Cs and Rb are closely matched with radii being 260 pm and 235 pm [**70**], respectively. From this, D for Rb^+ in the molten salt has been selected to approximate Cs^+. The diffusion coefficient [**71**] for Rb^+ is shown below:

$$D\left(\frac{cm^2}{s}\right) = 1.83\exp\left[\frac{-1.65\times10^4}{R_g T}\right] \qquad \text{Eqn. 4.4}$$

The measured temperature range is from 700 K to 790 K. In zone freezing, the temperatures of interest lie below the measured temperature ranges of these equations presented above. It is assumed in this work that the equations can be used outside the measured range without major deviation from true values.

4.3 Temperature Profiles and Effects

The temperature profiles for the crucible as a function of time and position are shown in Figure 4.2 and Figure 4.3, respectively, for the 3 wt% CsCl experiment at 5.0 mm/hr. After salt melting, the retort was moved to a reference position within the furnace (defined in Chapter 3) after which the retort advancement rate was set and initiated. During the first hour of the experiment, the temperature decreased rapidly due to the rapid transition from the melting position in the high temperature zone (HTZ) to the reference position at time zero. After this initial transient period, the temperature profile maintained a relatively constant slope until the top salt surface entered the low temperature zone (LTZ) at approximately 50 mm of displacement. Once the salt entered the LTZ the temperature decreased more rapidly. Temperature profiles for all rates and conditions are shown in Appendix C.

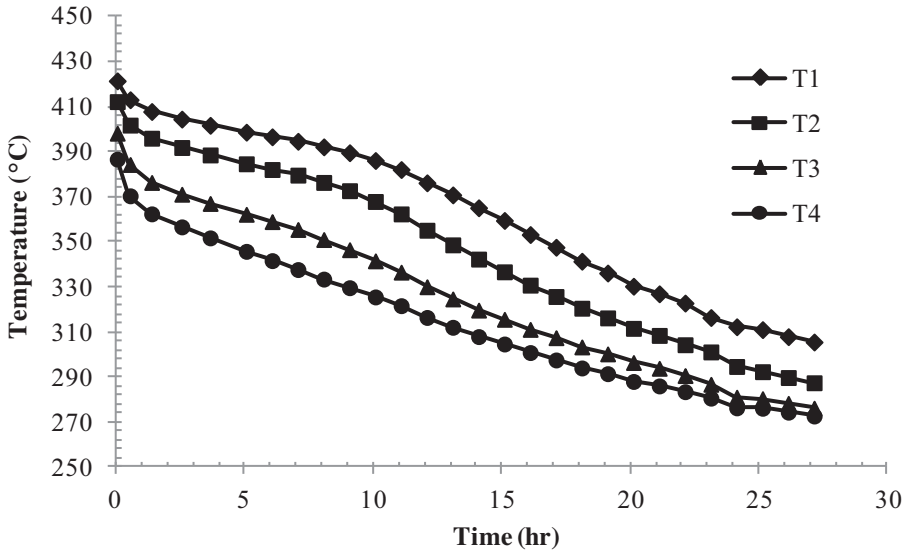

Figure 4.2: Temperature profile along the crucible edge as a function of time for the 3 wt% CsCl at 5.0 mm/hr rate. 50 g of salt were used with a no-lid configuration and a ΔT of 200°C.

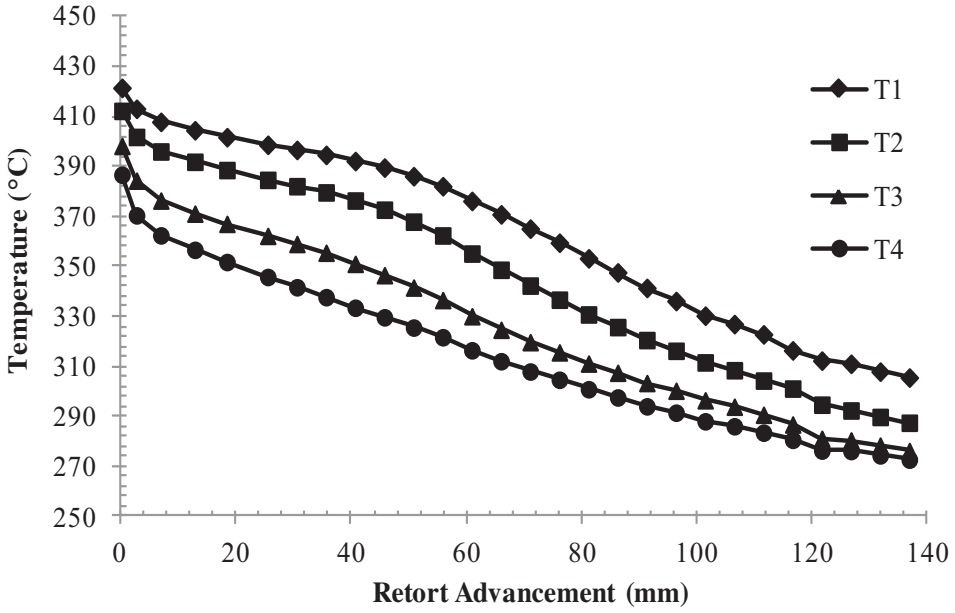

Figure 4.3: Temperature profile along the crucible edge as a function of the calculated retort position for the 3 wt% CsCl at 5.0 mm/hr rate. 50 g of salt were used with a no-lid configuration and a ΔT of 200°C.

Temperature profiles were compared for all three moving rates by plotting them as a function of the retort advancement. Figure 4.4 shows the comparisons between rates for the 50 g samples with 3 wt% initial CsCl experiments with the lid configuration. For ease of comparison, only T1 and T3 are shown because (1) the same trends observed with T1 and T3 were also similar to those observed in T2 and T4 and (2) they represent regions closest to the salt within the crucible. In the case of the lid configuration, the variations between rates show small differences initially and with increasing differences during the latter half of the experiment. Interestingly, the temperature at the 5.0 mm/hr rate falls between those at the 1.8 mm/hr and 3.2 mm/hr rate after approximately 50 mm of retort advancement (after exiting the adiabatic zone). However, the largest percent difference between the temperatures of each rate and the average temperature was only 1.3%.

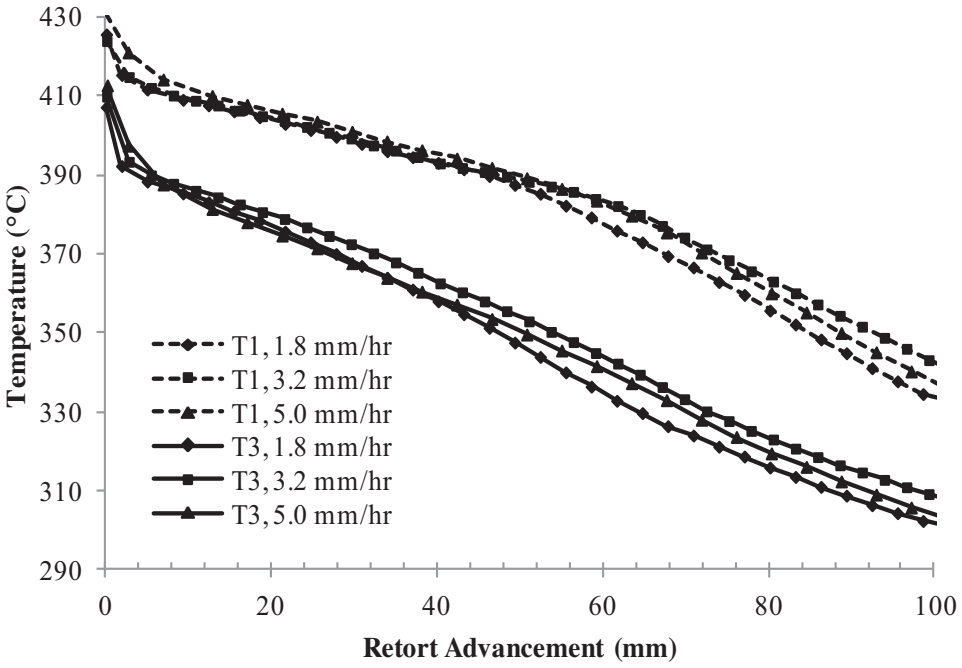

Figure 4.4: Comparison of the (1.8, 3.2, and 5) mm/hr rates for the 3 wt% CsCl experiments while using a lid configuration. $\Delta T = 200°C$ and 50 g.

Temperature profiles obtained at the different rates were compared to the other zone freezing conditions. For the no-lid configuration, the temperature profiles were nearly indistinguishable with the largest percent difference being 0.5%. A slightly larger difference was observed for the 400 g case. The 5.0 mm/hr profile was bracketed by the 1.8 mm/hr and 3.2 mm/hr rates. The maximum percent difference from the average is 1.7%, and therefore, there is no significant rate dependence on temperature for these conditions. For the $\Delta T = 300°C$ case, the largest percent difference between the average of the two rates is 1.1%. From the above comparisons, it is clear that rate does not have a strong influence on the temperature of the retort within the furnace regions. This indicates that heat transfer within the furnace and retort is at a steady state condition for all three selected advancement rates given the same initial conditions.

A comparison between the lid and no-lid configurations at 1.8 mm/hr is shown in Figure 4.5. The T1 temperature profiles for both configurations are similar with the lid configuration being slightly warmer throughout the process. The comparison of T3 values reveals there is about a 10°C difference between them indicating that the lid slows

the rate of heat loss from the salt (for example, it acts as a radiation shield). Similar observations are apparent with the other rates.

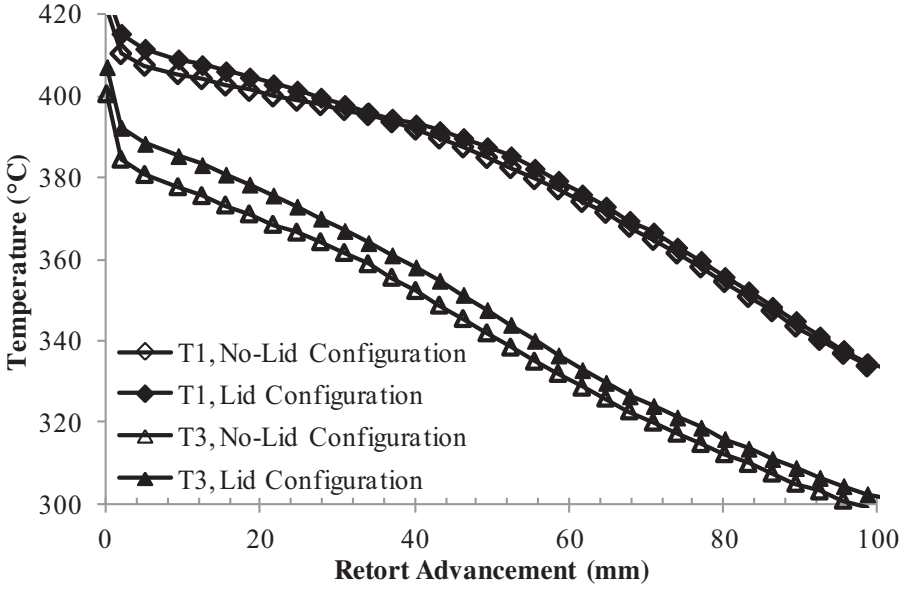

Figure 4.5: Comparison of the 1.8 mm/hr temperature profiles between the lid and no-lid configurations.

A comparison between temperature profiles for the rest of the experimental conditions was not done due to the large variation of the retort advancements, thermocouple positions, reference points, and salt heights. Comparisons between these conditions are better shown later using the concentration profiles.

Based on the temperature profiles, the actual or effective growth rate of the crystals can be estimated. The melting temperature of pure LiCl-KCl eutectic salt is 352°C and since the slope of the liquidus line is not steep, the melting temperature of the mixture has been approximated to be constant with respect to the CsCl concentration. The time at which each thermocouple (T1, T2, T3 and T4) reaches the melting temperature has been recorded. By dividing the distance between thermocouples by the recorded Δt, an approximate growth rate can be calculated. The actual time from the start of solidification to termination of solidification is found by dividing the height of the grown salt ingot by the effective growth rate. Table 4.1 shows the effective growth rates and growing times for the various rates and conditions.

Table 4.1: Effective growth rates and times for the different rates and conditions.

Advancement Rate (mm/hr)	Effective Growth Rate (mm/hr)	Growth Time (hr)
50 g, No-Lid Configuration, ΔT = 200°C		
1.8	1.75	23.43
3.2	2.85	15.09
5.0	4.70	8.94
50 g, Lid Configuration, ΔT = 200°C		
1.8	1.95	23.59
3.2	3.30	13.94
5.0	5.21	8.83
400 g, No-Lid Configuration, ΔT = 200°C		
1.8	2.52	34.52
3.2	4.13	21.07
5.0	6.42	13.55
50 g, No-Lid Configuration, ΔT = 300°C		
1.8	N/A	N/A
3.2	3.08	13.96
5.0	4.82	8.92

The effective growth rates are close to the advancement rates as is expected. Interestingly, under some conditions the effective growth rates are lower than expected and for other conditions they are higher. For example, the growth rates for the lid configuration are 3% to 8% larger than expected and the rates for the no-lid configuration are between 3% and 6% lower. The lid configuration would have a slower growth rate because the lid may act as radiation shield, thus reducing the heat loss from the top surface of the salt. Another interesting point is that the growth rates from the 400 g experiments are 30% to 40% faster than expected. This effect is likely due to the thinner blanket material used which may allow for increased radial cooling.

The magnitude of liquid mixing in the salt can be approximated using the parameter Δ, which is a function of the Gr, Pe and Sc defined by Eqns. 2.31 to 2.33. Parameter Δ is represented by δR/D, and was discussed in Chapter 2. The ΔT in the Gr was calculated using the temperature gradient between the top and bottom of the liquid

salt. The Gr and Sc were then calculated using properties calculated based on an average temperature. The Pe number was calculated using the crucible radius and retort advancement rate. Table 4.2 shows the Gr an Pe numbers as well as the calculated parameter Δ for the different rates and conditions when the top surface of the salt starts to solidify. Sc and D were approximately 3,800 and 6.05×10^{-10} m^2/s for these experiments, respectively. According to Favier [**49**], for $\Delta \geq 5$, the solute mixing is diffusion controlled and for $\Delta \leq 1$, the mixing can be considered well-mixed. Values of Δ between these ranges is in a convection-diffusion regime. Based on Favier's conclusions, the solute mixing for the 1.8 mm/hr, 50 g, lid and no-lid experiments at a ΔT of 200°C are expected to be closer to the well-mixed condition. The remaining experiments are in the convection-diffusion regime.

Table 4.2: Grashof number, Peclet number, Δ, and δ for the salt at the varying conditions.

Advancement Rate (mm/hr)	**Grashof Number × 10^4**	**Peclet Number**	**Parameter Δ**	**δ (mm)**
50 g, No-Lid Configuration, ΔT = 200°C				
1.8	1.36	11.65	1.04	1.30
3.2	1.71	18.97	1.58	1.21
5.0	1.54	31.29	2.70	1.25
50 g, Lid Configuration, ΔT = 200°C				
1.8	1.94	12.53	1.00	1.12
3.2	1.95	21.21	1.69	1.11
5.0	2.28	32.29	2.44	1.02
400 g, No-Lid Configuration, ΔT = 200°C				
1.8	9.32	32.97	1.54	1.33
3.2	14.2	53.09	2.17	1.14
5.0	13.1	84.00	3.52	1.19
50 g, No-Lid Configuration, ΔT = 300°C				
1.8	N/A	N/A	N/A	N/A
3.2	2.82	20.50	1.47	1.04
5.0	2.95	32.08	2.28	1.03

4.4 Concentration Profiles and Effects

The elemental composition of collected samples from each experiment were measured via ICP-MS. Results are in units of micrograms (μg) of the given element to liters (L) of acid solution. The raw ICP-MS data were converted into local compositions

using a mole balance. With this method, the number of moles of Cs, for example, was set equal to the number of moles of Cl in each sample. The amount of Cs was added to the calculated amount of Cl to calculate amount in g of the CsCl in the solution. The same was done for the Li and K to calculate the amounts of LiCl and KCl. Assuming one liter of solution, the mass fraction (ω) of each sample was calculated by:

$$\omega_{CsCl} = \frac{m_{CsCl}}{m_{CsCl} + m_{LiCl} + m_{KCl}} \qquad \text{Eqn. 4.5}$$

where m is the mass of each component. Uncertainty for each sample was calculated with the largest source of uncertainty was from the mixed standards and calibration curve used during ICP-MS measurements. In this case, uncertainty ranged from 5% to 10% of the measured value. Locations of each sample were measured down the axis of the salt and non-dimensionalized using the total salt height. Errors for both the composition and location of the sample were propagated using standard error propagation formulas. Figures containing all of the local composition data are shown in Appendix D.

4.4.1.1 Buildup Fraction

In zone freezing, it is important to know at which point the grown crystal should be cut to obtain the desired salt purity. To do this, the salt crystal was separated into several hypothetical regions as shown in Figure 4.6(a). The total mass of salt for each region was estimated based on the average crystal geometry and the density of the salt. The mass of CsCl per section was approximated by assuming that the local composition in the segment was representative of the entire salt region as shown in Figure 4.6(b). The total composition of the salt down to a given segment was then calculated using a buildup fraction. The buildup fraction is defined below as:

$$\text{Buildup Fraction}_n = \sum_{i=1}^{n} \frac{m_{CsCl_i}}{m_{Salt\,i}} \qquad \text{Eqn. 4.6}$$

where n is the number of segments of interest, the subscript $_{Salt}$ represents all salt components, and i represents the segment number. The buildup fraction is the overall weight fraction of CsCl in the salt from the top of the salt down to the segment of interest.

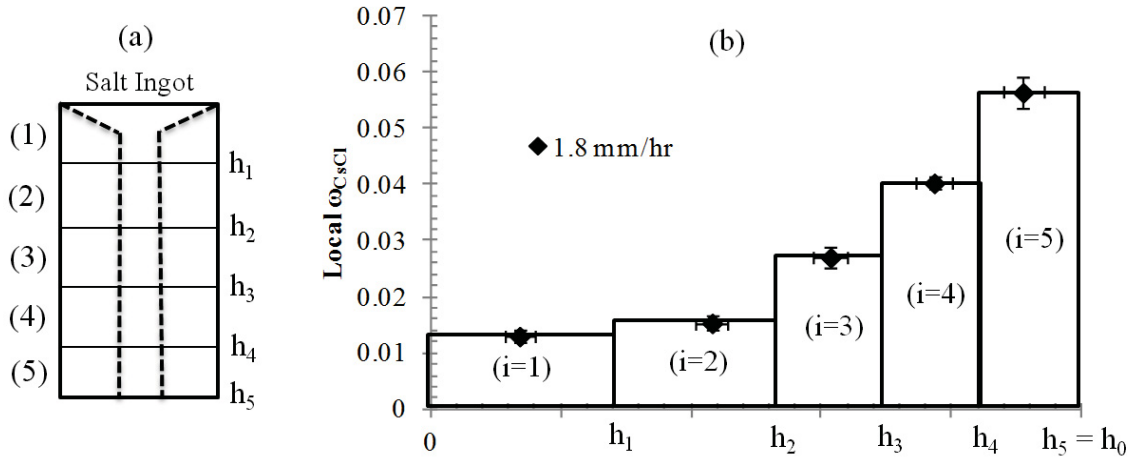

Figure 4.6: (a) Schematic of the segmented salt ingot. (b) Representation of each segment of salt with its approximated composition. Data is from the 3 wt% salt run at 1.8 mm/hr and a ΔT of 300°C.

Table 4.3 shows results of the above analysis for the 3 wt% salt run at 1.8 mm/hr and ΔT of 300°C as an example of the buildup fraction method. The last column in Table 4.3 shows the buildup fraction of the salt. The key advantage to this analysis technique is that it shows the relationship between salt amount and its composition. For instance, if the crystal is cut at h_3, then the top portion, with 70% of the total salt, would have a composition of 2.3 wt% CsCl. If a 2 wt% CsCl composition were desired, then by interpolation, the top 38% of the salt by mass should be recycled.

Table 4.3: Buildup fraction data for the 3 wt% CsCl salt run at 1.8 mm/hr and a ΔT of 300°C.

Segment (i)	**Approximate m_{Salt_i} (g)**	**Approximate m_{CsCl_i} (g)**	**$\sum m_{Salt_i}$ (g)**	**$\sum m_{CsCl_i}$ (g)**	**Buildup Fraction$_n$**
1	12.2	0.23	12.2	0.23	1.89
2	13.1	0.29	25.3	0.52	2.05
3	10.0	0.31	35.3	0.83	2.34
4	6.2	0.25	41.6	1.08	2.59
5	8.5	0.47	50.0	1.55	3.09

For ease of comparison, a desired salt purity of 2 wt% CsCl has been assumed and will be used throughout. It should be note that the buildup fraction analysis can be done at whatever salt purity is required for the application. However, for salt purities below 1.8 wt% CsCl, extrapolation of the data may be required if operating at a rate of 5.0

mm/hr. In addition, this method can be used to determine the composition of the recycled salt if the amount or ratio of salt to be recycled is specified.

Figure 4.7 shows the comparison of the different rates and lid configurations for the 50 g of 3 wt% CsCl salt at a ΔT of 200°C. The no-lid configuration has a large variation between the different rates indicating that the system is rate dependant. Here, separation of CsCl from the salt increases with decreasing rate because a slower growth rate provides conditions closer to equilibrium than the faster growth rates. Interestingly, for all the experiments in the lid configuration cases, the experiments show little rate dependence with data at different rates falling in nearly the same ranges. This observation is not consistent with expectations. It is suspected that the lid changes the heat transfer rates from the salt at the top surface. Without the lid, the hot salt is exposed to the body of the retort which is at a lower temperature and radiation heat loss approximately 2 watts (W). With the lid in place, combined heat transfer between the surface of the salt and the lid is approximately 0.05 W. As a result, the cooling at the surface of the salt is reduced and the crystal growth rate for the lid configuration may be different than that of the no-lid configuration.

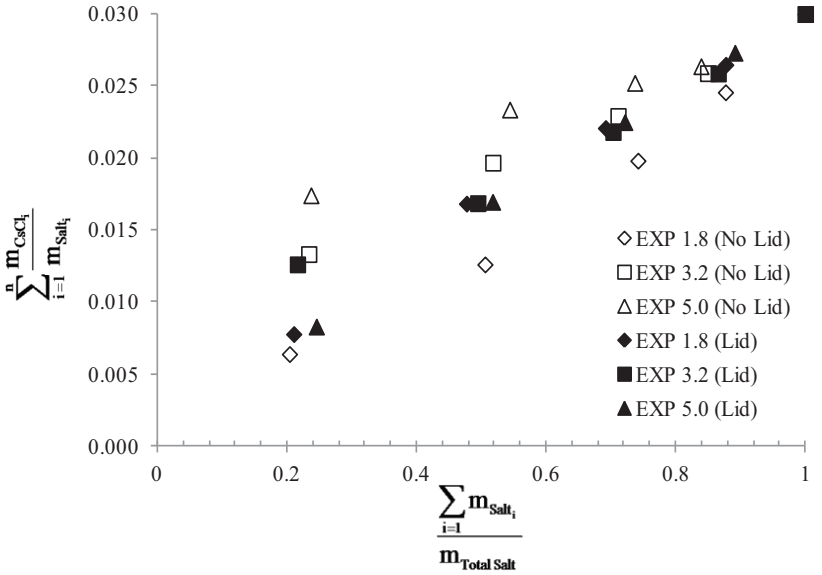

Figure 4.7: Comparison between rates and lid configurations for the 3 wt% CsCl, 50 g salt sample operated with a ΔT of 200°C.

The comparison shown in Figure 4.7 between the lid and no-lid configuration indicates that the best configuration depends on the selected rate. For example, if the advancement rate were set at 1.8 mm/hr, then approximately 75% of the salt for the no-lid configuration and 61% of the salt for the lid configuration could be recycled. For this rate, the no-lid configuration is best. However, if a rate of 5.0 mm/hr were selected, approximately 37% of the salt for the no-lid configuration and 63% of the salt for the lid configuration could be recycled. The same trend is observed for the 3.2 mm/hr rate with approximately 54% and 63% of the salt being recycled for the no-lid and lid configurations, respectively. For these rates, the lid configuration is best. Overall, the 1.8 mm/hr rate with a no-lid configuration provides the best separation, allowing for a greater amount of salt to be recycled at any given purity.

A comparison between the 50 g and 400 g experiments at varying rates is shown in Figure 4.8. The difference between the 50 g and 400 g samples at 1.8 mm/hr are significant for the first potion of the salt. However, for the remaining section of the salt the 50 g and 400 g samples are nearly identical. The 1.8 mm/hr rate for both the 50 g and 400 g experiments yield the largest amount of recycled salt at approximately 75% and 78%, respectively. A comparison between the 3.2 mm/hr rates shows that the 50 g

experiments yield a higher purity crystal in general. However, at 2 wt% CsCl, the approximate salt recycle is 55% of the salt for both the 50 and 400 g cases. At the 5.0 mm/hr rate, approximately 37% and 55% of the salt can be recycled for the different salt amounts, respectively. Overall, the 400 g samples have better separation tendencies than the 50 g samples.

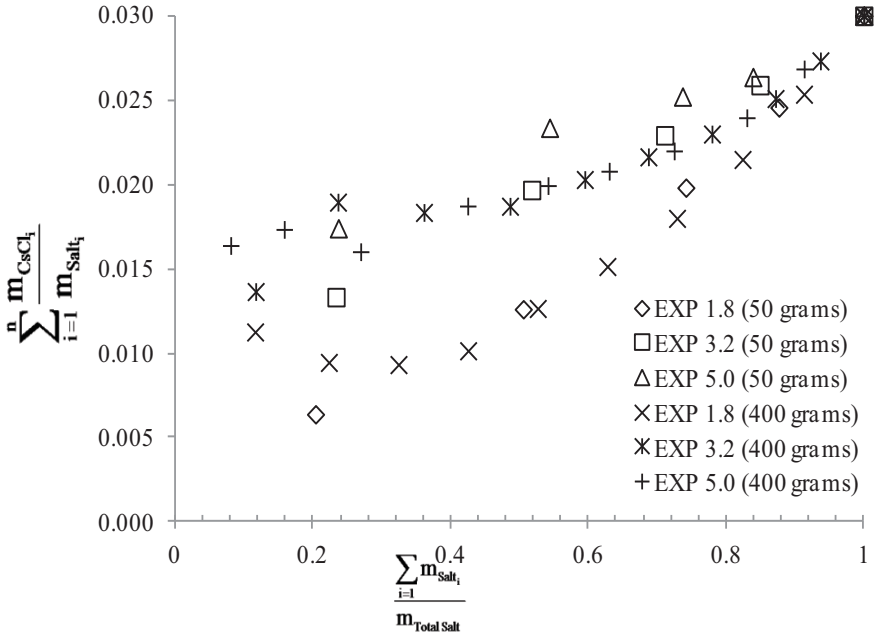

Figure 4.8: Comparison between rates and the 50 g and 400 g cases for the 3 wt% CsCl salt operated with a ΔT of 200°C.

A comparison between the different rates and operating temperatures is shown in Figure 4.9. For the ΔT of 300°C case, the variation between rates is much less than for the ΔT of 200°C case, which indicates that separation is less dependent on rates under these conditions. At the rate of 1.8 mm/hr, approximately 75% and 71% of the salt can be recycled for the ΔT of 200°C and 300°C cases, respectively. At the 3.2 mm/hr rate the ΔT of 200°C case is best in general; however, at 2 wt% both cases have similar recycle ratios of approximately 54% and 48%, respectively. At 5 mm/hr, the ΔT of 300°C case is significantly better with 50% of the salt being recycled verses 37% for the 200° case. Overall, the ΔT of 200°C provides the best separation.

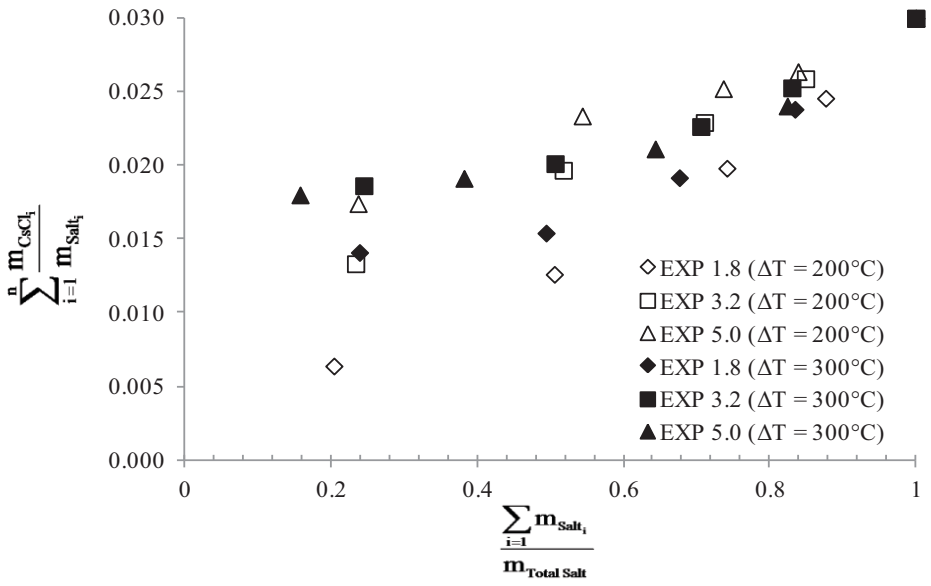

Figure 4.9: Comparison between rates and the operating temperatures of ΔT = 200°C and ΔT = 300°C. 50 g samples initially at 3 wt% CsCl were used.

A summary of results for the 3 wt% CsCl experiments, under 2 wt% desired purity, is shown in Table 4.4. Here, the percent of the salt recycled is used to calculate the amount of salt in g recycled per experiment. The throughput of both the recycled and waste streams is calculated using the total growth time of each experiment. Waste stream compositions (wt% CsCl) have also been calculated. A similar table to the one shown below can be compiled using a different value for the desired salt purity using the buildup fraction plots above.

Table 4.4: Summary of result for the 3 wt% CsCl experiments.

Rate (mm/hr)	Salt Recycled (%) (2wt% CsCl)	Amount Recycled (g)	Growth Time (hr)	Recycled Throughput (g/hr)	Waste Throughput (g/hr)	Waste Composition (wt% CsCl)
50 g, No-Lid Configuration, ΔT = 200°C						
1.8	75%	37.5	23.43	1.60	0.53	6.00%
3.2	54%	27.0	15.09	1.79	1.52	4.17%
5.0	37%	18.5	8.94	2.07	3.52	3.59%
50 g, Lid Configuration, ΔT = 200°C						
1.8	61%	30.5	23.59	1.29	0.83	4.56%
3.2	63%	31.5	13.94	2.26	1.33	4.70%
5.0	63%	31.5	8.83	3.57	2.10	4.70%
400 g, No-Lid Configuration, ΔT = 200°C						

1.8	78%	312.0	34.52	9.04	2.55	6.55%
3.2	55%	220.0	21.07	10.44	8.54	4.22%
5.0	55%	220.0	13.55	16.24	13.28	4.22%
50 g, No-Lid Configuration, ΔT = 300°C						
1.8	71%	35.5	23.50	1.51	0.62	5.45%
3.2	48%	24.0	13.96	1.72	1.86	3.92%
5.0	50%	25.0	8.92	2.80	2.80	4.00%

To compare between the 1 wt%, 3 wt%, and 5 wt% CsCl salt experiments, a cumulative method was used. With this method, the amount of CsCl in each segment of salt was accumulated ($\sum m_{CsCl_i}$), and divided by the total amount of CsCl in the salt. It is convenient to calculate the cumulative mass fraction having already calculated the buildup fraction. Cumulative mass fractions for the three initial compositions are shown in Figure 4.10 for the 5 mm/hr advancement rate. The difference between the initial composition is relatively small and no particular pattern is observed from the data. From these results, it is concluded that the initial composition of the salt, at least in this concentration range, does not strongly influence the separation; therefore, it is assumed that the above conclusion is applicable to other rates and conditions within the salt. Since the majority of the experiments were conducted at 3 wt% CsCl, the above assumption provides a method to predict the concentration profiles of salts with different initial compositions for the respective configurations and rates.

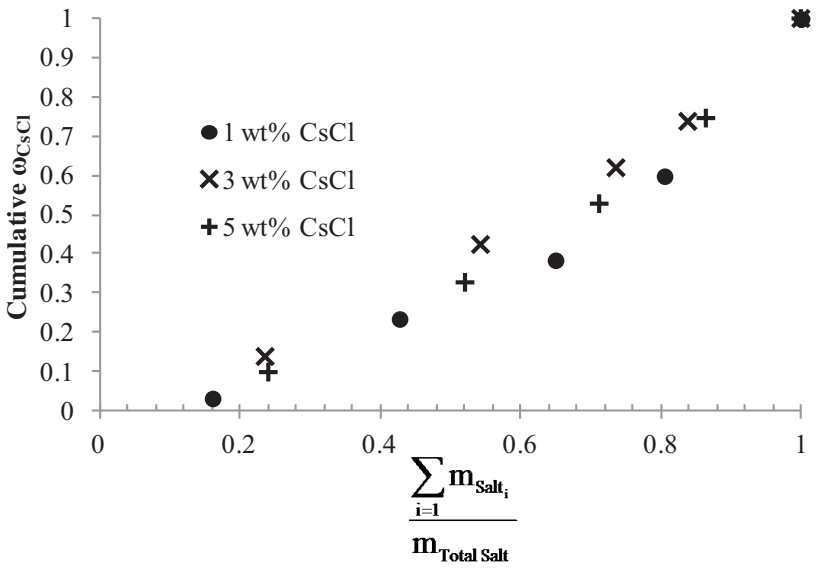

Figure 4.10: Comparison between 50 g experiments operated with an initial compositions of 1 wt%, 3 wt%, and 5 wt% CsCl at a rate of 5 mm/hr with a ΔT of 200°C and a no-lid configuration.

The concentration profiles at different initial compositions were predicted by working backwards from the assumed cumulative profile. For example, it was desired to predict the profile of an experiment using an initial composition of 5 wt% CsCl rather than 3 wt% CsCl, and the 3 wt% CsCl experiment conducted at 5.0 mm/hr with a no-lid configuration was be used. For this experiment, the total amount of CsCl was 1.5 g. To predict the new profile, the new amount of CsCl (2.5 g for a 5 wt% case) is multiplied by the cumulative value "i," to calculate the $\sum m_{CsCl_i}$ for each segment. The buildup fraction is then calculated by dividing the calculated $\sum m_{CsCl_i}$ by the $\sum m_{Salt_i}$. The buildup fraction for the predicted 5 wt% CsCl case and the measured 3 wt% CsCl case is shown in Figure 4.11. Notice that as the initial composition increases, the amount of salt that can be recycled at a desired purity decreases. This indicates that there is a diminishing return. The capability of predicting the buildup fraction is especially useful for process optimization and for predicting the results of multiple zone freezing stages as will be discussed later.

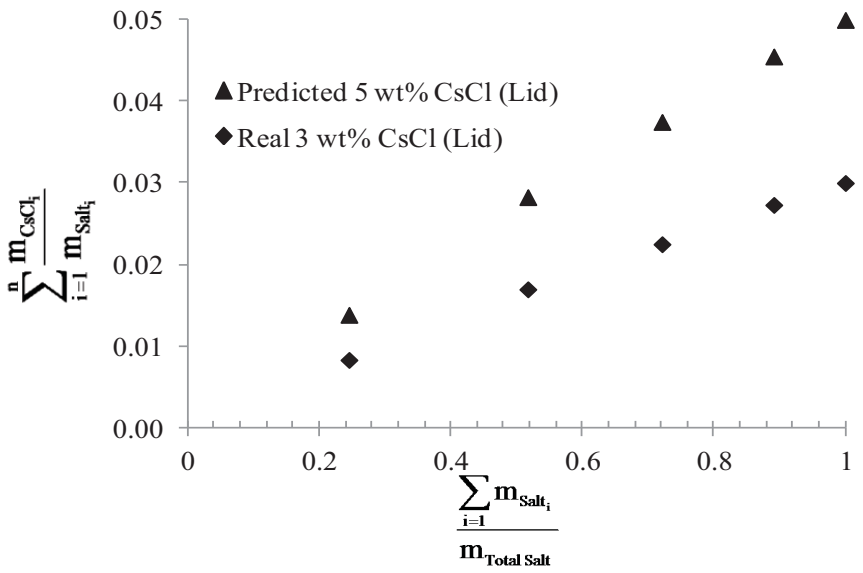

Figure 4.11: Predicted buildup fraction of a 5 wt% CsCl salt operated at 5 mm/hr with a lid configuration.

4.5 $CeCl_3$ Results

Only one experiment was conducted using $CeCl_3$. Results of this experiment are shown in Figure 4.12. Figure 4.13 shows the buildup fraction for the $CeCl_3$ experiment. $CeCl_3$ separates easily from the LiCl-KCl salt allowing for a very pure recycled crystal. For example, at a purity of 0.5 wt% $CeCl_3$, approximately 85% of the salt can be recycled.

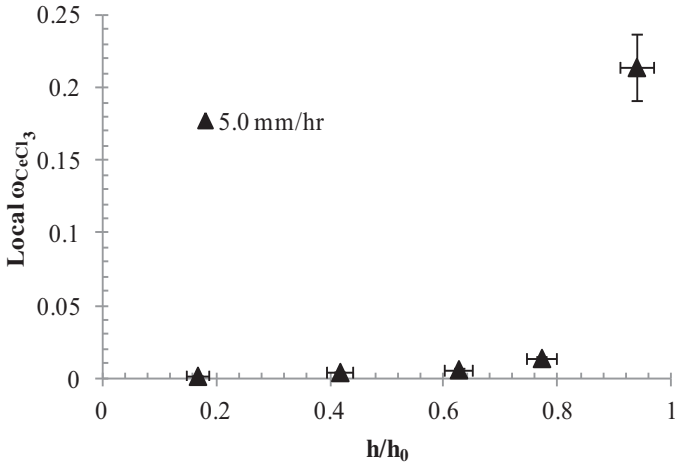

Figure 4.12: Local compositions of the 3 wt% $CeCl_3$ experiment operated at 5 mm/hr. The HTZ was set at 425°C and the LTZ was set to 275°C for this experiment. 50 g of salt was used.

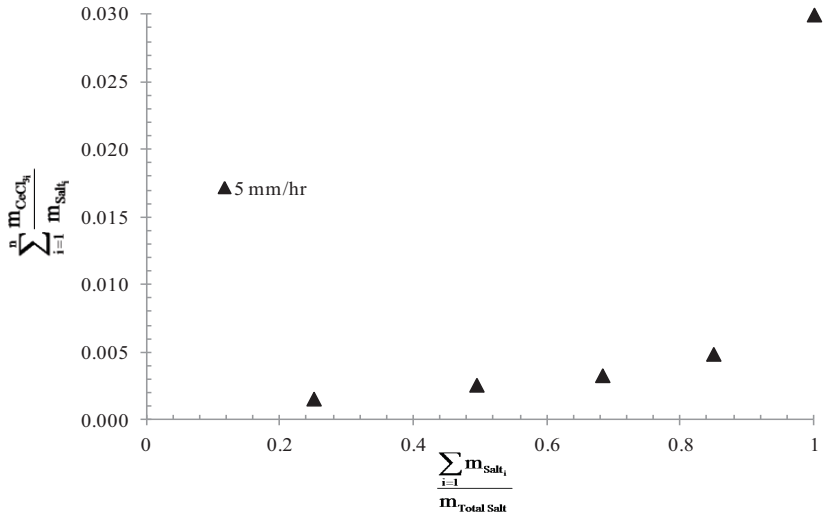

Figure 4.13: Buildup fraction for the 3wt% $CeCl_3$ experiment.

4.6 Ideal Operating Conditions

In this section, the ideal rate and configuration was determined. The idea is to provide conditions that would yield the largest amount of clean salt per time (g/hr) and achieve a given purity and percentage of recycled salt. Specifically, the effects of multiple zone freezing stages are considered at the different rates and conditions. Many variations can be explored, such as multiple stages using different rates and conditions for each stage. However, for simplicity, each zone freezing train is operated under the same rate and conditions. Using this method the ideal rate, conditions, and number of stages can be identified. Other areas, such as economics, can be used for optimization; however, they are not explored in this work.

As shown by the results summarized in Table 4.4, the 1.8 mm/hr rates (on an average) have the greatest amount of salt recycled with the highest concentration of CsCl in the waste stream. The (3.2 and 5.0) mm/hr growth rates have a smaller percentage of recycled salt per run or stage, but they have a higher mass flow rate of recycled salt. By using multiple recycle stages, or in other words, processing the waste from one stage in a subsequent stage (see Figure 4.14), the faster growth rates may provide a sufficient percentage of clean salt at a faster rate.

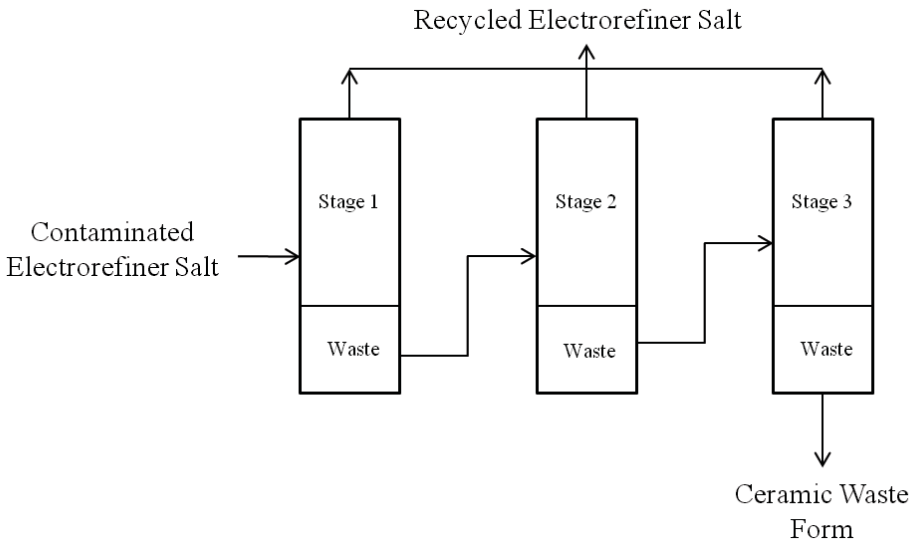

Figure 4.14: Schematic illustrating multiple zone freezing stages.

Table 4.5 shows the results of adding multiple stages for each experimental condition. The first stage is the same as reported experiments; however, since the waste composition is greater for the second stage, predicted values are used. For example, the 5.0 mm/hr rate with a no-lid configuration has a 37%, 17%, and 5% recycle for the first, second and third stages, respectively. Here, the third stage adds little and an additional stage would not be feasible. The recommended rate for the no-lid configuration depends on the required percentage of salt to be recycled. If 50% of the salt is to be recycled, then a single stage process operated at 3.2 mm/hr has the highest recycle flow rate of 1.79 g/hr. If 70% is required, then a single stage, 1.8 mm/hr process is recommended. For a recycle of greater than 80% of the salt, a two stage, 1.8 mm/hr process is needed.

Table 4.5: Summary of results for multi-stage separation.

Rate (mm/hr)	Stage	Processed (g)	Time (hr)	Recycled (g)	Waste (g)	Waste Composition (wt%)	% Recycled per Stage	Total % Recycled	Recycled Flow (g/hr)
50 g, No-Lid Configuration, ΔT = 200°C									
1.8	1	100.0	46.9	75.0	25.0	6.0%	75%	75%	1.60
	2	25.0	11.7	14.0	11.0	10.0%	56%	89%	1.52
3.2	1	100.0	30.2	54.0	46.0	4.2%	54%	54%	1.79
	2	46.0	13.9	14.0	32.1	5.1%	30%	68%	1.54
	3	32.1	9.7	5.6	26.5	5.7%	17%	74%	1.37
5.0	1	100.0	17.9	37.0	63.0	3.6%	37%	37%	2.07
	2	63.0	11.3	10.8	52.2	3.9%	17%	48%	1.64
	3	52.2	9.3	2.8	49.4	4.0%	5%	51%	1.31
50 g, Lid Configuration, ΔT = 200°C									
5.0	1	100.0	17.7	63.0	37.0	4.7%	63%	63%	3.57
	2	37.0	6.5	13.7	23.3	6.2%	37%	77%	3.17
	3	23.3	4.1	6.1	17.2	7.6%	26%	83%	2.93
	4	17.2	3.0	3.5	13.7	9.0%	20%	86%	2.75
50 g, No-Lid Configuration, ΔT = 300°C									
1.8	1	100.0	46.9	71.0	29.0	5.4%	71%	71%	1.51
3.2	1	100.0	30.2	48.0	52.0	3.9%	48%	48%	1.59
5.0	1	100.0	17.8	50.0	50.0	3.7%	50%	50%	2.81
	2	50.0	8.9	4.2	45.8	3.8%	8%	54%	2.03
	3	45.8	8.2	4.3	41.6	3.9%	9%	58%	1.68

For the lid configuration, the concentration profiles in all three rates were the same so the 5.0 mm/hr rate was selected due to quick growth times. The most attractive feature of this configuration and rate is the high recycle flow rate (3.57 g/hr for first stage) with a high percentage of recycled salt (63% for first stage). In this case, four stages can be effectively used to achieve a higher percentage of recycled salt. By the end of the fourth stage, 86% of the salt can be recycled with a mass flow rate of 2.75 g/hr. For the ΔT of 300°C cases, it is only feasible to use multiple stages at 5.0 mm/hr, and then, the effectiveness of the second and third stages is low. If 50% recycled is required then a single stage, 5.0 mm/hr process is ideal. If greater than 60% of the salt is to be recycled, then the 1.8 mm/hr is needed.

The 400 g cases are not shown in Table 4.5 because the scale is different and a direct comparison with other conditions has not been attempted here. However, the recommended conditions for the 50 g experiments are applied to the 400 g cases since their differences in the explored ranges are small. A comparison between the ideal rates within the experimental conditions and stages shows that the 5.0 mm/hr rate with a lid configuration is the overall best for high throughput and percentage of salt recycled per time. The number of stages used depends on the required percentage of salt required for recycle. It is anticipated that using a lid configuration on the 400 g cases would yield similar results.

Chapter 5 Modeling Results and Discussions

5.1 Effects of Modeling Parameters

Several key parameters are used to describe the concentration profile in the solid phase, which are k, R, D, and δ. In this section, the effect of these parameters will be explored using the non-mixed, well-mixed, and Favier models. In the non-mixed model, parameters k, R and D are used. To see the effect of k, parameters R and D were set at 1.8 mm/hr and 6.0×10^{-10} m^2/s, respectively, while k was varied. The effect of k on the non-mixed model is shown in Figure 5.1. As k increases, the initial slope of the concentration curve increases and the steady state condition is reached rapidly. Also, the concentration of the solute at the onset of solidification increases with increasing k. As a result of the above observations, and if only k is considered, then a smaller k corresponds to a lower solute concentration in the solid.

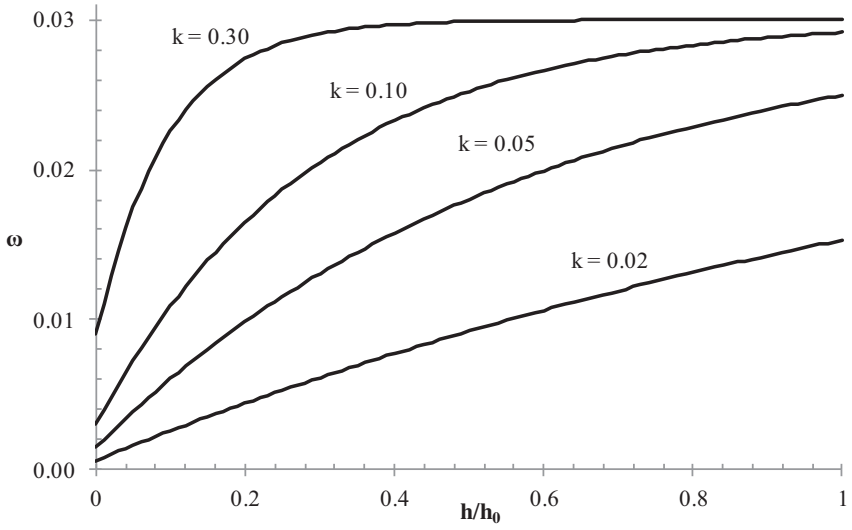

Figure 5.1: Effect of varying k in the non-mixed model. R = 1.8 mm/hr and D = 6.0×10^{-10} m^2/s.

Figure 5.2 shows the effect of varying R and D in the non-mixed model. In the non-mixed model, R and D appear as a ratio (R/D). For ease of comparison, the ratio R/D is varied within the ranges 400 to 2,800 with k set at 0.05. It is observed that as the ratio R/D increases, the slope of the concentration curve increases and the steady state conditions are reached faster. As the ratio of R/D decreases, a lower concentration of

solute in the solid is obtainable. This implies that as R decreases, it will result in a cleaner salt. Likewise, as D increases, better separation will occur.

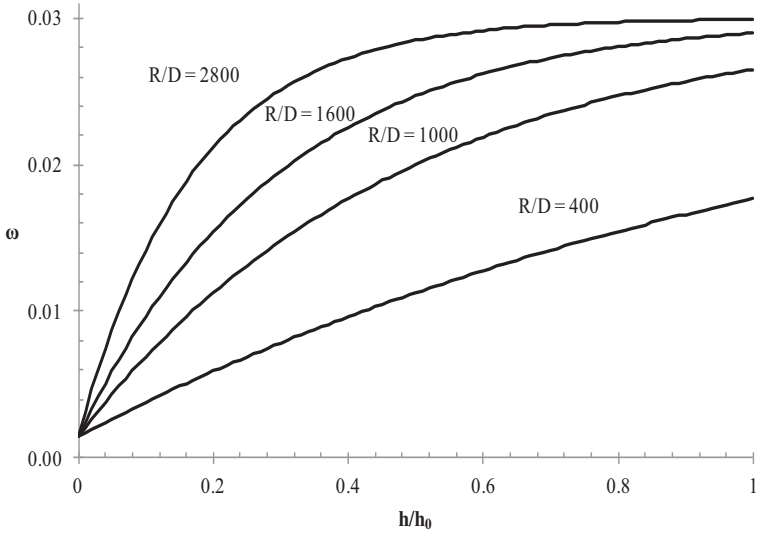

Figure 5.2: Effect of varying R and D in the non-mixed model. k was kept constant at 0.05.

In the well-mixed model there is only one parameter k_{eff}. However, k_{eff} is a function of k and Δ (Eqn. 2.17). Figure 5.3 shows the effect of varying k while Δ was kept constant at a value of unity. In this case, k_{eff} was changed from 0.02, 0.1, 0.3, 0.6, 0.8, and 1.0 and the k for each was calculated to be 0.03, 0.14, 0.32, 0.50, 0.56, and 0.61, respectively. As k increases, the amount of solute in the solid phase also increases. Therefore, a smaller value of k corresponds to better separation and a purer solid product.

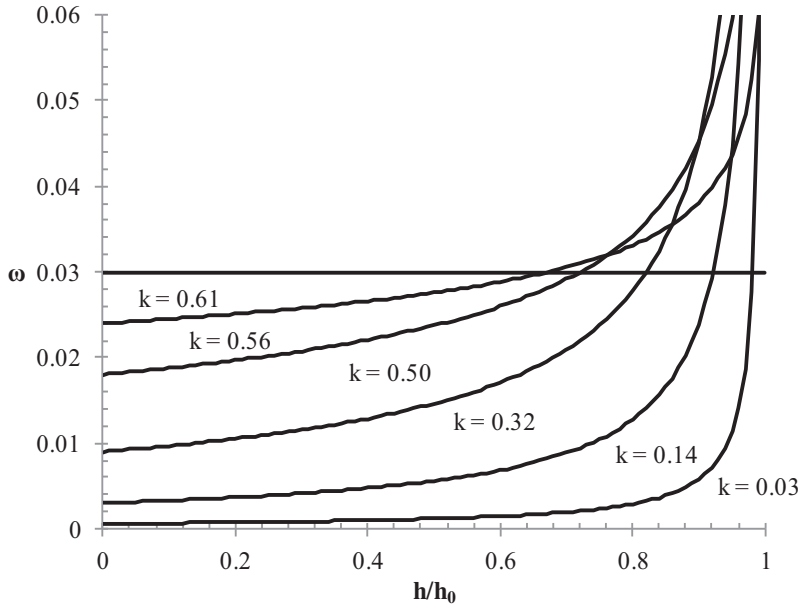

Figure 5.3: Effect of varying k in the well-mixed model. Δ was set constant at unity.

Figure 5.4 shows the effect of varying Δ in the well-mixed model with k = 0.1. Interestingly, as the value of Δ increases, the solute concentration in the solid appears to be reduced. This seems to be in contrast with the idea that a greater order of mixing in the liquid provides better separation (smaller Δ means more mixing). An explanation comes from looking at the k_{eff} values for this system. For example, the values of Δ have been varied from 0.1, 0.5, 1, and 5 and the corresponding k_{eff} values were 0.51, 0.20, 0.14, and 0.09, respectively. The reason separation appears to be better with less mixing is because in order to maintain a value of k = 0.1 for all four cases, the k_{eff} must decreases. When k_{eff} is forced constant at 0.4, then the corresponding k values for the varied Δ's are 0.38, 0.29, 0.20, and 0.004, respectively. The ratio of k_{eff} to k, is the ratio of the concentration of the liquid at interface to the bulk concentration. Here, C_L/C_B is 1.1, 1.4, 2.0, and 90 for the values of Δ above, respectively. The effect of Δ is that as it increases, the mixing effect is reduced significantly as indicated by the large concentration of solute at the interface verses the bulk. Since $\Delta = R\delta/D$, as D increases the parameter Δ must decrease and as R or δ increase, Δ must increase. This is consistent with the above observations.

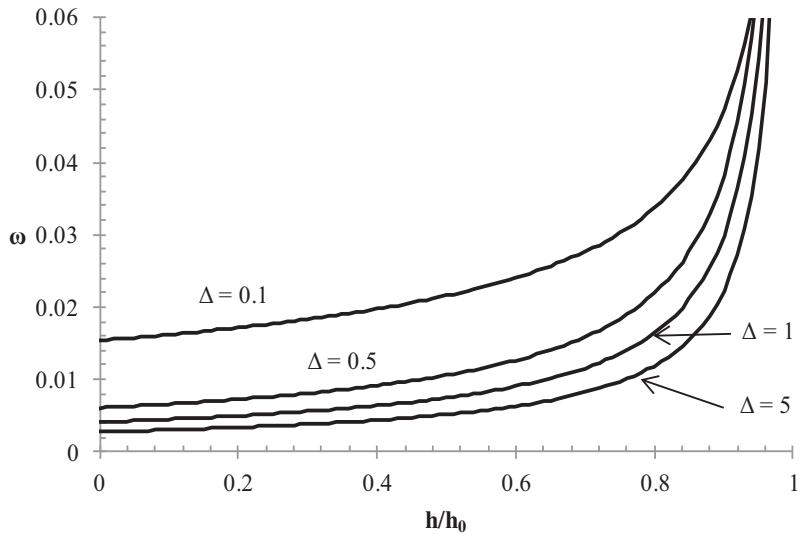

Figure 5.4: Effect of varying Δ in the well-mixed model. k was set constant at 0.1.

As in the well-mixed model, the main parameters in the Favier model are k and Δ. The interplay between these parameters here are the same as above because both models are based on the definition of k_{eff}. However, Figure 5.5 shows a graphical representation of the effect of k in the Favier model with Δ equal to 2.3. Again, as k increases the order of solute rejection decreases. Figure 5.6 shows the effect of varying Δ with k equal to 0.1. In this case, for values of Δ close to one, the concentration curve resembles the well-mixed model. As Δ increases to a value of five, the concentration curve transitions to a non-mixed type profile.

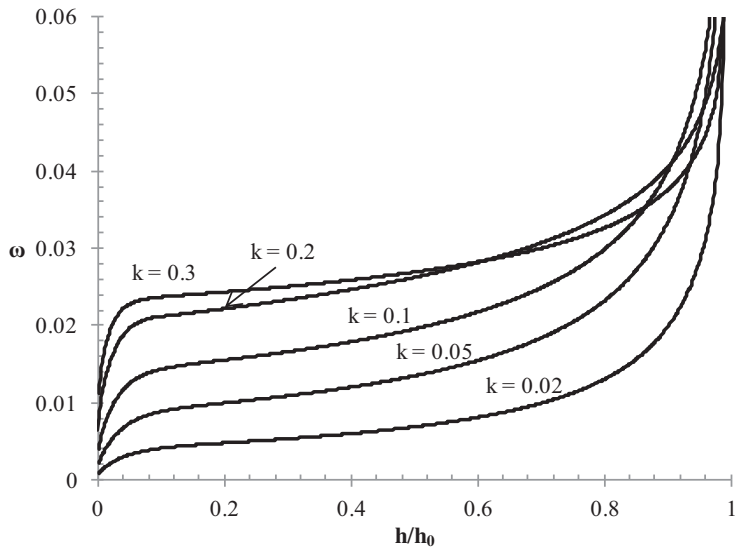

Figure 5.5: Effect of varying k in the Favier model. Δ was kept constant at 2.3.

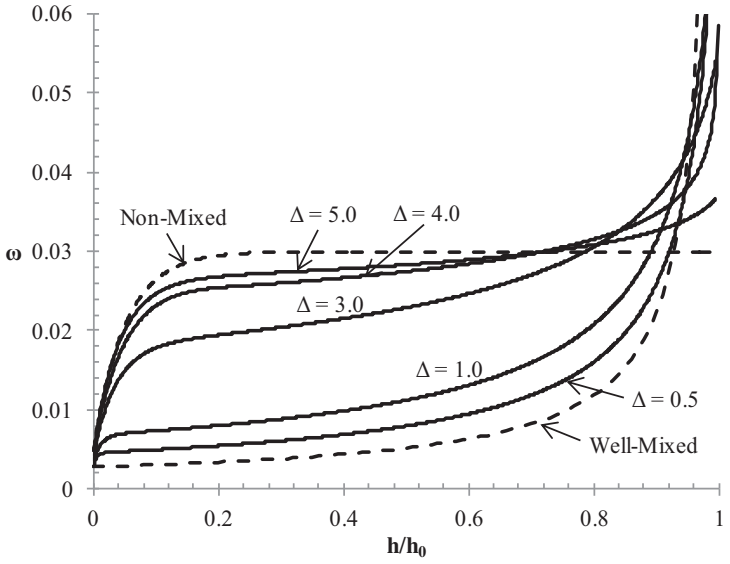

Figure 5.6: Effect of varying Δ in the Favier model. k was kept constant at 0.1.

In general, as k increases, the solute concentration in the solid also increases. Also, as the transport parameter Δ is increased the mixing becomes more diffusion dominant and increased solute concentration in the solid results. There is an interplay between k and Δ at the interface as discussed above. The parameter Δ, describes the transport conditions within the liquid phase. k is a measure of the thermodynamics and kinetics at the interface. From the equilibrium phase diagram, separation at the interface

is a function of the solute concentration. Therefore, k then is not only a function of R, D, and δ, but it is a function of the composition as well.

5.2 Model Fitting

Regression techniques were used to fit the non-mixed, well-mixed, and Favier models to the data by adjusting k and k_{eff}. The k and k_{eff} values for the non-mixed and well-mixed models, respectively, were found using the solver function in Excel by setting the R^2 value equal to one. The k for the Favier model was found by minimizing the error using a least squares (lsqnonlin) function in MATLAB. In the case of the non-mixed model, only the data points close to and below the initial composition were used. This is because the assumption is made in the non-mixed model that once the initial composition is reached, the system is at a steady state and end effects are outside the range of the model. The fitted k_{eff} and k parameters are shown in Table 5.1 for the different experimental conditions. The well-mixed model uses k_{eff} which is in terms of the bulk liquid composition. Using Eqn. 2.17 and the measured Δ, k can be calculated from k_{eff}.

Table 5.1: Fit segregation coefficients for the different models and experimental conditions.

Growth Rate (mm/hr)	Parameter Δ	Non-Mixed (k)	Well-Mixed (k_{eff})	Well-Mixed (k)	Favier (k)
50 g, No-Lid Configuration, ΔT = 200°C					
1.8	1.04	0.093	0.403	0.192	0.226
2.9	1.58	0.065	0.540	0.194	0.175
4.7	2.70	0.056	0.559	0.079	0.100
50 g, Lid Configuration, ΔT = 200°C					
2.0	1.00	0.063	0.673	0.431	0.425
3.3	1.69	0.063	0.553	0.186	0.228
5.2	2.44	0.034	0.703	0.170	0.166
400 g, No-Lid Configuration, ΔT = 200°C					
2.5	1.54	0.030	0.475	0.162	0.156
4.1	2.17	0.030	0.539	0.118	0.122
6.4	3.52	0.024	0.549	0.035	0.039
50 g, No-Lid Configuration, ΔT = 300°C					
1.8	1.00	0.068	0.475	0.249	0.284
3.1	1.47	0.078	0.563	0.228	0.253
4.8	2.28	0.043	0.504	0.095	0.114

Figure 5.7 shows the best fit for the three models with the experimental data for the 1.8 mm/hr rate conducted using a no-lid configuration and a ΔT of 200°C. Here, the non-mixed model has the worst fit with an R^2 value of 0.64 for the first three points. Based on the value of Δ = 1.04, the transport regime is expected to be convective; and therefore, it makes sense that the non-mixed model fits poorly. The well-mixed model and the Favier model have similar trends with R^2 values of 0.88 and 0.82, respectively. The only key difference between the well-mixed and Favier models occurs up to 5% of the salt solidified. Here, the Favier model increases rapidly from the initial position at $k \cdot C_0$ to the well-mixed position at the location of τ*. In a convective regime, it is expected that the well-mixed and Favier models would match the data; however, the basic trend or slope of both models differ from the measured data.

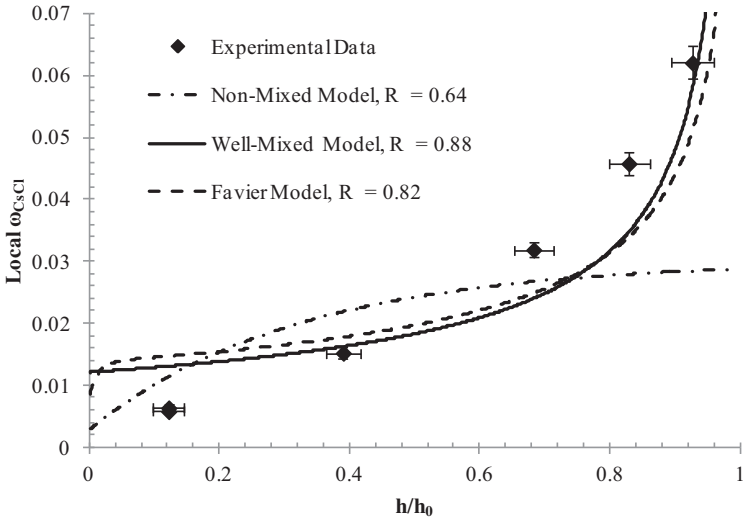

Figure 5.7: Comparison of the experimental data (1.8 mm/hr, 50 g, No-Lid Configuration, ΔT = 200°C) with the non-mixed, well-mixed and Favier models

For the 3.2 mm/hr rate (see Figure 5.8), the non-mixed model actually fits the first three data points with an R^2 value of 0.95. This is unexpected because according to Δ (1.58), the transport regime should still be convective. The well-mixed and Favier models at 3.2 mm/hr are again similar with R^2 values of 0.92 and 0.81, respectively. At 5.0 mm/hr (see Figure 5.9), the non-mixed model follows the data closely with an R^2 value of 0.92. Trends for the well-mixed and Favier models continue to be similar at the 5.0 mm/hr rate, though at this advancement rate, the non-mixed model is better.

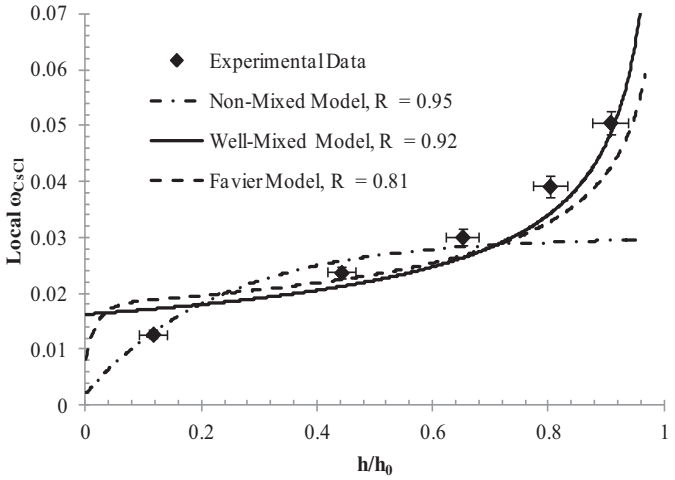

Figure 5.8: Comparison of the experimental data (3.2 mm/hr, 50 g, No-Lid Configuration, $\Delta T = 200°C$) with the non-mixed, well-mixed and Favier models.

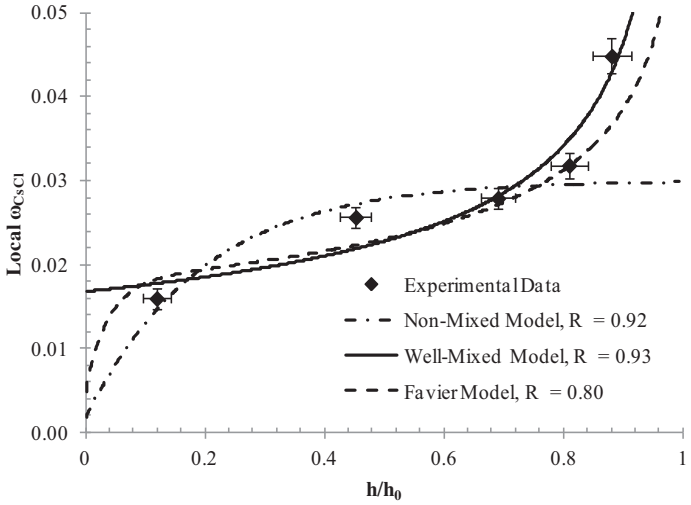

Figure 5.9: Comparison of the experimental data (5.0 mm/hr, 50 g, No-Lid Configuration, $\Delta T = 200°C$) with the non-mixed, well-mixed and Favier models.

For the lid configurations the well-mixed and Favier models fit the experimental data with R^2 values ranging from 0.70 to 0.80. However, again the basic slope of the lines are different from the experimental data as can be seen from Figure 5.10 for the 5.0 mm/hr rate. The non-mixed model fits only slightly better for the first three data points with R^2 values ranging from 0.24 to 0.81. All of the model comparisons with the experimental data are shown in Appendix E.

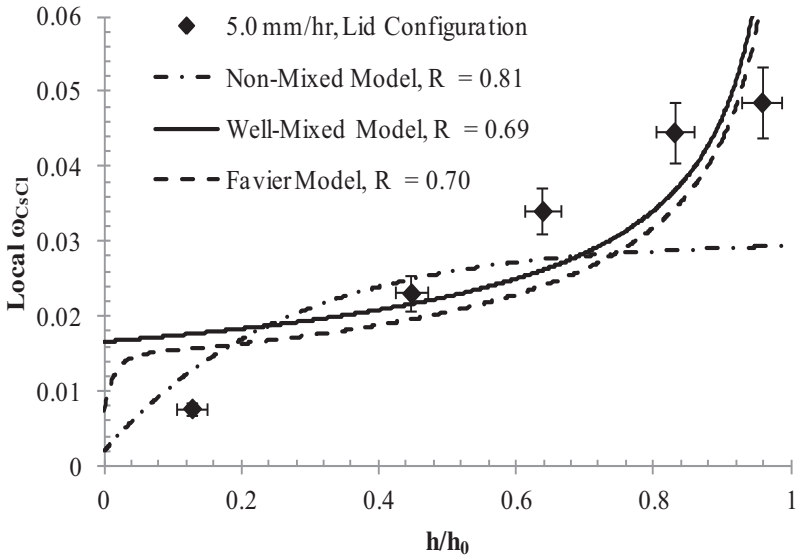

Figure 5.10: Comparison of the experimental data (5.0 mm/hr, 50 g, Lid Configuration, ΔT = 200°C) with the non-mixed, well-mixed and Favier models.

For the 400 g experiments, the well-mixed and Favier models fit the basic trend of the experimental data as shown in Figure 5.11 for the 3.2 mm/hr rate. In this case, the non-mixed model does not fit well with an R^2 of 0.53 for the first 6 data points. The basic trend observed in Figure 5.11 is also observed for the 1.8 mm/hr and 5.0 mm/hr rates at 400 g, as well as all of the ΔT of 300°C cases. From this result, it appears that the 400 g and ΔT of 300°C are primarily well-mixed systems despite the larger values of Δ for the faster rates. With closer observation, it was observed that the Gr number in these experiments are larger than the other experiments performed. This difference in the Gr should be reflected in the parameter Δ; however, values of Δ are nearly the same. It was notes in Chapter 4 that the Sc, D, and r were nearly the same as well. As a result, the dominant term in determining the parameter Δ for these systems is the growth rate. Since the 400 g and ΔT of 300°C cases have a higher Gr number on average it is possible that heat transfer from the liquid to the growing solid is increased. This could have the effect of "warming" the solid-liquid interface, thus slowing the actual growth rate.

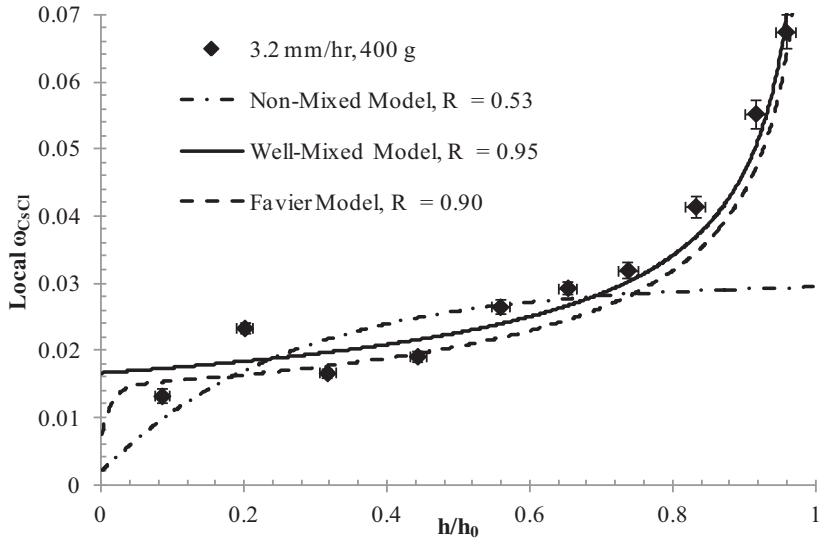

Figure 5.11: Comparison of the experimental data (3.2 mm/hr, 400 g, No-Lid Configuration, ΔT = 200°C) with the non-mixed, well-mixed and Favier models.

The basic trend observed from the 50 g, no-lid and lid configurations at a ΔT of 200°C is that non-mixed model in fits well for approximately the first half of the grown crystal. Therefore, it seems apparent that the experimental transport regime may have been diffusion dominant in this region. If this phase were diffusion dominant, then it stands to reason that the entire sample would be diffusion dominant unless the parameter Δ is decreasing throughout. The diffusion coefficient will remain constant, and δ is only likely to increase throughout the process. For Δ to decrease, R should decrease throughout the process. That is, if the actual growth rate of the salt was fast initially (high Δ), and then slowed down throughout the process (low Δ), then a transformation from a diffusion dominant regime to a convection dominant regime is possible. Liquid mixing as discussed above may contribute to the decreasing growth rate. However, another possible explanation is the amount of solute at the interface is large enough to lower the melting temperature of the mix. As the melting temperature decreases, the amount of heat in the surrounding material must decrease before phase change will occur. This could effectively reduce the growth rate of the solid.

Another reason that the modeling may yield results different from expected is due to the assumption made in the respective models that equilibrium at the interface prevails. If equilibrium at the interface were prevailing, then a near perfect separation would result

since k_0 is equal to zero for this system. This indicates that separation of CsCl from the LiCl-KCl must be due to kinetic effects at the interface. Indeed, it has been shown earlier that k is a function of the rate and composition. As a result, it is very possible that k is not constant throughout the growing period.

5.3 A Hybrid Model

The general trend for the 50 g, no-lid and lid configuration data is that in the first portion of the crystal the non-mixed model fits best, and for the ending portion the well-mixed model fits best. As a result of these observations, it seems logical to combine the non-mixed and well-mixed models to form a hybrid model. Since the Favier model and the well-mixed model are in most cases nearly identical, it is recommended that the well-mixed model be used. For simplicity, a simple weighted average method will be used to combine the non-mixed and well-mixed models together as shown below:

$$C_{Hybrid} = C_{Non-Mixed}\left(1 - \frac{h}{h_0}\right) + C_{Well-Mixed}\left(\frac{h}{h_0}\right) \qquad \text{Eqn. 5.1}$$

where $C_{Non\text{-}Mixed}$ represents the non-mixed model and $C_{Well\text{-}Mixed}$ represents the well-mixed model. The k and k_{eff} parameters listed in Table 5.1 are used.

To understand how each model is contributing on the overall effect of each model, the first and second terms of Eqn. 5.1 were analyzed. By dividing the first and second terms of Eqn. 5.1 by C_{Hybrid}, it is possible to see the exact amount that each equation contributed to the whole solution. For example, for the 1.8 mm/hr rate of a lid configuration, the individual terms on the RHS of Eqn. 5.1 were calculated and then divided by the sum of the two. The results are shown in Figure 5.12. The plot shows that initially all of the hybrid solution stems from the non-mixed solution, and conversely near the end. This observation is expected due to the applied weighting factor. It should be noted that the curves for the non-mixed and well-mixed terms are a mirror image of each other. The figure and trends shown below are typical of all other experimental data sets.

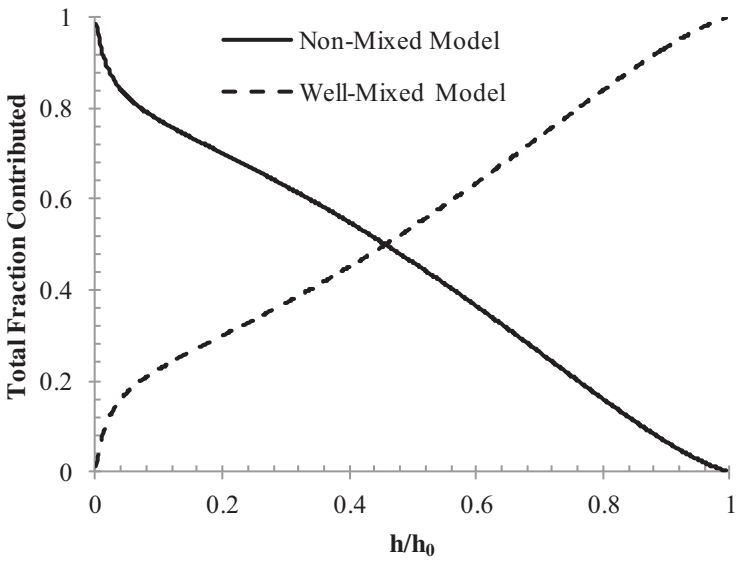

Figure 5.12: The total fraction contributed by the non-mixed and well mixed models to the hybrid solution.

Of more interest is the dynamics of each model's contribution. This can be found by calculating each term in Eqn. 5.1 for several locations of the interface h/h_0. By summing these terms, the total fraction of each model can be determined. Dividing the individual contribution values by its total fraction results in the distribution at each location, as shown in Figure 5.13. Here, it can be seen that each of the models contributes differently than expected. For example, it would seem that the non-mixed model would have the greatest influence initially. However, from the plot shown in Figure 5.14, it can be seen that its influence is initial small and it gradually increases to a maximum around $h/h_0 = 0.38$ and then decreases. The well-mixed model on the other hand, plays and increasing role throughout with most of its influence being seen near the end of the specimen. The intersection of the two points represents the transition of influence between the two models. In other words, up until about $h/h_0 = 0.65$, the most influential model is the non-mixed; and after 0.65, it is dominated by the well-mixed model. This result is different from what may have been initially concluded by observation. Figure 5.13 is very typical of results for all of the experimental conditions. In fact, the transition points for all experiments were calculated to be at an average of 0.67 ± 0.02.

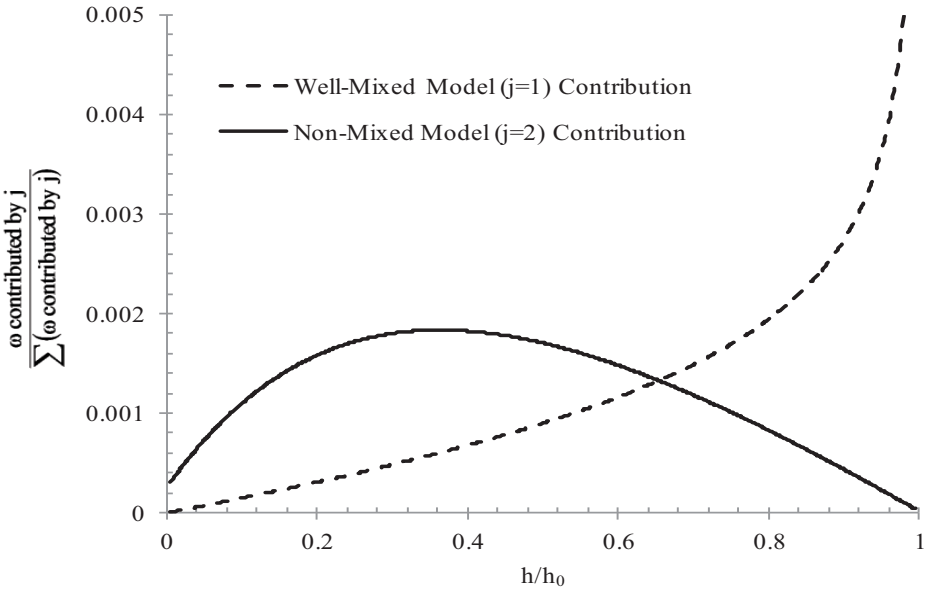

Figure 5.13: The fraction of influence for the non-mixed and well-mixed models.

One advantage to the hybrid model is that the k is effectively increasing throughout. The exact relationship between the effective hybrid k (k_{effH}) and other parameters will not be attempted here. However, conceptually, it can be seen that k_{effH} is basically a function of k and k_{eff} used in the non-mixed and well-mixed models. Another advantage is that this model provides a means for transition between two flow regimes as discussed above. For this to be conceptually true, Δ must be changing. This indicates that k_{effH} will in part be a function of Δ.

Figure 5.14 shows the comparison between the non-mixed, well-mixed, and hybrid model for the experiment conducted at 5 mm/hr, 50 g, no-lid configuration, at ΔT = 200°C. Here, the hybrid model fits best with an R^2 value of 0.96. The hybrid model was applied to all of the experimental data, which is also shown in Appendix E. The hybrid model fits the experimental data better than the non-mixed and well-mixed cases for the 50 g, no-lid and lid configurations. However, for the 400 g and ΔT of 300°C cases the well-mixed model fits better as shown in Figure 5.15. It is interesting to note that the hybrid model still fits ok for the data with the exception of the first three data points. Overall, it appears that the hybrid model can be used to all of the experimental

conditions. However, it fits the data especially well when the flow is in a convection-diffusion regime.

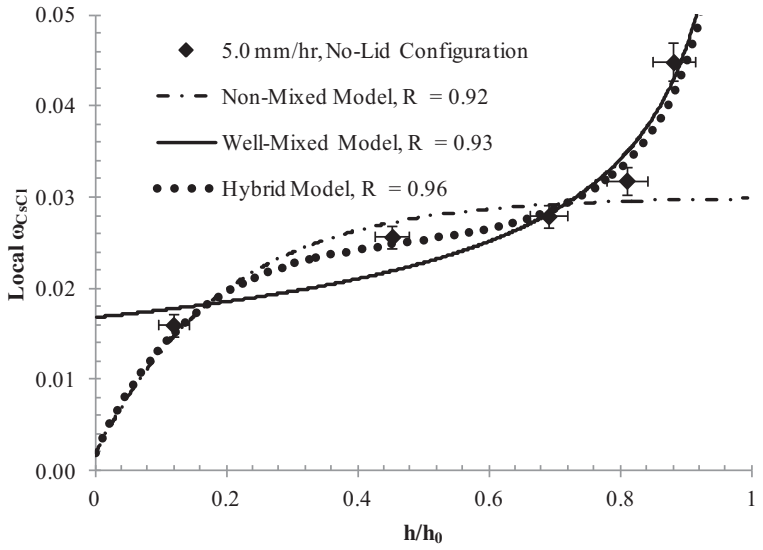

Figure 5.14: Comparison of the non-mixed, well-mixed, Favier, and hybrid models. Experimental conditions were; 5.0 mm/hr, 50 g, no-lid configuration, and a $\Delta T = 200°C$.

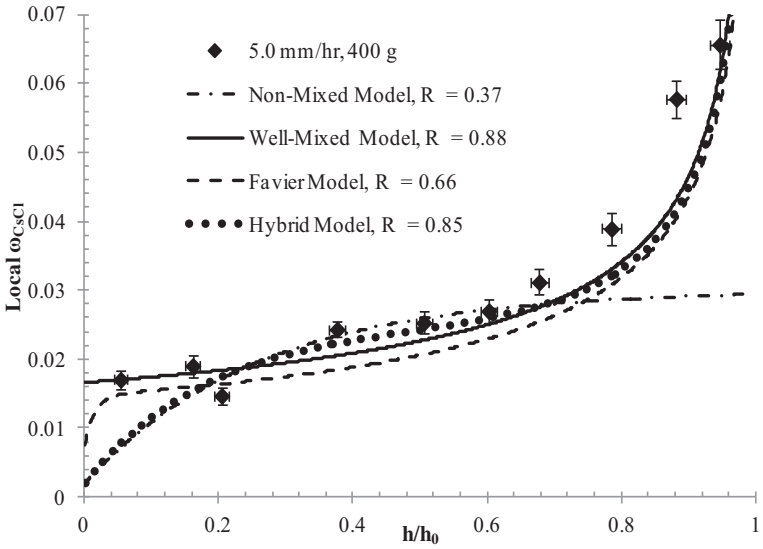

Figure 5.15: Comparison of the non-mixed, well-mixed, Favier, and hybrid models. Experimental conditions were; 5.0 mm/hr, 400 g, no-lid configuration, and a $\Delta T = 200°C$.

Chapter 6 Summary and Recommendations

6.1 Summary

In this work, a zone freezing process has been studied to explore the separation of CsCl from the eutectic LiCl-KCl salt. The purpose of this work was to indentify key parameters and conditions to provide optimal zone freezing performance. This was done by studying the effect of the advancement rate, crucible lid configurations, mixture and crucible size, and the difference between the temperatures of the hot and cold furnace zones.

From the equilibrium phase diagram, a maximum recycle yield of 94% of the electrorefiner salt was calculated—indicating good separation feasibility. Several models were presented to describe the melt crystallization process and specifically, the solute concentration in the liquid phase. The well-mixed model (Eqn. 2.7) assumes that equilibrium conditions at the interface prevail and that no concentration gradients in the liquid phase exist. The effective segregation coefficient k_{eff} is used to describe the solid concentration at the interface. The non-mixed model (Eqn. 2.14) has been developed with the assumption that equilibrium prevails at the interface; however, mixing of the liquid phase is due to diffusion and a concentration buildup at the interface occurs. The segregation coefficient k, is used to model the solid composition. The Favier model was developed to account for convection-diffusion flow regimes using the parameters k and Δ.

Experiments were conducted at (1.8, 3.2 and 5.0) mm/hr for the following parameter variations: (1) lid versus no-lid crucible configurations, (2) 50 g versus 400 g mixture sizes, (3) initial salt compositions of (1, 3, and 5) wt% CsCl and (4) temperature differences between furnace zones of 200°C and 300°C. During experiments, the temperatures were measured at select locations around the salt to provide temperature profiles of the salt with respect to time. Only four thermocouples were used and the actual heat transfer data were not measured in this work. Following the crystal growing experiments, samples were collected and analyzed using elemental analysis.

From the measured temperature profiles the effective growth rate was approximated as well as the growth time. Data collected from elemental analysis and the buildup fraction (Eqn. 4.6) was used to calculate amount of total salt that can be recycled at a given purity. To identify the ideal rates and conditions, a comparison was made using the recycled salt purity, amount of salt, and time. The required salt purity was assumed to be 2 wt% CsCl in this analysis. The ideal conditions were found by maximizing the amount of salt recycled while minimizing the time required. From this, it is recommended that a lid-configuration condition with a ΔT of 200°C be used. Also, the 400 g mixtures show increased performance. It is anticipated that operating the 400 g mixtures with a lid-configuration will yield even better results. Due to time constraints, additional experiments were not conducted but are needed to confirm the above assumption.

The modeling parameters k and Δ were systematically varied within the models to determine their effects on the solute concentration profile. In all the models, as k increased (transport conditions aside) the amount of solute in the solid also increased. As the parameter Δ increased, the magnitude of solute mixing decreases and as a result a larger concentration gradient in the boundary layer adjacent to the solid-liquid interface increases. This increase of solute concentration also causes k to decrease. As a result of these comparisons, conceptually it can be concluded that k is a function of the parameter Δ (R, D, and δ) and the solute concentration and temperatures at the interface.

The non-mixed, well-mixed and Favier models were compared to the experimental data. For the 400 g and $\Delta T = 300°C$ cases the Favier and well-mixed models fit the trend of the experimental data best. In these cases, the Gr was greater, and therefore, these models were expected to fit better. For the 50 g lid and no-lid configurations, the basic trend was that the non-mixed model fit well for the top portion of the crystal and the well-mixed and Favier models fit best for the bottom portion of the crystal. This result may indicate that the transport regime is shifting from a diffusion dominant regime to a convection dominant regime (Δ moves from high to low). For this to occur, the growth rate must also be decreasing. Also, it is apparent that k is not constant throughout the growing period. To account for these observations, a hybrid

model was developed using a weighted average method between the non-mixed, and well-mixed models. In the hybrid model, the parameter Δ is effectively decreasing while k is increasing. The hybrid model fits every experimental case; however, it fits best for the 50 g, lid and no-lid configurations due to the transport transition from non-mixed to well-mixed.

6.2 Recommendations for Future Work

For the experimental part, it is recommended to further explore the separation characteristics of $SrCl_2$ in the LiCl-KCl salt using zone freezing and to determine the CsCl and $SrCl_2$ diffusion coefficients in the molten salt to aid in the modeling an analysis of the data. Additional experiments are necessary to investigate effects of using a lid configuration on separation, specifically the 400 g case and those of radial segregation. Future work should include the studies on higher mass fractions to explore the prospect of operating multiple zone freezing stages and the actual temperatures of the liquid salt during run time to fully understand the growth rate and flow conditions in the salt.

For the modeling aspect, two-dimensional studies of segregation are recommended to explore the effect of radial freezing and segregation as well as axial. Dimensional analysis can be explored to determine a function to describe the effective 'hybrid' k. Future work should focus on the kinetics and thermodynamics of the process to help find the expression for k that can account for these fundamentals.

References

1 Andrews, A. *Nuclear Fuel Reprocessing: U. S. Policy Development*. Congressional Research Service, Order Code RS22542, 2008.

2 Shultis, J. K. and Faw, R. E. *Fundamentals of Nuclear Science and Engineering*. CRC Press, Boca Raton, 2008.

3 U.S. Department of Energy website. http://www.ne.doe.gov/fuelcycle/neFuelCycle.html Date Retrieved: February 28, 2012.

4 Kim, I. T. and Simpson, M. F. *Separation of Fission Products from Molten LiCl-KCl Salt Used for Electrorefining of Metal Fuels*. I-NERI Annual Technical Progress Report, September, 2008.

5 Cho, T. Z., Yang, H. C., Park, G. H., Lee, H. S., and. Kim, I. T. Treatment of LiCl-KCl Waste Salt Delivered from Pyroprocessing of Spent Nuclear Fuel. (Jeju, Korea 2008), Proc. 2nd Int. Pyroprocessing Research Conf. (IPRC2008).

6 Cho, Y. Z., Park, G. H., Lee, H. S.,. Kim, I. T., and Han, D. S. Concentration of Cesium and Strontium elements involved in a LiCl Waste Salt by a Melt Crystallization Process. *Nuclear Technology*, 171 (2010), 325-334.

7 Koch, L. J. *Experimental Breeder Reactor II: An Integrated Experimental Fast Reactor Nuclear Power Station*. American Nuclear Society, La Grange Park, IL, 2008.

8 Goff, K. M., Benedict, R. W., and Levinskas, D. Spent Fuel Treatment at ANL-West. (Salt Lake City, UT 1994), Proc. of DOE Spent Nuclear Fuel Challenges and Initiatives.

9 Willit, J. L., Miller, W. E., and Battles, J. E. Electrorefing of Uranium and Plutonium - A Literature Review. *Journal of Nuclear Materials*, 195 (1992), 229-249.

10 Laider, J. J., Battles, J. E., Miller, W. E., Ackerman, J. P., and Carls, E. L.

Development of Pyroprocessing Technology. *Progress in Nuclear Energy*, 31 (1997), 131-140.

11 Benedict, R. W., Solbrig, C., Westphal, B., Johnson, T. A., Li, S. X., Marsden, K., and Goff, K. M. Pyroprocessing Progress at Idaho National Laboratory. (Boise, Idaho 2007), Proceedings of Global 2007.

12 Li, S. I., Johnson, T. A., Westphal, B. R., Goff, K. M., and Benedict, R. W. Electrorefining Experience for Pyrochemical Processing of Spent EBR-II Driver Fuel. (Tsukuba, Japan 2005), Proceedings of Global 2005.

13 Lexa, D. and Johnson, I. Occlusion and Ion Exchange in the Molten (Lithium Chloride-Potassium Cholride-Alkali Metal Chlorides) Salt+Zeolite 4A System with Alkali Metal Chlorides of Sodium, Rubidium, and Cesium. *Metallurgical and Materials Transactions B*, 32B (2001), 429-435.

14 Simpson, M. F. and Dunzik-Gougar, M. L. Two-Site Equilibrium Model for Ion Exchange between Monovalent Cations and Zeolite-A in a Molten Salt. *Industrial Engineering and Chemistry Research*, 42 (2003), 4208-4212.

15 Dunzik-Gouger, M. L., Simpson, M. F., and Scheetz, B. E. Two-Site Equilibrium Model for Ion Exchange Between Monovalent Cations and Zeolite-A in a Molten Salt. *Microporous and Mesoporous Materials*, 84 (2005), 366-372.

16 Phongikaroon, S. and Simpson, M. F. Two-Site Equilibrium Model for Ion Exchange Between Multivalent Cations and Zeolite-A in a Molten Salt. *AIChE Journal*, 52 (2006), 1736-1743.

17 Yoo, T. S., Frank, S. M., Simpson, M. F., Hahn, P. A., Battisti, T. J., and Phongikaroon, S. Salt-Zeolite Ion Exchange Equilibrium Studies for a Complete Set of Fission Products in Molten LiCl-KCl. *Nuclear Technology*, 171 (2010), 306-315.

18 Shaltry, M., Phongikaroon, S., and Simpson, M. F. Ion Exchange Kinetics of Fission Products between Molten Salt and Zeolite-A. *Microporus and Mesoporous Materials*,

152 (2012), 185-189.

19 Simpson, M. F., Yoo, T. S., Benedict, R. W., Phongikaroon, S., Frank, S., Sachdev, P., and Hartman, K. Srategic Minimization of High Level Waste from Pyroprocessing of Spent Nuclear Fuel. (Boise, Idaho 2007), Proc. of Global 2007.

20 Garandet, J. P. and Alboussiere, T. Bridgman Growth: Modelling and Experiments. *Progress in Crystal Growth and Characterization of Materials* (1999), 73-132.

21 Arkenbout, G. F. *Melt Crystallization Technology*. Technomic Publishing Company, Inc., Lancaster, Pennsylvania, 1995.

22 Ulrich, J. and Jones, M. J. Heat and Mass Transfer Operations - Crystallization. *Chemical Engineering and Chemical Process Technology*, Vol II.

23 Fukui, K. and Maeda, K. Direct numerical simulation of solid-layer crystallization from binary melt. *Journal of Crystal Growth*, 235 (2002), 633-639.

24 Wilcox, W. R. Zone Melting of Organic Compounds. *Chemical Reviews*, 64 (1964), 187-220.

25 Kakimoto, K., Eguchi, M., Watanabe, H., and Hibiya, T. In-Situ Observation of Impurity Diffusion Boundary Layer in Silicon Czochralski Growth. *Journal of Crystal Growth*, 99 (1990), 665-669.

26 Diehn, B., Rowland, F. S., and Wolf, A. P. Zone Refining for the Separation of Radioactive Trace Contaminants from Organic Compounds. *Analytical Chemistry*, 40 (1968), 60-64.

27 Pfann, W. G. Zone Melting Considered as a Multistage Separation Method. *Industrial and Engineering Chemical Fundamentals*, 8 (1969), 357-358.

28 Abrosmov, N. V., Rossolenko, S. N., Alex, V., Gerhardt, A., and Schroder, W. Single Crystal Growth of Si1-xGex by the Czochralski Technique. *Journal of Crystal*

Growth, 166 (1996), 657-662.

29 Pimutkar, S. M. and Ostrach, S. Convective Effects in Crystals Grown from Melt. *Journal of Crystal Growth*, 55 (1981), 614-646.

30 Lee, H. S., Oh, G. H., Lee, Y. S., Kim, I. T., Kim, E. H., and Lee, J. H. Concentrations of CsCl and SrCl2 from a Simulated LiCl Salt Waste Generated by Pyroprocessing by Using Czochralski Method. *Journal of Nuclear Science and Technology*, 46 (2009), 392-397.

31 Cheuvart, P., El-Hanani, U., Schneider, D., and Triboulet, R. CdTe and CdZnTe Crystals Grown by Horizontial Bridgman Technique. *Journal of Crystal Growth*, 101 (1990), 270-274.

32 Kim, D. H. and Brown, R. A. Modelling of the dynamics of HgCdTe growth by the vertical Bridgeman method. *Journal of Crystal Growth*, 114 (1991), 411-435.

33 Wibowo, C. Developing Crystallization Processes. *Chemical Engineering Progress*, 107 (2011), 21-31.

34 Seader, J. D. and Henley, E. J. *Separation Process Principles*. John Wiley & Sons, Inc., Hoboken, New Jersey, 1998.

35 Sangster, J. and Pelton, A. D. Thermodynamic Calculation of Phase Diagrams of the 60 Common-Ion Ternary Systems Containing Cations Li, Na, Rb, Cs, and Anions F, Cl, Br, I. *Journal of Phase Equilibria*, 12 (1991), 511-537.

36 Sangster, J and Pelton, A. D. Phase Diagrams and Thermodynamic Properties of the 70 Binary Alkali Halide Systems having Common Ions. *Journal of Physical Chemistry and Reference Data*, 16 (1987), 509-561.

37 Shujian, T., Qingfan, L., Shixiang, L., and Chaogui, Z. Phase Diagram of the Ternary System CeCl3-KCl-LiCl. *Journal of Alloys and Compounds*, 274 (1998), 142-147.

38 Prausnitz, J. M., Lichtenthaler, R. N., and Gomes de Azevedo, E. *Molecular Thermodynamics of Fluid-Phase Equilibria*. Prentice-Hall, Inc., Upper Saddle River, New Jersey, 1999.

39 Jackson, K. A., Gilmer, G. H., Temkin, D. E., and Beatty, K. M. Microsegregation far from equilibrium. *Journal of Crystal Growth*, 163 (1996), 461-469.

40 Hillert, M. and Sundman, B. A solute-drag treatment of the trasition from diffusion-controlled to diffusion less solidification. *Acta Metallurgica*, 25 (1977), 11-18.

41 Agren, J. A simplified treatment of the transition from diffusion controled to diffusion-less growth. *Acta Metallurgica*, 37 (1989), 181-189.

42 Goldman, L. M. and Aziz, M.J. A periodic stepwise growth model for the velocity and orientation dependence of solute trapping. *Journal of Materials Research*, 2 (1987), 524-527.

43 Scheil, E. Bemerkungen zur Schichtkristallbildung. *Zeitschrift fur Metallkunde*, 23 (1931), 237.

44 Rutter, J. W. and Chalmers, B. A Prismatic Substructure Formed during Solidification of Metals. *Canadian Journal of Physics*, 31 (1953), 15-39.

45 Tiller, W. A., Jackson, K. A., Rutter, J. W., and Chalmers, B. The Redistribution of Solute Atoms During The Solidification of Melt. *Acta Metallurgica*, 1 (1953), 428-437.

46 Burton, J. A., Prim, R. C., and Slichter, W. P. The Distribution of Solute in Crystals Grown from the Melt. Part I. Theortical. *The Journal of Chemical Physics*, 21 (1953), 1987-1991.

47 Burton, J. A., Prim, R. C., and Slichter, W. P. Distribution of Solute in Crystals Grown from the Melt. Part II. Experimental. *The Journal of Chemical Physics*, 21 (1953), 1991-1996.

48 Favier, J. J. Macrosegregation-I Unified Analysis during Non-Steady State Solidification. *Acta Metallurgica*, 29 (1981), 197-204.

49 Favier, J. J. Macrosegegation-II A comparative Study of Theories. *Acta Metallurgica*, 29 (1981), 205-214.

50 Camel, D. and Favier, J. J. Thermal Convection and Longitudinal Macrosegregation in Horizontal Bridgman Crystal Growth I. Order of Magnitude Analysis. *Journal of Crystal Growth*, 67 (1984), 42-56.

51 Camel, D. and Favier, J. J. Thermal Convection and Longitudinal Macrosegregation in Horizontal Bridgman Crystal Growth II. Practical Laws. *Journal of Crystal Growth*, 67 (1984), 57-67.

52 Garandet, J. P., Duffar, T., and Favier, J. J. On the Scaling Analysis of the Solute Boundary Layer in Idealized Growth Configurations. *Journal of Crystal Growth*, 106 (1990), 437-444.

53 Batchelor, G. K. Heat Transfer by Free Convection Across a Closed Cavity Between Vertical Boundaries at Different Temperatures. *Quarterly of Applied Mathamatics*, XII (1954), 209-233.

54 Kaddeche, S., Ben Hadid, H., and Henry, D. Macrosegregation and Convection in the Horizontal Bridgman Configuration I. Dilute Alloys. *Journal of Crystal Growth*, 135 (1994), 341-353.

55 Kaddeche, S., Garandet, J. P., Barat, C., Ben Hadid, H., and Henry, D. Interface curvature and convection related macrosegregation in the vertical Bridgman configuration. *Journal of Crystal Growth*, 158 (1996), 144-152.

56 Verhoeven, J. D., Gill, W. N., Puszynski, J. A., and Ginde, R. M. Macrosegregation during Convection-Free Plane Front Solidification I. Rectilnear Geometry. *Journal of Crystal Growth*, 89 (1988), 189-201.

57 Verhoeven, J. D., Gill, W. N., Puszynski, J. A., and Ginde, R. M. Macrosegregation During Convection-Free Plane Front Solidification II. Cylindrical and Spherical Geometries. *Journal of Crystal Growth*, 97 (1989), 254-266.

58 Smith, V. G., Tiller, W. A., and Rutter, J. W. A Mathamatical Analysis of Solute Redistribution during Solidification. *Canadian Journal of Physics*, 33 (1955), 723-745.

59 Bennon, W. D and Incropera, F. P. A continuum model for momentium, heat and species transport in binary solid-liquid phase change systems-I. Model Formulation. *International Journal of Heat and Mass Transfer*, 30 (1987), 2161-2170.

60 Chang, C. J. and Brown, R. A. Radial Segregation Induced by Natural Convection and Melt/Solid Interface Shape in Vertical Bridgman Growth. *Journal of crystal Growth*, 63 (1983), 343-364.

61 Voller, V. R., Brent, A. D., and Prakash, C. The modelling of heat, mass, and solute transport in solidification systems. *International Journal of Heat and Mass transfer*, 32 (1989), 1719-1731.

62 Kim, D. H. and Brown, R. A. Modelling of the dynamics of HgCdTe growth by the Vertical Bridgman Method. *Journal of Crystal Growth*, 114 (1991), 411-434.

63 Prescott, P. J., Incropera, F. P., and Gaskell, D. R. Convective Transport Phenomena and Macrosegregation during Solidification of a binary metal alloy: II=-Experiments and Comparisons with Numerical Predictions. *Transactions of ASME*, 116 (1994), 742-749.

64 Krane, M. J. M. and Incropera, F. P. Experimental Validation of Continuum Mixture Model for Binary Alloy Solidification. *Journal of Heat Transfer*, 119 (1997), 783-791.

65 Fukui, K. and Maeda, K. Distribution of solute at solid-liquid interface during solidification of melt. *Journal of Chemical Physics*, 109 (1998), 7468-7473.

66 Fukui, K and Maeda, K. Melt Layer Solidification of Fatty acids in a rectangular cell. *Journal of Chemical Physics*, 112 (2000), 1554-1559.

67 Fukui, K. and Maeda, K. Effects of crystal growth rate and heat and mass transfer on solute distribution. *Chemical Engineering Science*, 57 (2002), 3133-3140.

68 Janz, G. J. Thermodynamic and Transport Properties for Molten Salts: Correlation Equations for Critically Evaluated Density, Surface Tension, Electrical Conductance, and Viscosity Data. *Journal of Physical and Chemical Reference Data*, 17 (1988), Supplement No. 2.

69 Incropera, F.P., Dewitt, D. P., Bergman, T. L., and Lavine, A. S. *Fundamentals of Heat and Mass Transfer*. John Wiley & Sons, Inc., Hoboken, 2007.

70 Slater, J. C. Atomic Radii in Crystals. *Journal of Chemical Physics*, 41 (1964), 3199.

71 Janz, G. J. and Bansal, N. P. Molten Salts Data: Diffusion Coefficients in Single and Multi-Component Salt Systems. *Journal of Physical and Chemical Reference Data*, 11 (1982), 505.

Appendix A - MATLAB Programs

A.1 Main Program

```
rate1 = 1.8;     % Advancement Rate (mm/hr)
D = 6.05e-10;    % Diffusion Coefficient (m2/s)
LID = 1;         % Lid configuration, 1 means no-lid, 2 means lid
SIZE = 50;       % Amount of salt used, 50 g and 400 g
DELTAT = 200;    % Difference between furnace zones, 200 or 300.
COMP = 0.03;     % Initial composition
points = 1000;   % Number of points used in the solution

% Function to import the experimental data and fit parameters
[Exp_C,Exp_P,L,radius,height,datapts,del,ko,Ev,Eh,rate] = ...
    ExperimentalData(rate1,LID,SIZE,DELTAT,COMP);



dx = L/points; % mesh size (m)
R = rate/(3600*1000); % Effective growth rate (m/s)
delta = del*R/D;   % Transport parameter
kp = ko/(ko+(1-ko)*exp(-delta)); % keff

%% Initiate Variables
rootsA = zeros(20,1);       % Matrix to store alpha roots
beta = zeros(5,1);          % Matrix to store Beta roots
sumterms = zeros(points,1); % Matrix used to calculate summation terms
Cs = zeros(points,2);       % Solution up to x*
Csf = zeros(points,3);      % Solution after x*
CsTrue = zeros(points,2);   % Combination of Cs and Csf
error = zeros(points-1,2);  % Matrix used to find x*

%% Find the roots alpha and beta of the Eqns.
test = (2*ko-1)*delta/2;
for i = 1:20
    if test < -1
        %Favier part II, pg. 206
        alpha = fzero(@(alpha)alpha*coth(alpha)-(1-2*ko)*delta/2,i);
        rootsA(i,1) = alpha;
        break
    else
        %Favier part I, Eqn. 8
        alpha = fzero(@(alpha)2*alpha*cos(alpha)-(1-
2*ko)*delta*sin(alpha),i);
    end
    rootsA(i,1) = alpha;
end
% Eliminate diplicate roots
rootsA1 = sd_round(abs(rootsA),5);
rootsU = unique(rootsA1);
rootsU = rootsU(rootsU~=0);

for j = 1:5
    if test < -1
```

```
        beta(1,1) = 1-(1-2*ko)^2*tanh(rootsU(1,1))^2;
    else
        beta(j,1) = 1+(1-2*ko)^2*tan(rootsU(j,1))^2;
    end
end

%% Calculate the Initial Solid Concentration (Favier part 1, Eqn. 9")
x = 0;
for i = 1:points
    if test < -1
        Cs(i,1) = kp*(1-(8*(1-ko)*(ko+(1-ko)*exp(-delta))/delta*...
            (sinh(rootsU(1,1))^2*exp(-beta(1,1)*delta*x/(4*del)))/...
            (-beta(1,1)*(1-((2*cosh(rootsU(1,1))^2)/((1-
2*ko)*delta))))));
    else
        sumterms(i,1) = 0;
        for j = 1:5
            term = ((sin(rootsU(j,1))^2*exp(-
beta(j,1)*delta*x/(4*del)))/...
                (beta(j,1)*(1-(2*cos(rootsU(j,1))^2)/((1-
2*ko)*delta))));
            sumterms(i,1) = sumterms(i,1)+term;
        end
        Cs(i,1) = kp*(1-(8*(1-ko)*(ko+(1-ko)*exp(-delta))/delta)*...
            sumterms(i,1));
    end
    Cs(i,2) = x/L;
    x = x+dx;
end
%% Calculate x* or XStar
x = 0;
for i = 1:points-1
    rhs = kp*((1-Cs(i,1))/(L-x));
    lhs = (Cs(i+1,1)-Cs(i,1))/dx;
    error(i,1) = (rhs-lhs)^2;
    error(i,2) = i;
    x = x+dx;
end
error1 = sortrows(error,1);
XStar = error1(1,2);

%% Calculate End effects
x = 0;
for i = 1:points
    Csf(i,1) = Cs(XStar,1)+kp/(1-kp)*(1-Cs(XStar,1))*...
        ((((L-x)/(L-Cs(XStar,2)*L))^(kp-1))-1);
    Csf = real(Csf);
    Csf(i,2) = x/L;
    x = x+dx;
end
%% Merge Initial and End effects together
for i = 1:points
    if i <= XStar
        CsTrue(i,1) = Cs(i,1)*0.03;
        CsTrue(i,2) = Cs(i,2);
    else
```

```
        CsTrue(i,1) = Csf(i,1)*0.03;
        CsTrue(i,2) = Csf(i,2);
    end
end


%% Calculate R2
diff_sqrd = zeros(points,3);
m_comp = zeros(datapts,2);
sqrd = zeros(datapts,3);
Exp(1:datapts,1) = Exp_P;
Exp(1:datapts,2) = Exp_C;
for j = 1:datapts
    Value = Exp(j,1);
    for k = 1:points
        diff_sqrd(k,1) = (Value-CsTrue(k,2))^2;
        diff_sqrd(k,2) = CsTrue(k,2);
        diff_sqrd(k,3) = CsTrue(k,1);
    end
    close_val = sortrows(diff_sqrd,1);
    P1 = close_val(1,2);
    P2 = close_val(2,2);
    C1 = close_val(1,3);
    C2 = close_val(2,3);
    m_comp(j,1) = Value;
    m_comp(j,2) = ((Value-P1)/(P2-P1))*(C2-C1)+C1;
end
ybar = mean(Exp_C);
for j = 1:datapts
    sqrd(j,1) = ((Exp(j,2)-m_comp(j,2))/Exp(j,2))^2;
    sqrd(j,2) = (Exp(j,2)-ybar)^2;
    sqrd(j,3) = (Exp(j,2)-m_comp(j,2))^2;
end
R_squared = sd_round((sum(sqrd(1:datapts,2))-...
    sum(sqrd(1:datapts,3)))/sum(sqrd(1:datapts,2)),2);

%% Plot data
figure(1)
plot(Exp_P(1:datapts,1),Exp_C(1:datapts,1),'o',...
    CsTrue(1:points,2),CsTrue(1:points,1),'black');
axis([0 1 0 .07]);
xlabel('h/h0');
ylabel('Local Mass Fraction');
title('Boundary Layer Model');
if LID == 1
    sLID = 'NO LID';
else
    sLID = 'LID';
end
s{1} = sprintf('Exp: (%g mm/hr, %g grams, dT=%g C, %s case)',...
    rate1,SIZE,DELTAT,sLID);
s{2} = sprintf('Favier R^2 = %g',R_squared);
leg1 = legend(s{1:2},'Location','Northwest');
set(leg1,'FontSize',7.2);
set(leg1,'Box','off');
```

A.2 Experimental Data and Conditions

```
function [Exp_C,Exp_P,length,...
    radius,height,datapts,del,ke,Ev,Eh,rate] = ...
    ExperimentalData(rate1,LID,SIZE,DELTAT,COMP)
%ExperimentalData - This function is used to call the experimental
%conditions and data for each experiment.
%   INPUTS
%    rate1 = the set advancement rate in mm/hr ...(1.8, 3.2, and 5.0)
%    LID = 1 or 2, 1 is for no-lid configuration
%    SIZE = 50 or 400, 50 is for the fifty g sample
%    DELTAT = 200 or 300, 200 represents the 200C termperature
difference
%    COMP = the initial composition (0.03, 0.05, and 0.01)%
%   OUTPUTS
%     Exp_C = the experimental composition data
%     Exp_P = the experimental Position data
%     Ev = the vertical error
%     Eh = the horizontal error
%     length = the height of the salt (m)
%     radius = the radius of salt (m)
%     datapts = the number of experimental data points
%     del = thickness of boundary layer (m)
%     ke = the segregation coefficient
%     Ev = the vertical error bar data
%     Eh = the horizontal error bar data
%     rate = the effective growth rate

% Start of Function
if rate1 == 1.8 && LID == 1 && SIZE == 50 && DELTAT == 200 &&...
        COMP == 0.03
    %1.8 mm/hr
    Exp_C = [0.005780 0.015201 0.031859 0.045783 0.062060]';
    Exp_P = [0.12 0.39 0.68 0.83 0.93]';
    Ev = [0.000255 0.000898 0.001182 0.001966 0.002664]';
    Eh = [0.024570 0.026181 0.029535 0.031685 0.033255]';
    length = 0.041;
    radius = 0.0145;
    height = 0.02;
    datapts = 5;
    del = 0.0013;
    ke = 0.2267;
    rate = 1.75;
elseif rate1 == 1.8 && LID == 2 && SIZE == 50 && DELTAT == 200 &&...
        COMP == 0.03
    Exp_C = [0.00748 0.02305 0.032473 0.041227 0.053056]';
    Exp_P = [0.10869 0.402173 0.608695 0.804347 0.956521]';
    Ev = [0.001431 0.001473 0.000864 0.001550 0.001987]';
    Eh = [0.021867 0.023431 0.025449 0.027898 0.030082]';
    length = 0.046;
    radius = 0.014;
    height = 0.02;
    datapts = 5;
    del = 0.00112;
```

```
    ke = .4253;
    rate = 1.95;
elseif rate1 == 1.8 && LID == 1 && SIZE == 50 && DELTAT == 300 &&...
        COMP == 0.03
    Exp_C = [0.012981 0.015329 0.027018 0.040228 0.056338]';
    Exp_P = [0.136363 0.431818 0.613636 0.772727 0.909090]';
    Ev = [0.001133 0.001339 0.001665 0.001174 0.002787]';
    Eh = [0.022937 0.024755 0.026665 0.028721 0.030715]';
    length = 0.044;
    radius = 0.0145;
    height = 0.02;
    datapts = 5;
    del = 0.00105;
    ke = .2839;
    rate = 1.8;
elseif rate1 == 1.8 && LID == 1 && SIZE == 400 && DELTAT == 200 &&...
        COMP == 0.03
    Exp_C = [0.010763 0.007176 0.008649 0.012207 0.022136 0.026815...
        0.034097 0.046014 0.058289 0.075299]';
    Exp_P = [0.091954 0.195402 0.298850 0.390804 0.494252 0.586206...
        0.689655 0.781609 0.873563 0.954023]';
    Ev = [0.000767 0.001250 0.00151 0.002126 0.001569 0.001898...
        0.002409 0.003240 0.00409 0.002839]';
    Eh = [0.011542 0.011711 0.011996 0.012340 0.012822 0.013323
0.013962...
        0.014588 0.015262 0.015886]';
    length = 0.087;
    radius = 0.0285;
    height = 0.03;
    datapts = 10;
    del = 0.00133;
    ke = .1568;
    rate = 2.52;
elseif rate1 == 3.2 && LID == 1 && SIZE == 50 && DELTAT == 200 &&...
        COMP == 0.03
    Exp_C = [0.0127 0.0237 0.0301 0.0392 0.0506]';
    Exp_P = [0.12 0.44 0.65 0.8 0.91]';
    Ev = [0.000827 0.001139 0.001434 0.001863 0.00212]';
    Eh = [0.023412 0.025424 0.027751 0.029815 0.031396]';
    length = 0.043;
    radius = 0.0145;
    height = 0.02;
    datapts = 5;
    del = 0.00121;
    ke = 0.1753;
    rate = 3.3;
elseif rate1 == 3.2 && LID == 2 && SIZE == 50 && DELTAT == 200 &&...
        COMP == 0.03
    Exp_C = [0.013019 0.020796 0.034575 0.044835 0.05834]';
    Exp_P = [0.108695 0.413043 0.630434 0.804347 0.934782]';
    Ev = [0.002489 0.000597 0.000989 0.001277 0.001213]';
    Eh = [0.021867 0.023520 0.025698 0.027898 0.02975]';
    length = 0.046;
    radius = 0.014;
    height = 0.02;
    datapts = 5;
    del = 0.00111;
```

```
    ke = .2285;
    rate = 2.85;
elseif rate1 == 3.2 && LID == 1 && SIZE == 50 && DELTAT == 300 &&...
        COMP == 0.03
    %3.2 mm/hr
    Exp_C = [0.01960 0.022652 0.030555 0.042234 0.05594]';
    Exp_P = [0.16279 0.418604 0.651162 0.790697 0.88372]';
    Ev = [0.00092 0.001036 0.000928 0.001232 0.001675]';
    Eh = [0.023561 0.025211 0.027751 0.029647 0.031035]';
    length = 0.043;
    radius = 0.0145;
    height = 0.02;
    datapts = 5;
    del = 0.00104;
    ke = .2529;
    rate = 3.08;
elseif rate1 == 3.2 && LID == 1 && SIZE == 400 && DELTAT == 200 &&...
        COMP == 0.03
    Exp_C = [0.013229 0.023357 0.01665 0.019148 0.026515 0.029344...
        0.031992 0.041482 0.055334 0.067513]';
    Exp_P = [0.084210 0.2 0.315789 0.442105 0.557894 0.652631
0.736842...
        0.831578 0.915789 0.957894]';
    Ev = [0.001012 0.000814 0.000739 0.000882 0.001072 0.000951
0.001213...
        0.001562 0.002106 0.002555]';
    Eh = [0.010563 0.010734 0.011038 0.011509 0.01205 0.012569
0.013075...
        0.013690 0.014273 0.014576]';
    length = 0.095;
    radius = 0.028;
    height = 0.03;
    datapts = 10;
    del = 0.00114;
    ke = .1219;
    rate = 4.13;
elseif rate1 == 5 && LID == 1 && SIZE == 50 && DELTAT == 200 &&...
        COMP == 0.03
    %5 mm/hr
    Exp_C = [0.015975 0.025643 0.027922 0.031831 0.044844]';
    Exp_P = [0.12 0.45 0.69 0.81 0.88]';
    Ev = [0.001249 0.001227 0.00119 0.001517 0.00209]';
    Eh = [0.023977 0.026132 0.028933 0.030633 0.031730]';
    length = 0.042;
    radius = 0.0145;
    height = 0.02;
    datapts = 5;
    del = 0.00125;
    ke = .1007;
    rate = 4.7;
elseif rate1 == 5 && LID == 1 && SIZE == 50 && DELTAT == 300 &&...
        COMP == 0.03
    %5 mm/hr
    Exp_C = [0.017371 0.019213 0.023186 0.033201 0.055901]';
    Exp_P = [0.139534 0.279069 0.558139 0.767441 0.895348]';
    Ev = [0.000255 0.000898 0.001182 0.001966 0.002664]';
    Eh = [0.024570 0.026181 0.029535 0.031685 0.033255]';
```

```
    length = 0.043;
    radius = 0.0145;
    height = 0.02;
    datapts = 5;
    del = 0.00103;
    ke = .1142;
    rate = 4.82;
elseif rate1 == 5 && LID == 2 && SIZE == 50 && DELTAT == 200 &&...
        COMP == 0.03
    Exp_C = [0.007756 0.02313 0.034119 0.04461 0.048621]';
    Exp_P = [0.127659 0.446808 0.638297 0.829787 0.957446]';
    Ev = [0.000847 0.002426 0.003097 0.004040 0.004719]';
    Eh = [0.021449 0.023303 0.02524 0.02764 0.029456]';
    length = 0.047;
    radius = 0.0135;
    height = 0.02;
    datapts = 5;
    del = 0.00102;
    ke = .1666;
    rate = 5.21;
elseif rate1 == 5 && LID == 1 && SIZE == 400 && DELTAT == 200 &&...
        COMP == 0.03
    Exp_C = [0.017030 0.019042 0.014697 0.024324 0.025294 0.026997...
        0.031175 0.038923 0.057798 0.065668]';
    Exp_P = [0.053763 0.161290 0.204301 0.376344 0.505376 0.602150...
        0.677419 0.784946 0.88172 0.946236]';
    Ev = [0.00143 0.001583 0.001207 0.001089 0.001571 0.001676...
        0.001849 0.002300 0.002743 0.003594]';
    Eh = [0.010768 0.010891 0.010974 0.011488 0.012047 0.012551
0.012987...
        0.013669 0.014335 0.014803]';
    length = 0.093;
    radius = 0.0285;
    height = 0.03;
    datapts = 10;
    del = 0.00119;
    ke = .0394;
    rate = 6.42;
elseif rate1 == 5 && LID == 1 && SIZE == 50 && DELTAT == 200 &&...
        COMP == 0.05
    Exp_C = [0.019390 0.039203 0.050345 0.068891 0.090007]';
    Exp_P = [0.119047 0.452380 0.642857 0.80952 0.928571]';
    Ev = [0.000255 0.000898 0.001182 0.001966 0.002664]';
    Eh = [0.024570 0.026181 0.029535 0.031685 0.033255]';
    length = 0.045;
    radius = 0.0145;
    height = 0.02;
    datapts = 5;
    del = 0.0016;
    ke = .2014;
    rate = 5.0;
elseif rate1 == 5 && LID == 1 && SIZE == 50 && DELTAT == 200 &&...
        COMP == 0.01
    Exp_C = [0.001994 0.007735 0.006859 0.014043 0.02090]';
    Exp_P = [0.083333 0.333333 0.583333 0.75 0.875]';
    Ev = [0.000255 0.000898 0.001182 0.001966 0.002664]';
    Eh = [0.024570 0.026181 0.029535 0.031685 0.033255]';
```

```
    length = 0.047;
    radius = 0.014;
    height = 0.02;
    datapts = 5;
    del = 0.0016;
    ke = .202;
    rate = 5.0;
elseif rate1 == 5 && LID == 3 && SIZE == 50 && DELTAT == 200 &&...
        COMP == 0.03
    %CeCl3
    Exp_C = [0.001963 0.00456 0.006444 0.014236 0.214486]';
    Exp_P = [0.166666 0.416666 0.625 0.770833 0.9375]';
    Ev = [0.00020 0.000483 0.000683 0.001508 0.022753]';
    Eh = [0.021120 0.022569 0.024567 0.026304 0.028556];
    length = 0.048;
    radius = 0.0135;
    height = 0.02;
    datapts = 5;
    del = 0.0016;
    ke = .2149;
    rate = 5.0;
end
end
```

Appendix B - Photos of Grown Crystals

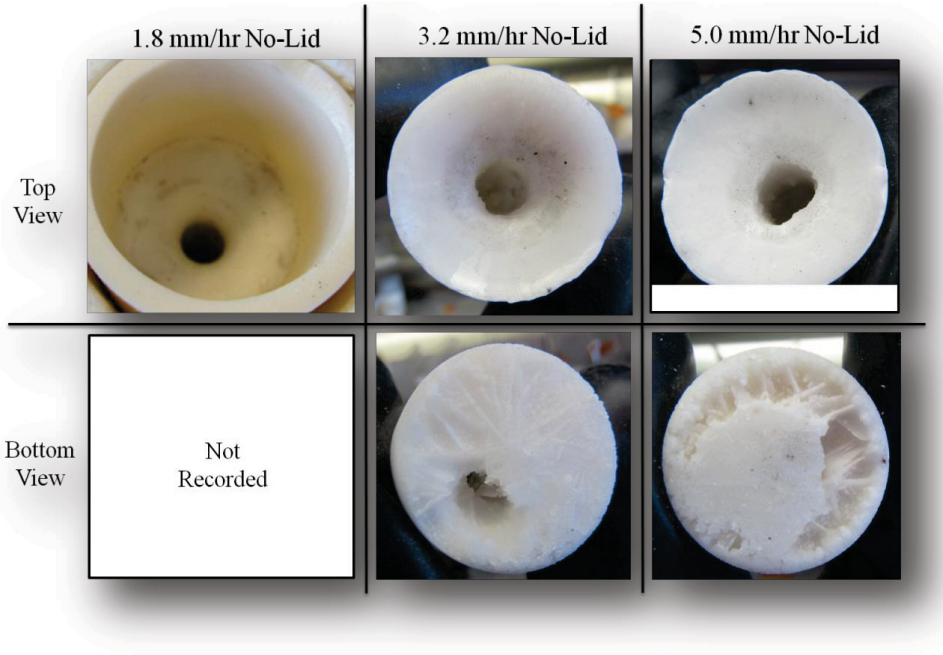

Figure B.1 Top and bottom view of grown crystal ingots of 3 wt% salt with a no-lid configuration.

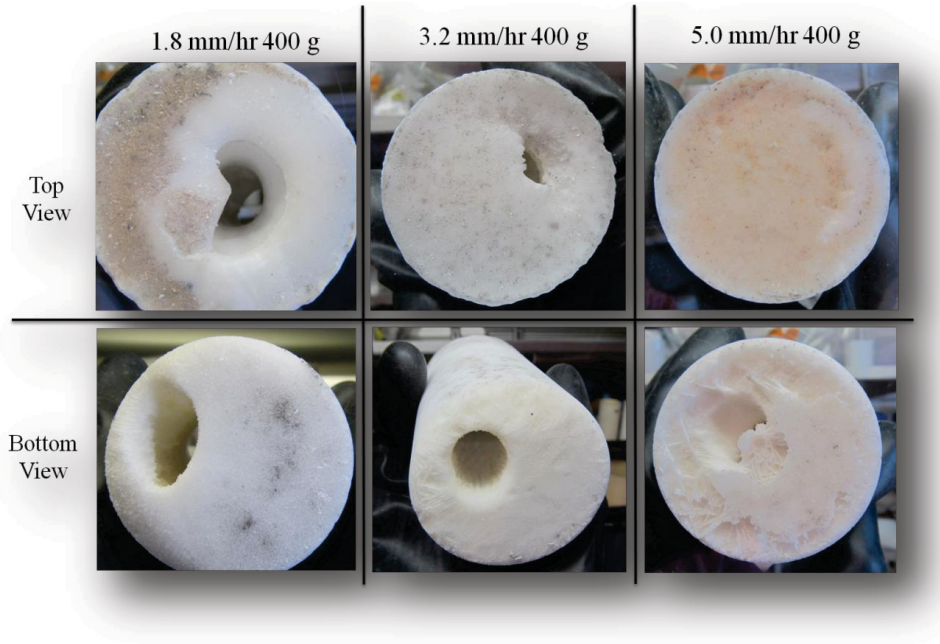

Figure B.2: Top and bottom view of crystals grown from a 3 wt% salt. 400 g samples were used.

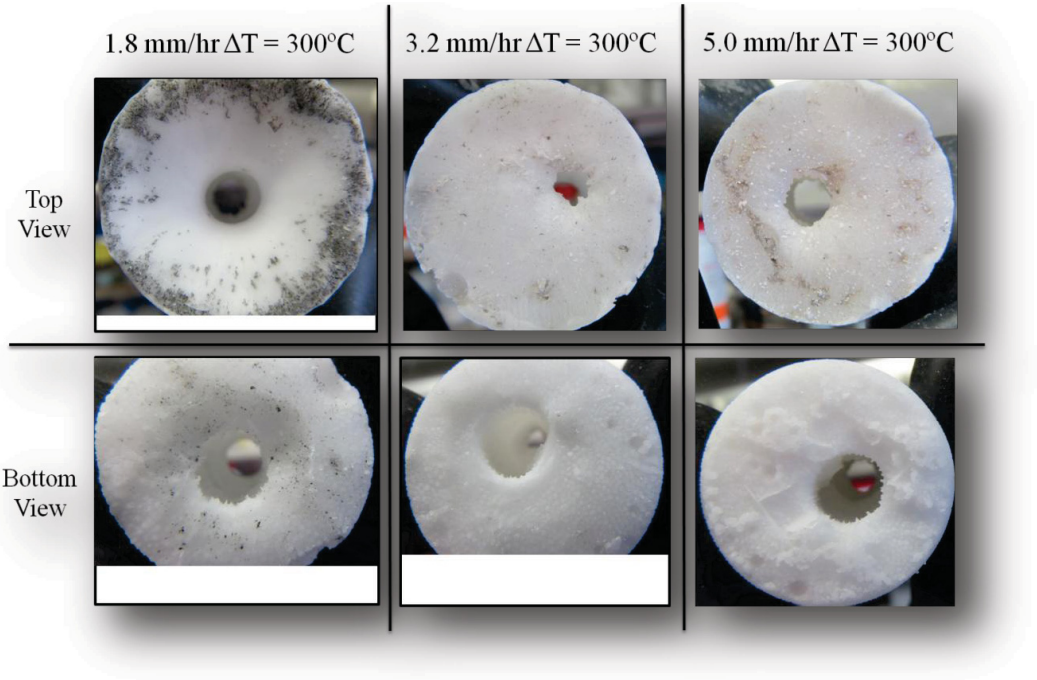

Figure B.3: Top and bottom view of crystals grown from a 3 wt% salt with a ΔT of 300°C.

Appendix C - Temperature Profiles

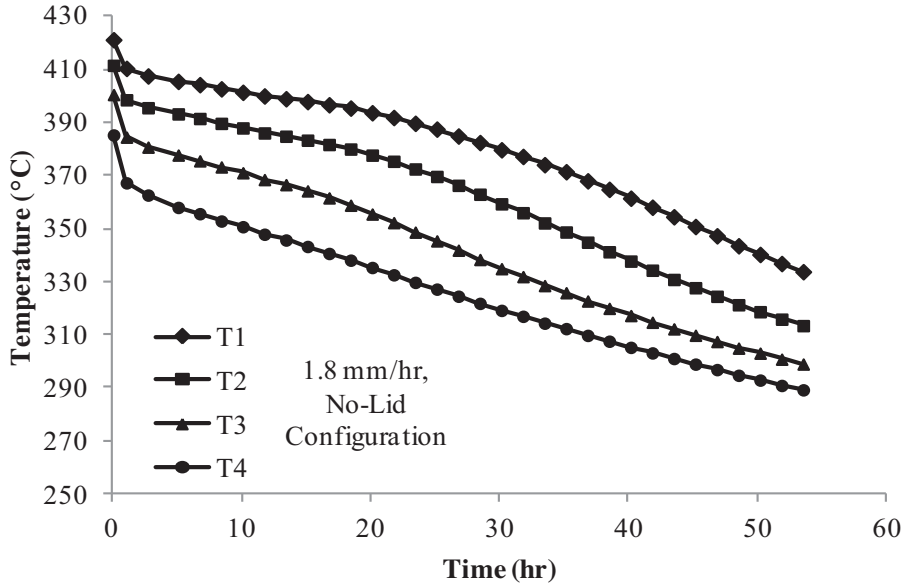

Figure C.1: Temperature profile for the 1.8 mm/hr, 50 g, no-lid configuration, with a ΔT of 200°C.

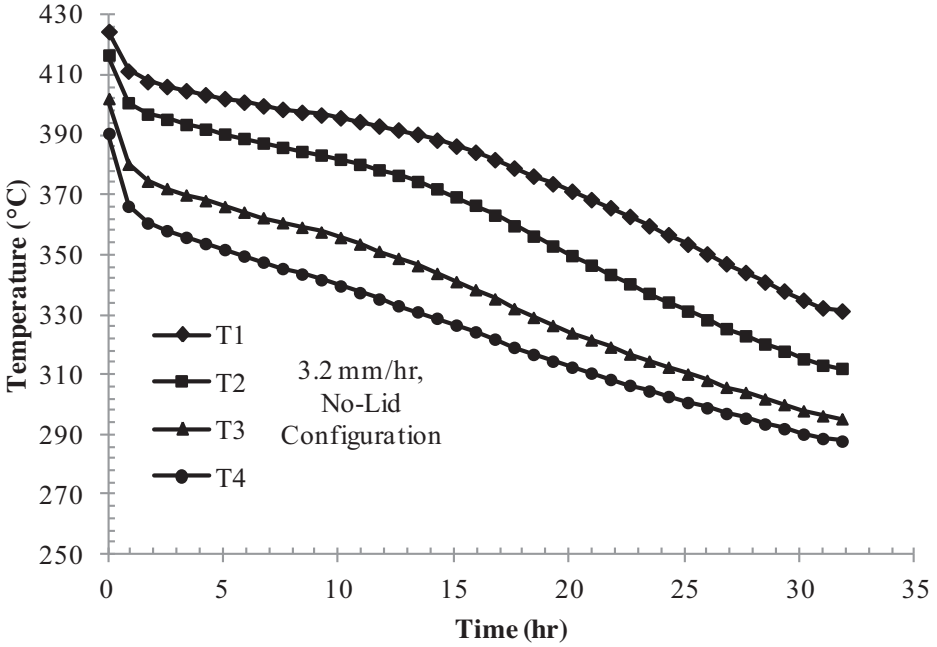

Figure C.2: Temperature profile for the 3.2 mm/hr, 50 g, no-lid configuration, with a ΔT of 200°C.

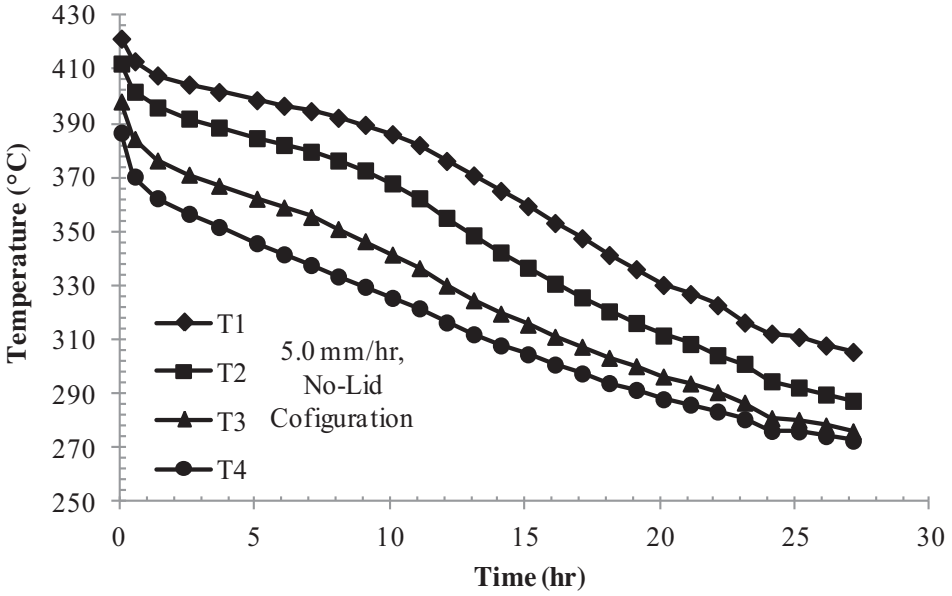

Figure C.3: Temperature profile for the 5.0 mm/hr, 50 g, no-lid configuration, with a ΔT of 200°C.

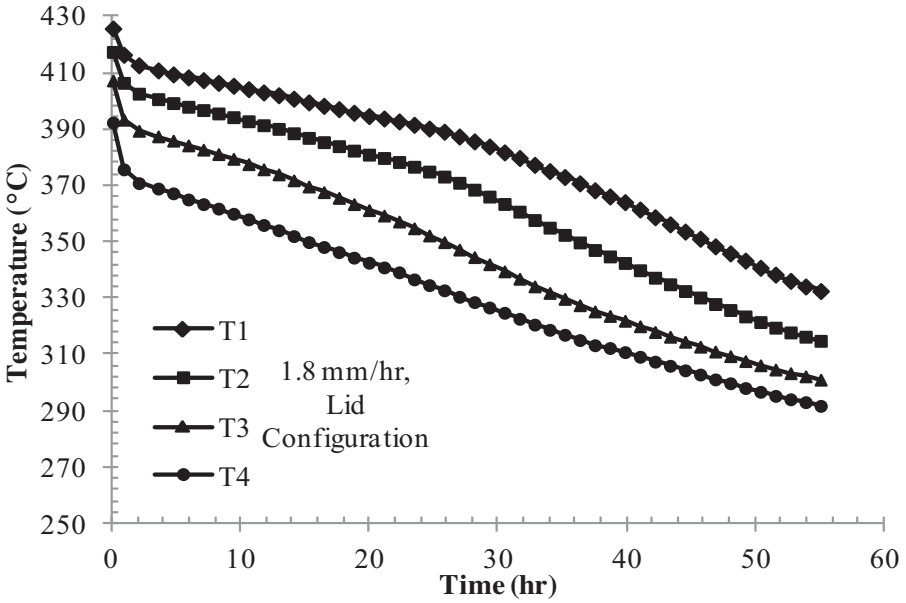

Figure C.4: Temperature profile for the 1.8 mm/hr, 50 g, lid configuration, with a ΔT of 200°C.

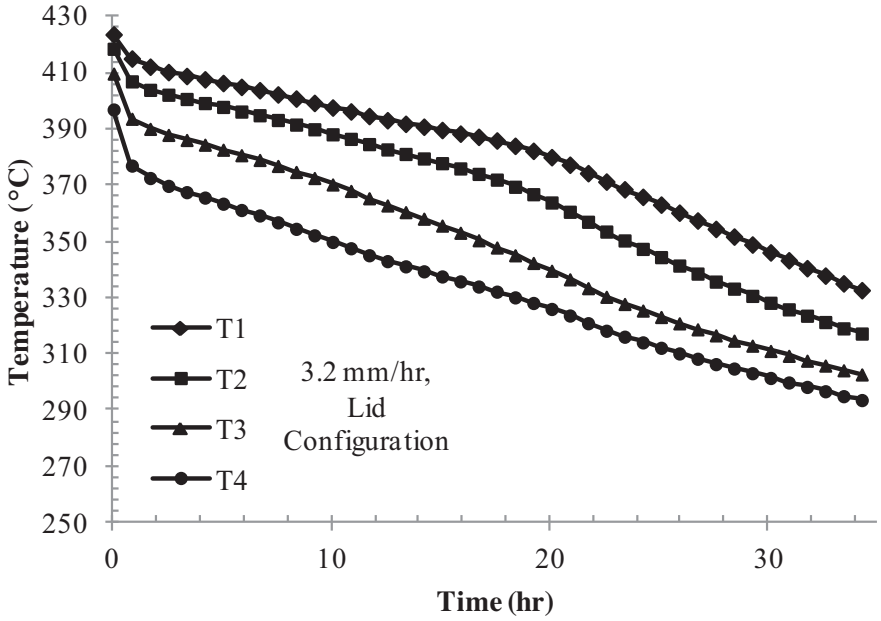

Figure C.5: Temperature profile for the 3.2 mm/hr, 50 g, lid configuration, with a ΔT of 200°C.

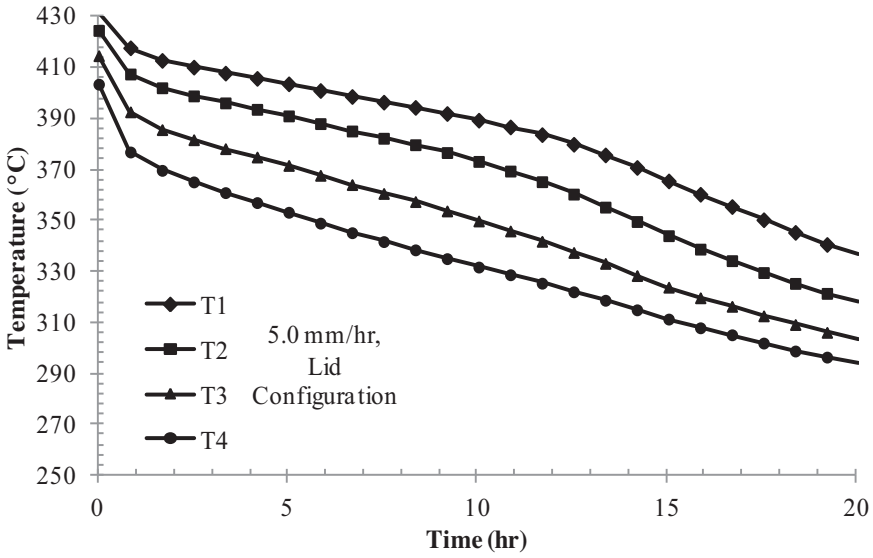

Figure C.6: Temperature profile for the 5.0 mm/hr, 50 g, lid configuration, with a ΔT of 200°C.

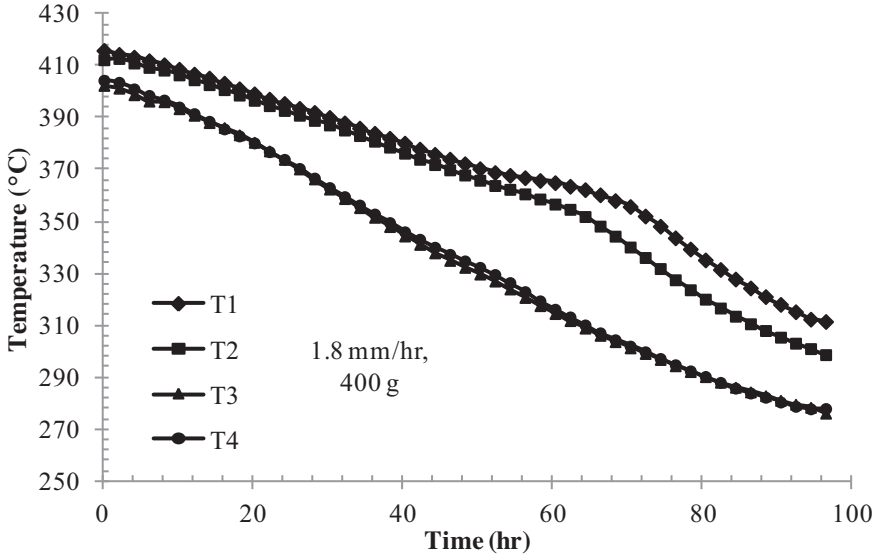

Figure C.7: Temperature profile for the 1.8 mm/hr, 400 g, no-lid configuration, with a ΔT of 200°C.

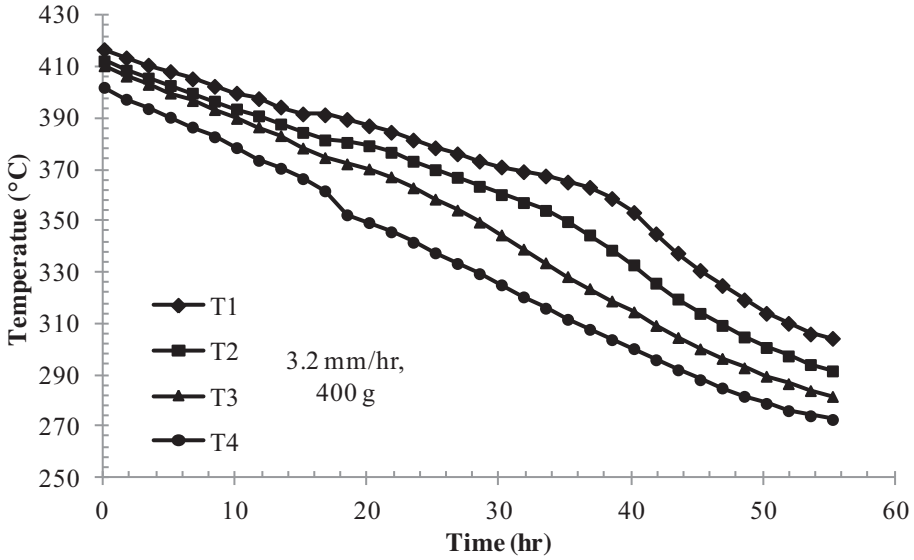

Figure C.8: Temperature profile for the 3.2 mm/hr, 400 g, no-lid configuration, with a ΔT of 200°C.

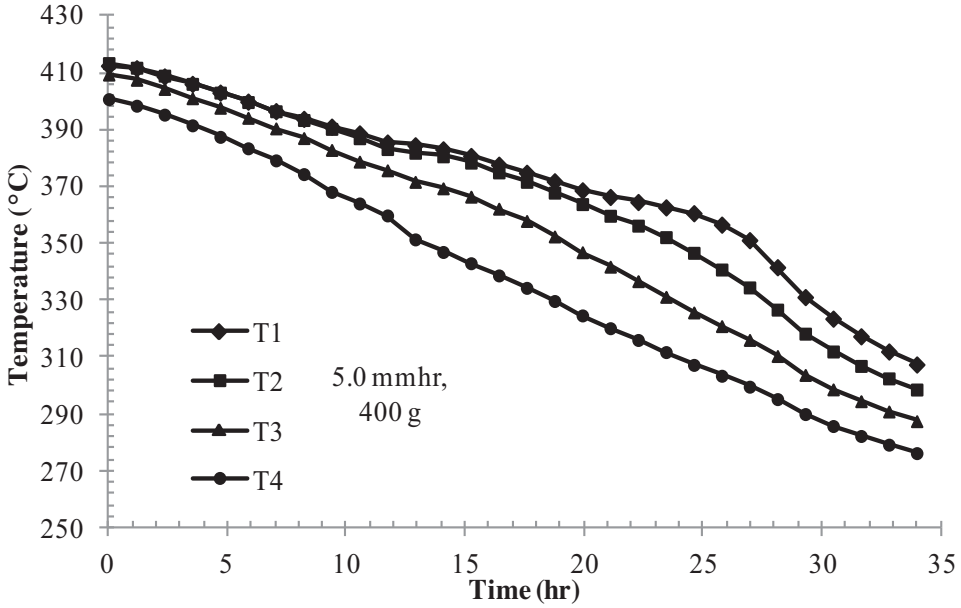

Figure C.9: Temperature profile for the 5.0 mm/hr, 400 g, no-lid configuration, with a ΔT of 200°C.

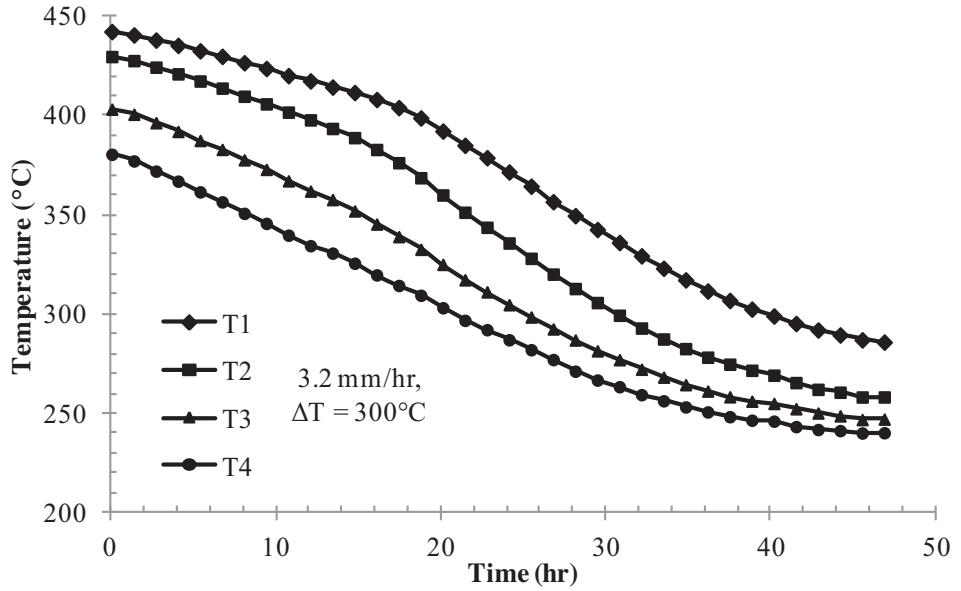

Figure C.10: Temperature profile for the 3.2 mm/hr, 50 g, no-lid configuration, with a ΔT of 300°C.

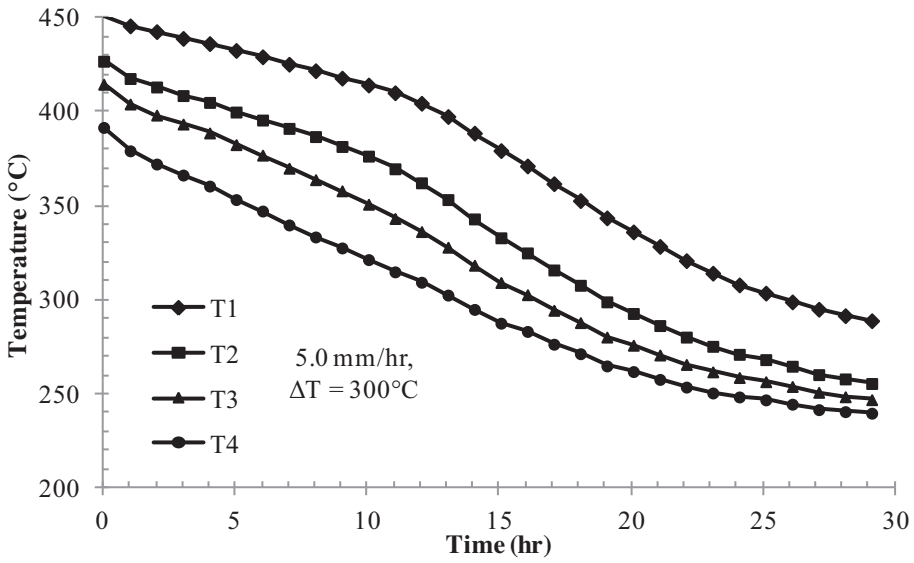

Figure C.11: Temperature profile for the 5.0 mm/hr, 50 g, no-lid configuration, with a ΔT of 300°C.

Appendix D - Local Mass Fraction Plots

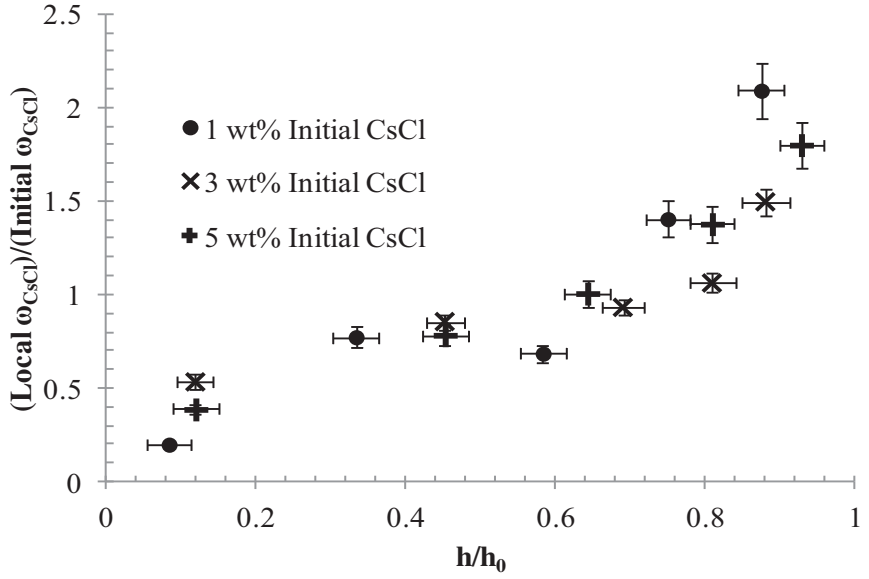

Figure D.1: Comparison of the 1 wt%, 3 wt%, and 5 wt% CsCl salts run at 5 mm/hr with a no-lid configuration and 50 g salt samples

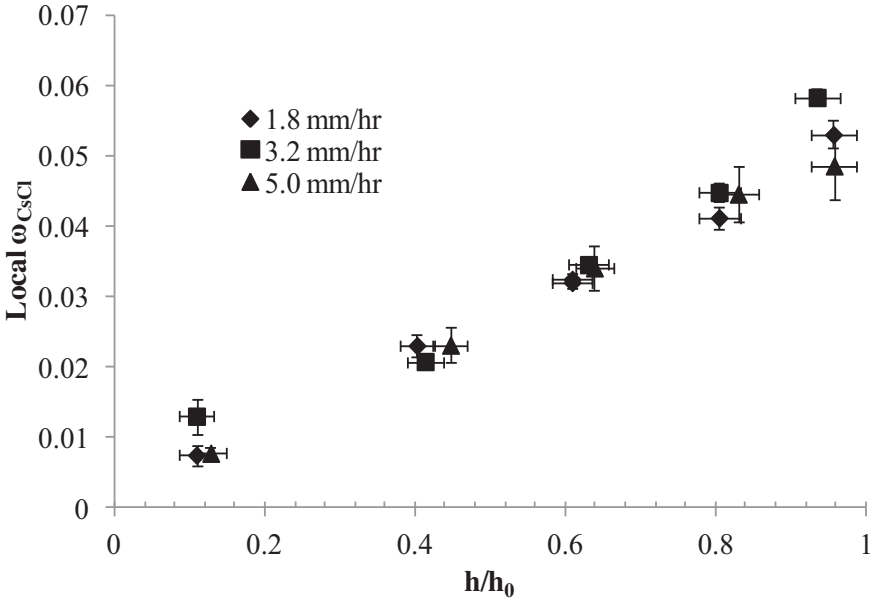

Figure D.2: Comparison of the local weight fraction at varying rates for a 3 wt% CsCl, 50 g salt sample run with a ΔT of 200°C and a lid configuration.

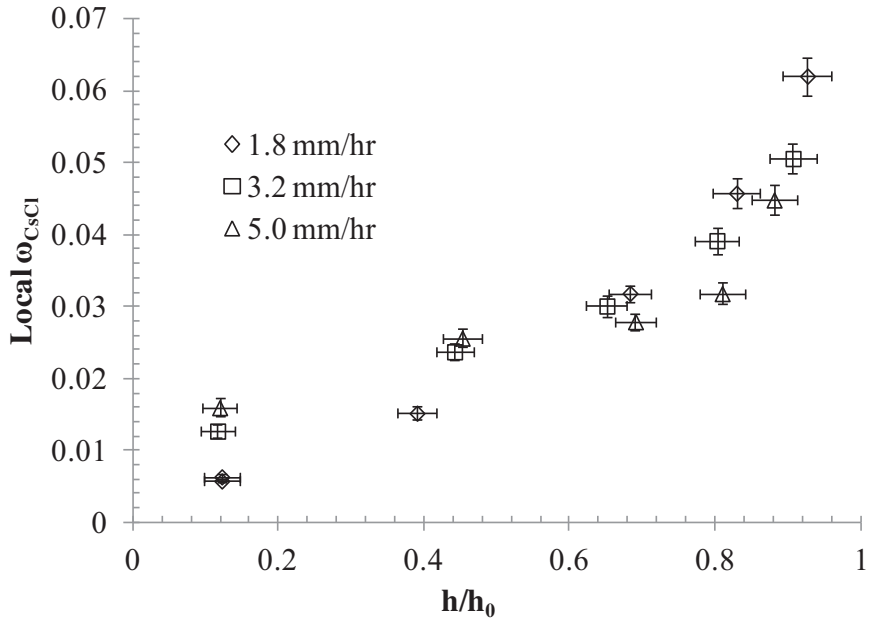

Figure D.3: Comparison of the local weight fraction at varying rates for a 3 wt% CsCl, 50 g salt sample run with a ΔT of 200°C and a no-lid configuration.

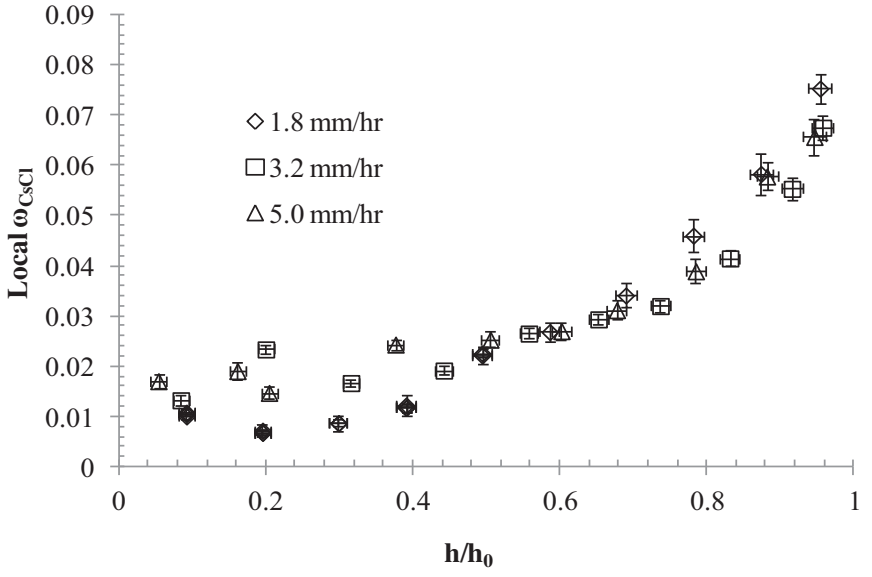

Figure D.4: Comparison of the local weight fraction at varying rates for a 3 wt% CsCl, 400 g salt sample run with a ΔT of 200°C and a no-lid configuration.

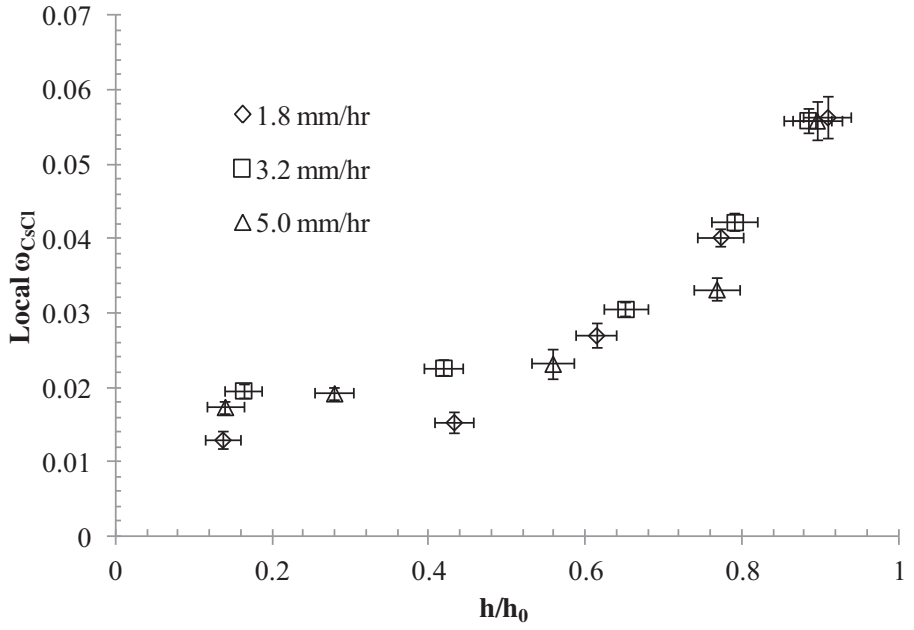

Figure D.5: Comparison of the local weight fraction at varying rates for a 3 wt%, 50 g salt sample run with a ΔT of 300°C and a lid configuration.

Appendix E - Modeling Comparisons

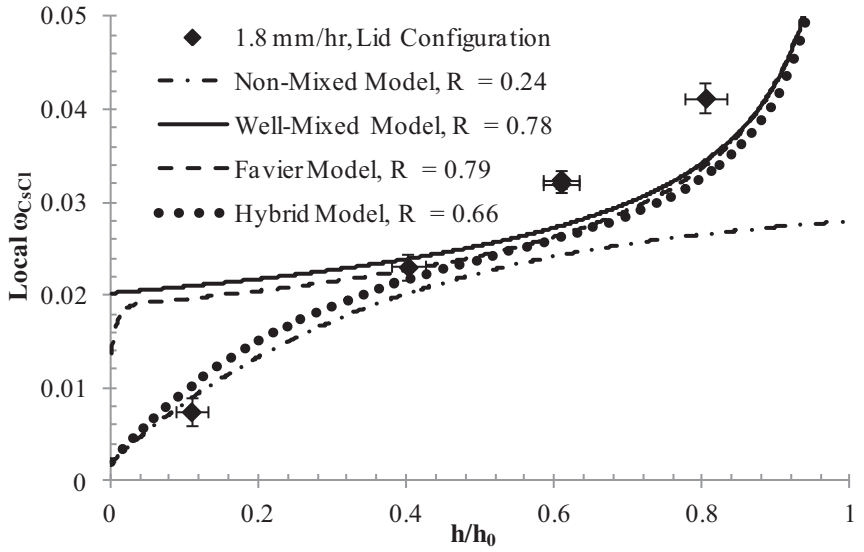

Figure E.1: Comparison of the non-mixed, well-mixed, Favier, and hybrid models. Experimental conditions were; 1.8 mm/hr, 50 g, lid configuration, and a $\Delta T = 200°C$.

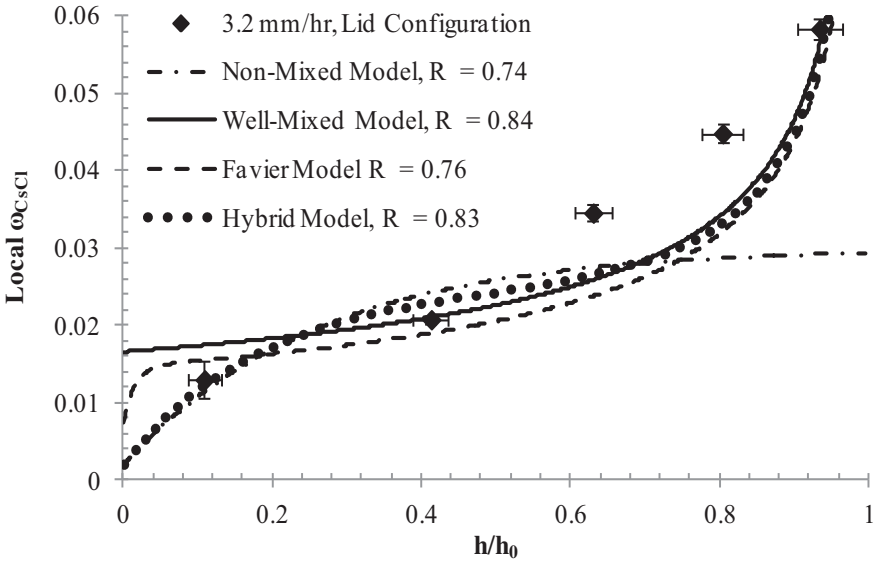

Figure E.2: Comparison of the non-mixed, well-mixed, Favier, and hybrid models. Experimental conditions were; 3.2 mm/hr, 50 g, lid configuration, and a $\Delta T = 200°C$.

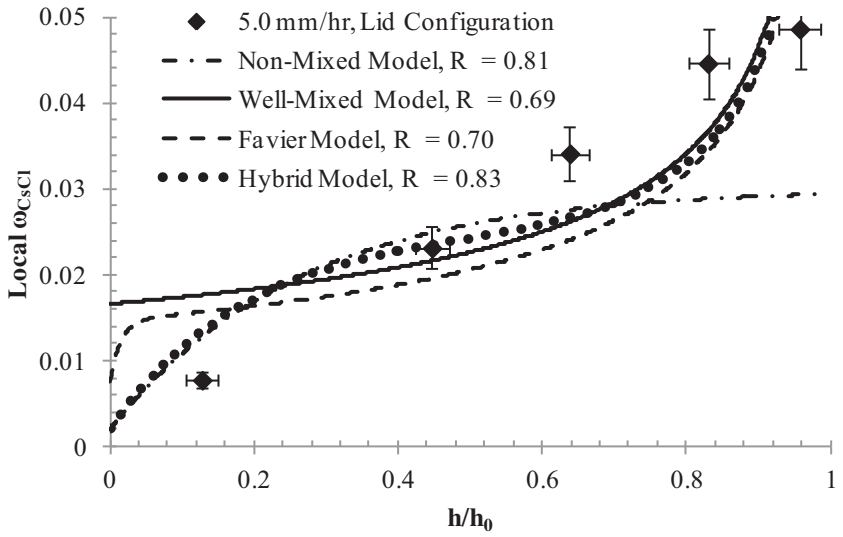

Figure E.3: Comparison of the non-mixed, well-mixed, Favier, and hybrid models. Experimental conditions were; 5.0 mm/hr, 50 g, lid configuration, and a $\Delta T = 200°C$.

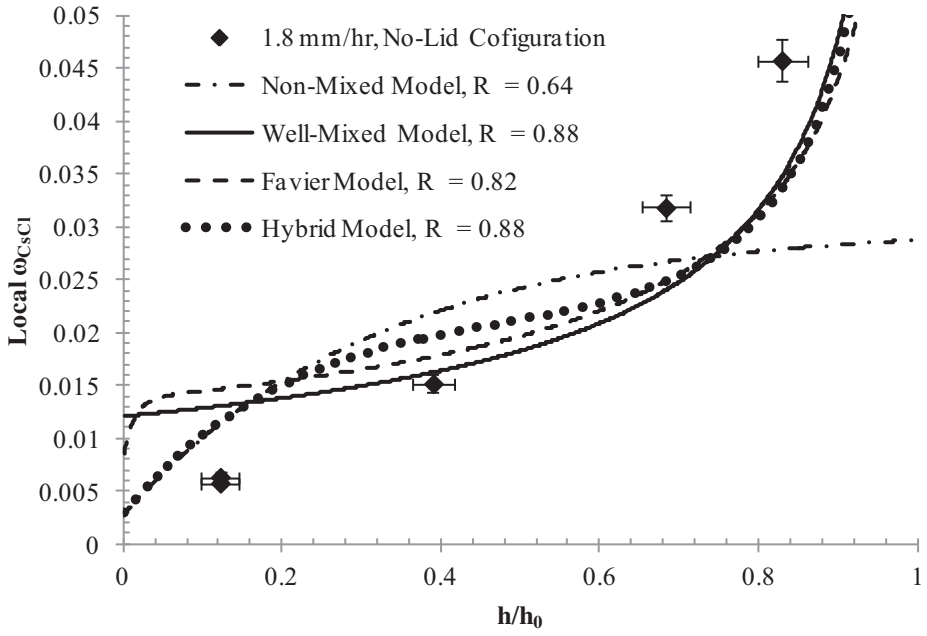

Figure E.4: Comparison of the non-mixed, well-mixed, Favier, and hybrid models. Experimental conditions were; 1.8 mm/hr, 50 g, no-lid configuration, and a $\Delta T = 200°C$.

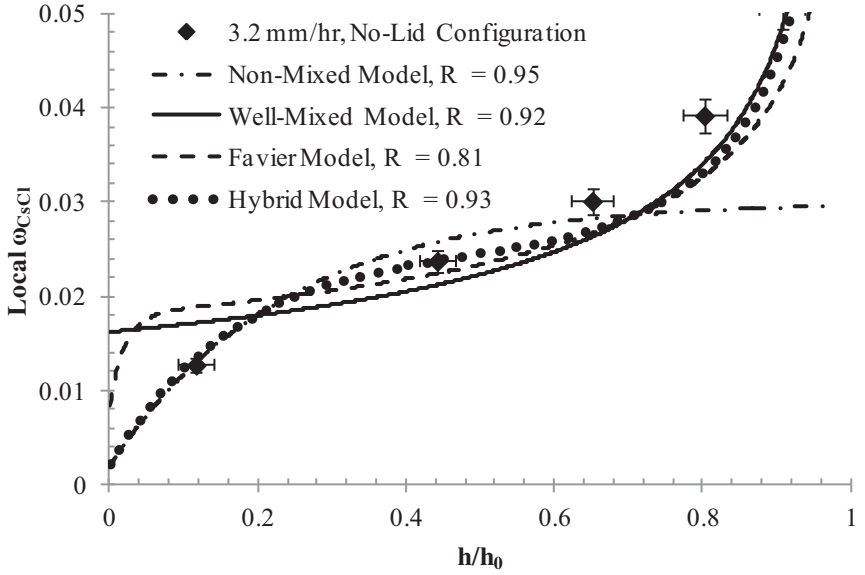

Figure E.5: Comparison of the non-mixed, well-mixed, Favier, and hybrid models. Experimental conditions were; 3.2 mm/hr, 50 g, no-lid configuration, and a $\Delta T = 200°C$.

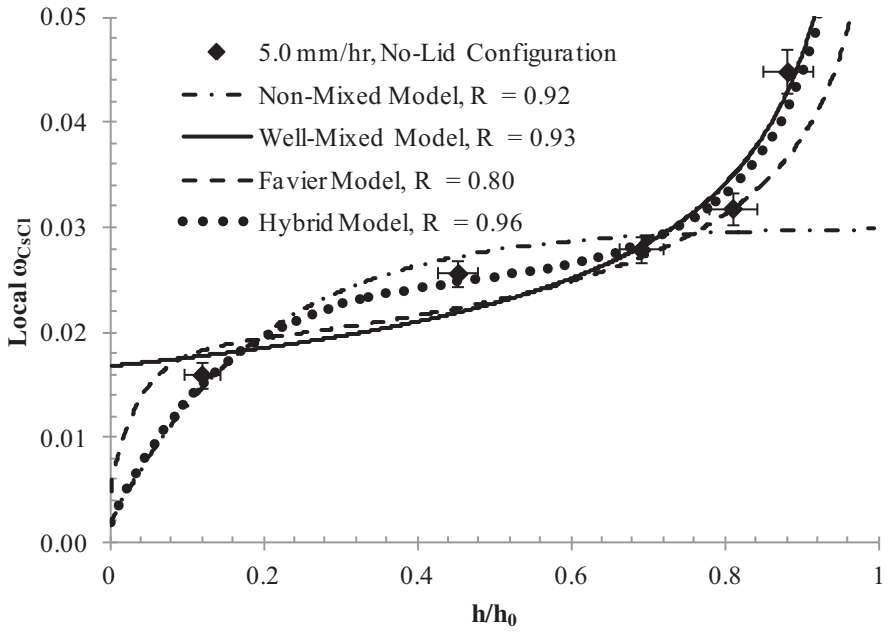

Figure E.6: Comparison of the non-mixed, well-mixed, Favier, and hybrid models. Experimental conditions were; 5.0 mm/hr, 50 g, no-lid configuration, and a $\Delta T = 200°C$.

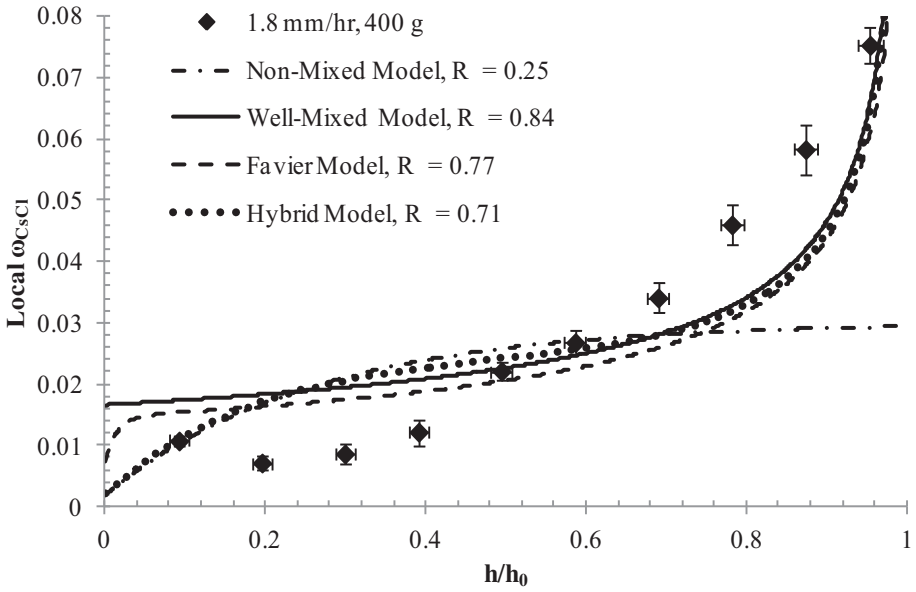

Figure E.7: Comparison of the non-mixed, well-mixed, Favier, and hybrid models. Experimental conditions were; 1.8 mm/hr, 400 g, no-lid configuration, and a $\Delta T = 200°C$.

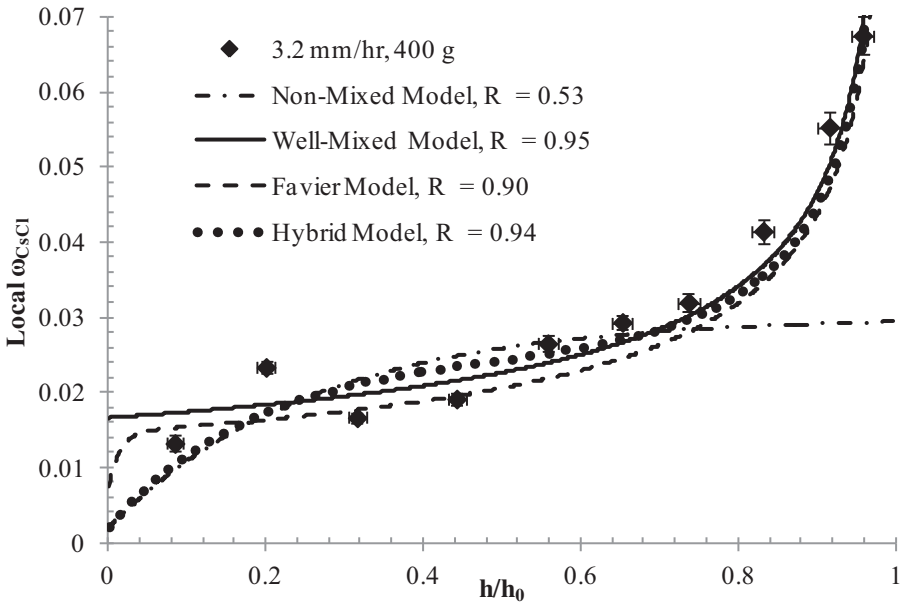

Figure E.8: Comparison of the non-mixed, well-mixed, Favier, and hybrid models. Experimental conditions were; 3.2 mm/hr, 400 g, no-lid configuration, and a $\Delta T = 200°C$.

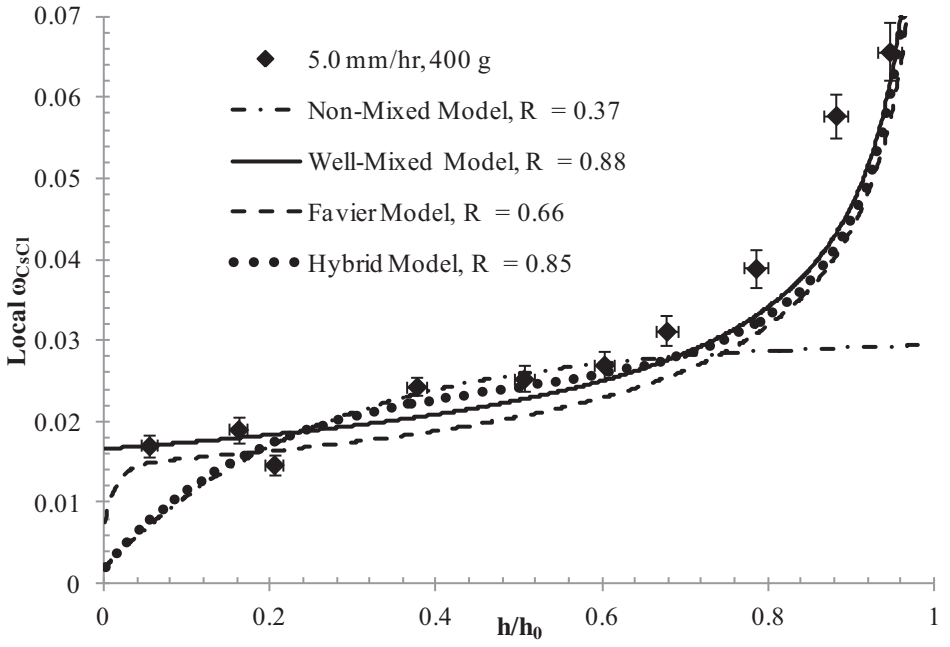

Figure E.9: Comparison of the non-mixed, well-mixed, Favier, and hybrid models. Experimental conditions were; 5.0 mm/hr, 400 g, lid configuration, and a $\Delta T = 200°C$.

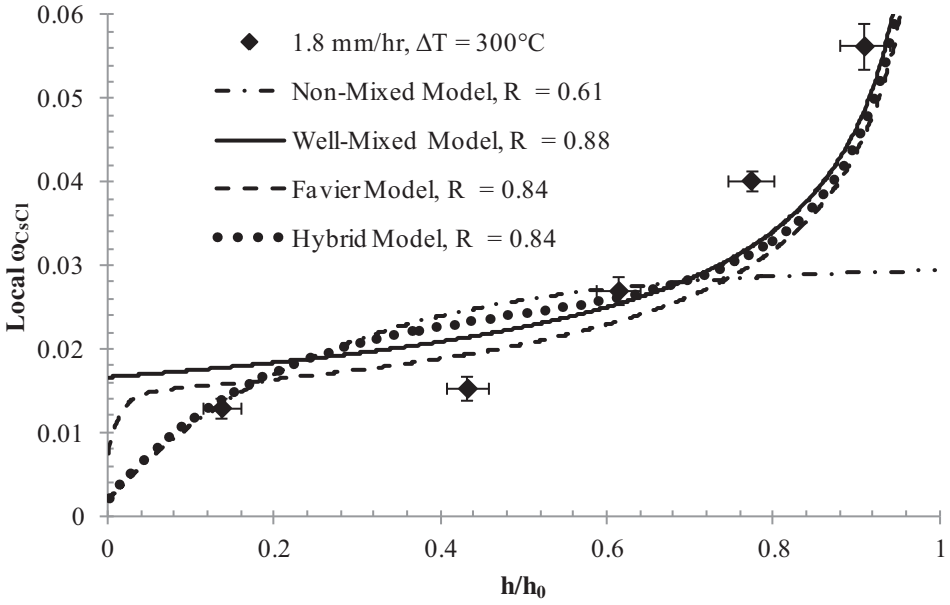

Figure E.10: Comparison of the non-mixed, well-mixed, Favier, and hybrid models. Experimental conditions were; 1.8 mm/hr, 50 g, no-lid configuration, and a $\Delta T = 300°C$.

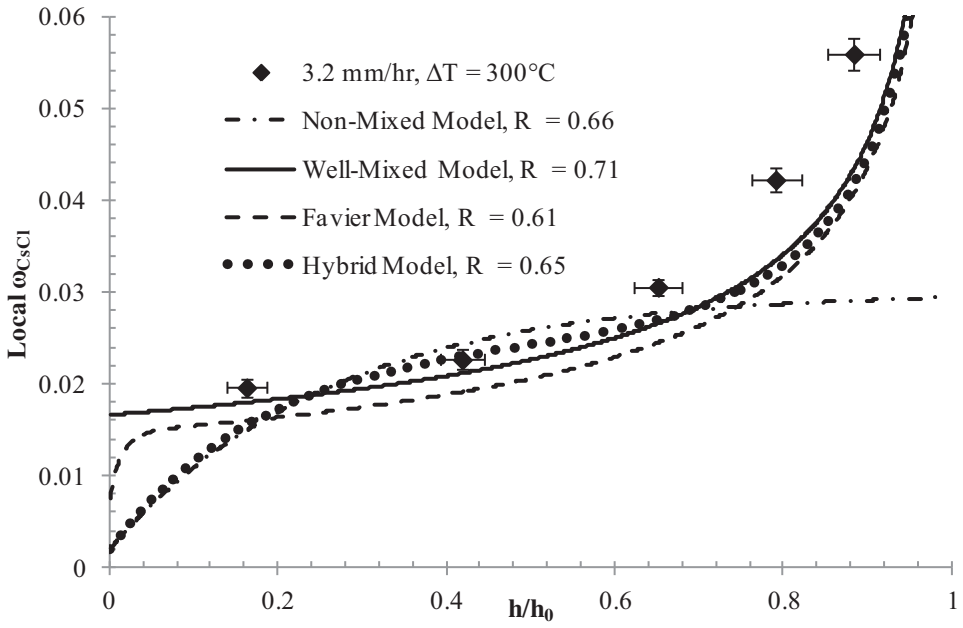

Figure E.11: Comparison of the non-mixed, well-mixed, Favier, and hybrid models. Experimental conditions were; 3.2 mm/hr, 50 g, no-lid configuration, and a ΔT = 300°C.

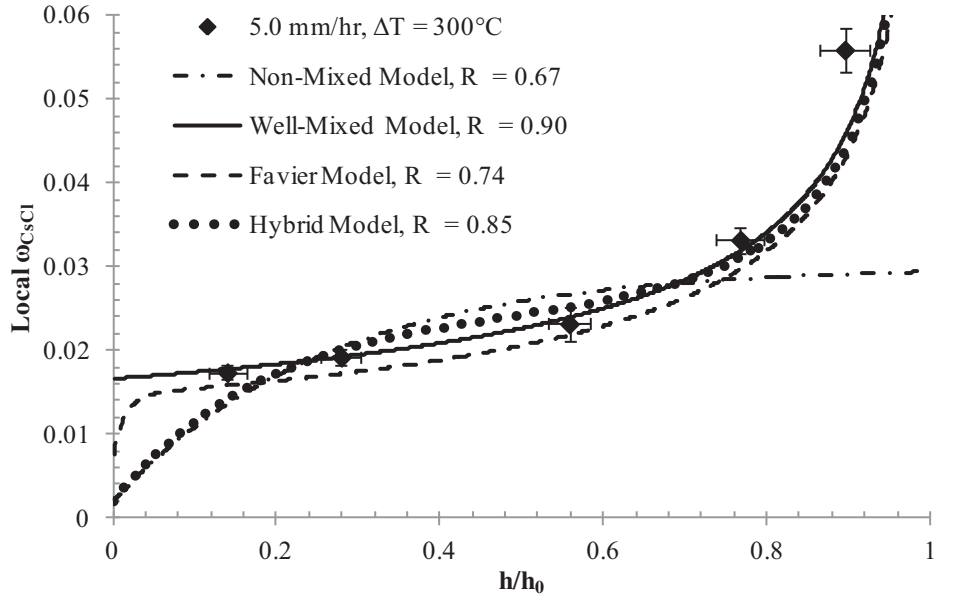

Figure E.12: Comparison of the non-mixed, well-mixed, Favier, and hybrid models. Experimental conditions were; 5.0 mm/hr, 50 g, no-lid configuration, and a ΔT = 300°C.